Protective effect of p38α MAP Kinase inhibitors in neurodegenerative diseases

Dissertation

der Mathematisch-Naturwissenschaftlichen Fakultät

der Eberhard Karls Universität Tübingen

zur Erlangung des Grades eines

Doktors der Naturwissenschaften

(Dr. rer. nat.)

vorgelegt von

Mariella Martorelli

aus Glarus/Schweiz

Tübingen

2024

Gedruckt mit Genehmigung der Mathematisch-Naturwissenschaftlichen Fakultät der Eberhard Karls Universität Tübingen.

Tag der mündlichen Qualifikation:	11.07.2024
Dekan:	Prof. Dr. Thilo Stehle
1. Berichterstatter/-in:	Prof. Dr. Stefan Laufer
2. Berichterstatter/-in:	Prof. Dr. Pierre Koch

CONTENTS

Abstract – English version

The p38α mitogen-activated protein (MAP) Kinase signaling pathway is known to be triggered by stress stimuli and to contribute to chronic inflammatory responses. A number of recent studies have identified this signaling pathway as a central player in different neurodegenerative diseases such as multiple sclerosis (MS) and Alzheimer Disease (AD) and their principal animal models: experimental allergic encephalomyelitis (EAE) and neuronal amyloidosis (APP/PS1 transgenic mice), respectively. This study set out to investigate the effect of inhibiting p38α MAP Kinase on the induction and development of EAE and amyloidosis and the potential of modulating this pathway as a disease-modifying therapy in both MS and AD respectively.

Thirteen novel "Skepinone-based" p38α MAP Kinase inhibitors were characterized *in vitro* and *in vivo* to select potent and metabolically stable Skepinone-based inhibitors of p38α MAP Kinase with the ability to cross the blood-brain barrier (BBB). Out of the 13 inhibitor compounds, **11** and **13** had the highest *in vitro* potency in human whole blood but differed in central neuro system (CNS) partition (**11** non-BBB-penetrant while **13** had a brain to plasma ratio of ca. 0.3). Certainly, continuing with thus, **11** and **13** were used as in detailed studies in EAE and Amyloidosis.

In earlier studies in CNS inflammation, there were indications that diet and diabetic status played a role in the overall inflammatory stress in the brain and in the regulation of the immune response in host mice. Given that these factors may play a role in human disease, the models were conducted with modified diets to potentially reflect the clinical situation for patients in developed countries.

The myelin oligodendrocyte peptide (MOG) EAE model in C57B6J mice was first optimized by taking into account effects of diet and antigen preparation. The goal was to reduce variation in incidence while maintaining severity at a moderate level (High Incidence, Low Variation Moderate Score: HILVMS). Briefly, the results suggest that allowing mice to mature for 4 weeks or more on a low fiber diet leads to a more uniform EAE response. Similarly, sonication of Complete Freund´s Adjuvant/Myelin oligodendrocyte peptide (CFA/MOG) emulsion made the response more uniform.

Compounds **11** and **13,** previously characterized *in vitro* and *in vivo* in **Chapter 1**, were evaluated in the optimized EAE model. Given that previous generations of p38 inhibitors were reported to exert untoward effects on the liver, detailed analysis of liver effects were included in the assessment of the model. Compound **11**, which had high levels in liver and spleen but not in the CNS, increased the survival of the EAE CFA/MOG induced animals while decreasing the severity of the signs of EAE. At a dose of 12 µmol/kg/day p.o., compound **11** could be considered moderately anti-inflammatory but highly protective of both liver morphology and of myelin levels in the brain.

Given its apparent protective effects in the acute inflammatory CNS model EAE, the next question was “would this compound also have a protective effect in a chronic degenerative model driven by amyloidosis, in which inflammation plays a significant role?”.

Compounds **11** (peripherally active) and **13** (BBB-penetrant) were applied p.o. in two different amyloidosis studies (long and short-term). Behavioral tests and histological findings showed pronounced treatment effects in both, long and short-term treatment studies. Both candidates improved cognitive and affective parameters in the long-term study: memory, activity and anxiety were maintained at WT levels in age-matched mice. Further histological analysis in brain showed that both compounds mediated the removal of Amyloid aggregates both over 10.5 months treatment (long-term study) or 2 weeks (short term study).

The short-term study was based on published data for **VX 745** which depleted amyloid in a Tg2576 amyloid mouse model over 3 weeks of treatment. In the APP/PS1 model, **VX 745** at 10 mg/kg p.o. was inactive over a 2-week application period and indeed was associated with a moderate increase in amyloid. It is not clear whether this difference is due to differences in the model, or to matters of dose. **VX 745**, despite promising data in animal models, failed in phase II clinical trials. The absence of activity in the APP/PS1 model is, at least, consistent with the clinical data.

In summary, these data suggest that the highly selective p38α MAP Kinase inhibitors were active in a range of systems from cellular to *in vivo* neurodegenerative settings. The effects in the animal models suggest that the substances are potentially useful as treatments for both, MS and AD.

Abstract – German Version

Der p38α mitogen-activated protein (MAP) Kinasesignalweg wird durch Stresssignale aktiviert und ist an chronischen Entzündungsreaktionen beteiligt. In aktuellen Studien wurde dieser Signalweg als ein Schlüsselfaktor bei der Entstehung neurodegenerativer Krankheiten, wie Multipler Sklerose (MS) und der Alzheimer Krankheit (AD), und deren wichtigsten Tiermodelle, die experimentelle allergiesche Enzehphalitis (EAE) und neuronale Amyloidose (beruhend auf transgenen APP/PS1 Mäusen) identifiziert. Ziel dieser Arbeit war es zu untersuchen wie sich eine Hemmung der p38α MAP Kinase Aktivität auf die Induktion und Ausprägung einer EAE und Amyloidose im Mausmodel auswirken. Dadurch sollte geklärt werden, inwiefern eine Modulation dieses Signalwegs als Therapieansatz bei AD und MS geeignet ist.

Dreizehn neuartige Skepinon-basierte p38α MAP Kinase Inhibitoren wurden in vitro und in vivo charakterisiert um wirksame Kandidaten zu selektieren, die metabolisch stabil sind und in der Lage sind die Blut-Hirn-Schranke zu passieren.

In humanem Vollblut zeigten die Wirkstoffe **11** und **13** die höchste Potenz, dabei ist Wirkstoff **11** im Gegensatz zu Wirkstoff **13** nicht hirngängig. Wirkstoff **11** und Wirkstoff **13** wurden für nachfolgende EAE und Amyloidose Studien ausgewählt.

Es ist aus Mausstudien zum zentralen Nervensystem (ZNS) bekannt, dass Ernährung und Diabetesstatus auf die Entzündungsbelastung des Gehirns und die Regulierung der Immunantwort Einfluss nehmen. Daher wurden die Mausmodelle mit modifizierten Diäten durchgeführt, welche an die Ernährung von Menschen in Industrieländern angepasst waren.

Das Myelin-Oligodentrozyten-Glykoprotein (MOG) induzierte EAE Modell in C57B6J Mäusen wurde durch das Testen unterschiedlicher Diäten und Antigenpräparationen optimiert. Ziel war es die Variabilität in der Inzidenzrate zu reduzieren und gleichzeitig die Symptomatik moderat zu halten (hohe Inzidenz, niedrige Variabilität, moderate Symptomatik). Kurz gesagt deuten die Ergebnisse darauf hin, dass es zu einer gleichmäßigeren EAE-Reaktion führt, wenn man Mäusen erlaubt vier Wochen oder länger mit einer ballaststoffarmen Ernährung heranzureifen. Zusätzlich konnte durch die Ultraschallbehandlung der Emulsion aus Freund´s Adjuvant und Myelin-Oligodentrozyten-Glykoprotein (CFA/MOG) Emulsion eine homogene Immunantwort induziert werden.

Die Wirkstoffe **11** und **13** wurden im optimierten EAE-Modell getestet. Da früheren Generation von p38α MAP Kinase Inhibitoren eine leberschädigende Wirkung zugeschrieben wurde, wurde eine detaillierte Leberanalyse durchgeführt und in die Bewertung mit einbezogen. Wirkstoff **11** wies hohe Konzentrationen in Milz und Leber auf, jedoch nicht im ZNS. Dennoch erhöhte Wirkstoff **11** die Überlebensrate und

verringerte die Krankheitssymptome im EAE-Modell. Bei einer Dosis von 12 µmol/kg/Tag p.o zeigte Wirkstoff **11** einen leicht entzündungshemmenden Effekt verbunden mit einer ausgeprägten protektiven Wirkung auf das Gehirn ohne die Leber zu schädigen.

Angesichts seiner offensichtlichen schützenden Wirkung im akuten entzündlichen ZNS-Modell EAE lautete die nächste Fragestellung: „Würde dieser Wirkstoff auch in einem chronisch degenerativen Modell, das durch Amyloidose verursacht wird und bei dem Entzündungen eine bedeutende Rolle spielen, eine schützende Wirkung haben?“.

Beide Wirkstoffe wurden peroral (p.o.) sowohl in einer Langzeit- als auch in einer Kurzzeit-Amyloidose Studie getestet. In beiden Studien zeigten Verhaltenstests und histologische Untersuchungen deutliche Behandlungseffekte. Beide Wirkstoffkandidaten verbesserten kognitive und affektive Parameter in der Langzeitstudie. So waren Erinnerungsvermögen, Aktivität und Angst vergleichbar zu altersentsprechenden Wildtypmäusen. Histologische Untersuchungen des Gehirns zeigten bei beiden Studien eine Reduzierung von Amyloid-Aggregaten in den wirkstoffbehandelten Tieren.

Das Studiendesign der Kurzzeitstudie basierte auf bereits veröffentlichten Daten für den Wirkstoff **VX 745**, welcher Amyloid-Aggregate im Tg2576 Amyloid Mausmodell nach 3-wöchiger Behandlung reduzierte. Im APP/PS1 Modell zeigte **VX 745** bei einer Dosis von 10 mg/kg p.o jedoch keine amyloidreduzierende Wirkung über einen zweiwöchigen Behandlungszeitraum. Dies könnte auf Unterschiede im Mausmodel oder einer falschen Dosierung zurückzuführen sein.

Zusammenfassend beschreibt die hier vorgelegte Arbeit den deutlichen Therapieerfolg der durch die Behandlung mit hochspezifischen p38α MAP Kinase Inhibitoren bei verschiedenen neurodegenerativen in vitro und in vivo Modellen erzielt werden konnte. Die Ergebnisse verdeutlichen das große Potential dieser Wirkstoffe für eine weiterführende Testung zur Behandlung neurodegenerativer Erkrankungen des Menschen, wie MS oder AD.

Publications

Tormählen NM*, **Martorelli M***, Kuhn A, Maier F, Guezguez J, Burnet M, Albrecht W, Laufer SA, Koch P. *Design and Synthesis of Highly Selective Brain Penetrant p38α Mitogen-Activated Protein Kinase Inhibitors*. J Med Chem. 2022 Jan 27;65(2):1225-1242. doi: 10.1021/acs.jmedchem.0c01773. *Indicates equal author contribution

Straß S, Geiger J, Cloos N, Späth N, Geiger S, Schwamborn A, De Oliveira da Cunha L, **Martorelli M**, Guse JH, Sandri TL, Burnet M, Laufer S. *Immune cell targeted fumaric esters support a role of GPR109A as a primary target of monomethyl fumarate in vivo*. Inflammopharmacology. 2023 Jun;31(3):1223-1239. doi: 10.1007/s10787-023-01186-0.

Straß, S., Geiger, J., **Martorelli, M**. *et al. Isostearic acid is an active component of imiquimod formulations used to induce psoriaform disease models*. Inflammopharmacol 31, 799–812 (2023). https://doi.org/10.1007/s10787-023-01175-3

Julian Laux, **Mariella Martorelli**, Nadja Späth, Florian Maier, Michael Burnet, and Stefan A. Laufer *Selective Inhibitors of Janus Kinase 3 Modify Responses to Lipopolysaccharides by Increasing the Interleukin-10-to-Tumor Necrosis Factor α Ratio.* ACS Pharmacology & Translational Science Article ASAP DOI: 10.1021/acsptsci.3c00043

Julian Laux*, **Mariella Martorelli***, Simon Strass, Dieter Schollmeyer, Florian Maier, Michael Burnet, and Stefan A. Laufer. *Inherent Fluorescence Demonstrates Immunotropic Properties for Novel Janus Kinase 3 Inhibitors.* ACS Pharmacology & Translational Science 2023 6 (10), 1433-1452 DOI: 10.1021/acsptsci.3c00119. *Indicates equal author contribution

Mariella Martorelli, Matthias Dengler, Julian Laux, Tina Fischer, Agne Vaiceliunaite, Ulrike Hahn, Thilo Weinstein, Santiago Cruces, Christina Pokoj, Luciano de Oliveira da Cunha, Lara Wohlbold, Pierre Koch, Stefan Laufer, Michael Burnet and Florian Maier. *A robust, high incidence and moderate severity form of EAE mediated by a low fiber diet and sonicated CFA/MOG emulsion.* Under peer review, Journal of Neuroinflammation.

Chapter 1

Characterization of highly selective brain-penetrant p38α Mitogen-Activated Protein Kinase inhibitors

Tormählen NM*, **Martorelli M***, Kuhn A, Maier F, Guezguez J, Burnet M, Albrecht W, Laufer SA, Koch P. *Design and Synthesis of Highly Selective Brain Penetrant p38α Mitogen-Activated Protein Kinase Inhibitors*. J Med Chem. 2022 Jan 27; 65(2):1225-1242. doi: 10.1021/acs.jmedchem.0c01773. *Indicates equal author contribution

Abbreviations

%, Percentage;

°C, Celsius degree;

ACN, Acetonitril;

AD, Alzheimer's disease;

BBB, Blood-brain-barrier;

CDI, 1,1'-carbonyldiimidazole;

CNS, Central nervous system;

CO_2, Carbon dioxide;

ELISA, Enzyme-linked immunosorbent *assay;*

ESI, Electrospray Ionization;

HBC, Human Buffy Coat;

HCl, Hydrogen chloride;

HLM, Human liver microsomes;

HPLC/MS/MS, Liquid Chromatography with tandem mass spectrometry;

HR, Hydrophobic region;

HWB, Human whole blood;

IC_{50}, Half maximal inhibitory concentration;

IL1β, interleukin 1 beta;

IL-6, Interleukin 6

IS, Internal Standard;

LC-MS, Liquid Chromatography mass spectrometry;

LPS, Lipopolysaccharide;

MAP, Mitogen-activated protein;

MS, Multiple sclerosis;

MTT, (3-[4,5-dimethylthiazol-2-yl]-2,5 diphenyl tetrazolium bromide)

MWB, Mouse whole blood;

MWM, Morris water maze;

TNFα, Tumor necrosis factor α.

1.1 Introduction

Stress-induced activation of p38α mitogen-activated protein (MAP) Kinase leads to overproduction of pro-inflammatory cytokines, and it is known to be expressed in glia cells and neurons, and therefore is associated with neuroinflammation and neurodegeneration.[1,2,3,4,5,6,7] In the mid-1990s, the discovery of its mode of action made it an early choice as a drug target for chronic inflammation. In particular, it has been demonstrated that during inflammation, the p38α MAP Kinase catalyzes the transfer of the γ-phosphate of its natural co-substrate, ATP, to the hydroxyl group of serine and threonine side chains of its substrate.[8] In addition, in post mortem brain tissue from Alzheimer disease (AD) patients increased activity of p38α MAP Kinase was found.[9,10] In response to stressors like Amyloid-β42[11] as well as during tau localization, p38α MAP Kinase was found to stimulate in microglia the release of different pro-inflammatory cytokines like interleukin (IL)-1β and tumor necrosis factor α (TNFα).[12] In addition, a number of recent studies have identified this signaling pathway as a central player in Multiple Sclerosis (MS) and its principal animal model, experimental allergic encephalomyelitis.[13,14,15] Early evidence for the involvement of p38 MAP Kinase in MS came from microarray studies showing that the expression of MAP Kinase 14 (encoding p38α) was elevated ~ five-fold in CNS lesions of MS patients.[16] Due to this association with CNS inflammation, the more recently described p38 MAP Kinase inhibitor Neflamapimod (**Figure 1**, VX 745)[17], a selective p38α MAP Kinase inhibitor with a low brain to plasma ratio and inferior selectivity amongst p38 isoforms, was selected for Phase II trials for the treatment of AD (NCT02423200, NCT02423122 & NCT03402659). Originally, Neflamapimod was developed for the treatment of Rheumatoid Arthritis, however was discontinued due to side-effects in preclinical studies.[18] Another brain-penetrant pryidinylpyridazine-based p38α MAP Kinase inhibitor MW150 (**Figure 1**) was investigated in diverse animal models of neurological disorders including models of AD.[11,19,20,21,22] Although it appeared to improve results in the Morris water maze (MWM) on APP/PS1 mice, pharmacodynamic data and safety profile, MW150 is currently being investigated in early stage clinical trials.[22]

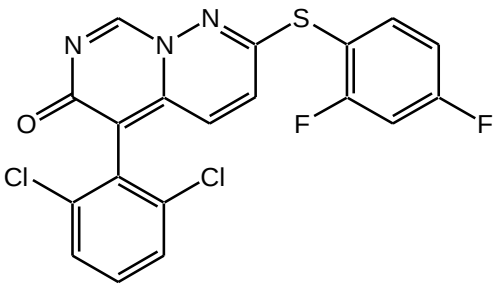

Neflamapimod
IC_{50} (p38α) 10 nM

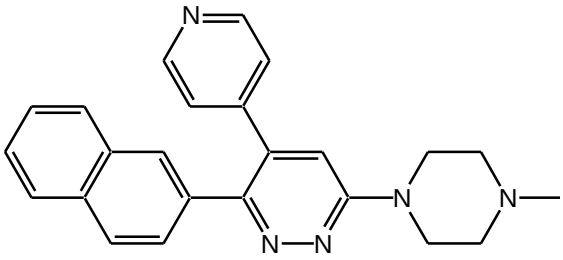

MW150
IC_{50} (p38α) 230 nM

Figure 1. Structures of p38α MAP Kinase inhibitors Neflamapimod (VX 745) and MW150.

In 2012, research of potent p38α MAP Kinase inhibitors dibenzosuberone derivatives Skepinone-L and Skepinone-N (**Figure 2**) showed outstanding kinome selectivity.[23,24] The prototypic compound that Skepinone-L serves has been used in various studies as a probe to further investigate the role of p38α MAP Kinase in various disorders.[23]

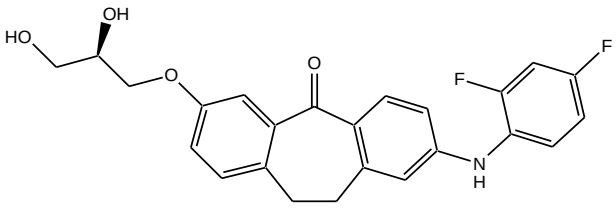

Skepinone- L
IC_{50} (p38α) 5 nM

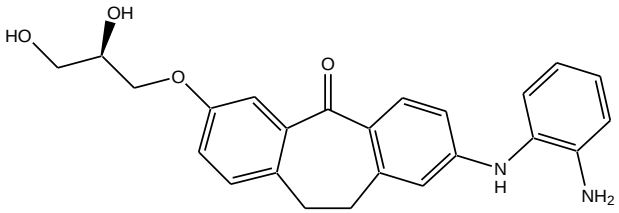

Skepinone- N
IC_{50} (p38α) 20 nM

Figure 2. Structures of p38α MAP Kinase inhibitors Skepinone-L and Skepinone-N.

X-ray analysis of this inhibitor in complex with the target enzyme revealed its binding mode, showing that it acts as a type I kinase inhibitor, inducing a glycine flip at the hinge region and addresses the hydrophobic region (HR) I as well as the HR II (**Figure 3**). Several studies have been reported using Skepinone-L as a lead structure e.g. for the design of Skepinone-based type I½ inhibitors of p38α MAP Kinase with improved binding kinetics.[25,26]

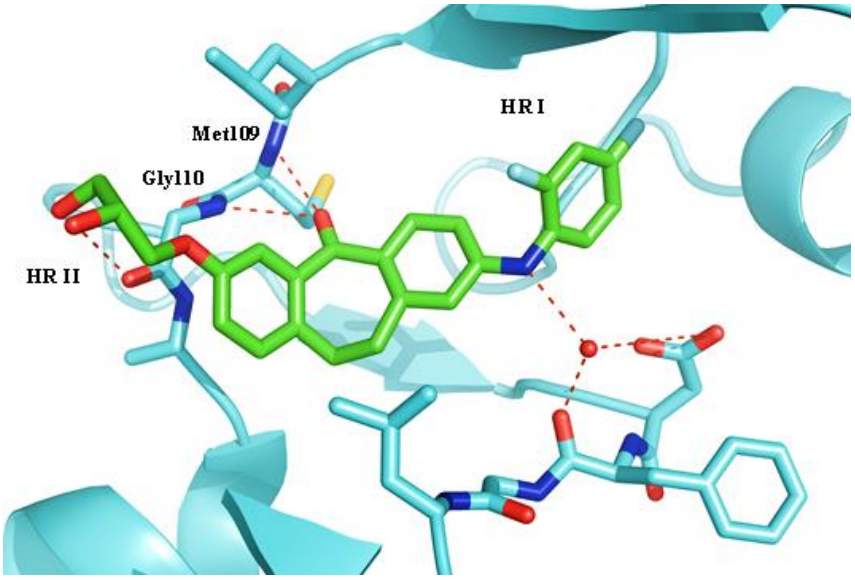

Figure 3. Binding mode of Skepinone-L (**Figure 2**) within the ATP binding site of p38α MAP Kinase. This Figure is adapted from: Tormählen NM. and Martorelli M. *et. al*. 2022.[27]

Aim

The overall aim of this chapter was to characterize *in vitro* and *in vivo* selective and metabolically stable Skepinone-based inhibitors of p38α MAP Kinase, which have the ability to cross the blood-brain barrier (BBB). The most potent *in vitro* inhibitors were tested in follow-up analysis in different inflammatory and neurodegenerative models such as AD or MS. In conclusion, it was hypothesized that while there is potential to improve AD and MS signs using selective p38α MAP Kinase inhibitors, those optimized for being BBB-penetrant are more likely to exert potent central anti-inflammatory effects. Therefore, the anti-inflammatory drug development program aimed at producing p38α MAP Kinase inhibitors with IC_{50} in the single digit nanomolar range, high brain-to-plasma ratios, ideally paired with high metabolic stability and a low level of side-effects. Taken together, I proposed using highly selective p38α MAP Kinase inhibitors for treating chronic inflammation in MS and AD, in both the periphery and CNS. First, the *in vitro* and *in vivo* drug screening experiments are shown, which allowed a selection of promising compounds for further studies.

1.2 Material and Methods

Structures of the tested p38α MAP Kinase inhibitors

The compounds' structures used in this work, dibenzosuberones **1** – **13**, are showed in **Table 1** of this thesis. 2D structures design graphs of each compound were arranged by engaging ChemDraw Ultra 6.0 software.

Table 1. p38α MAP Kinase inhibitors investigated and their structures.

Compound numbers	Structures
1	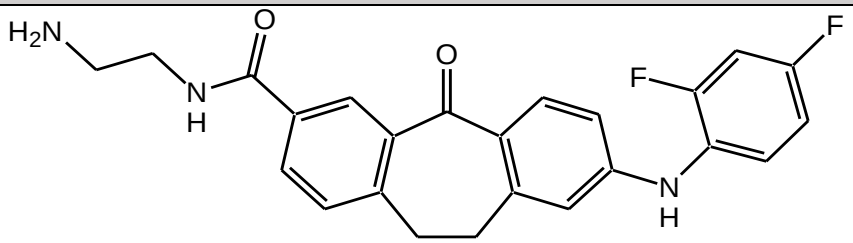
2	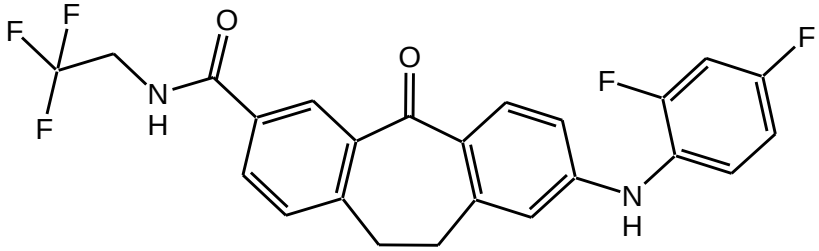
3	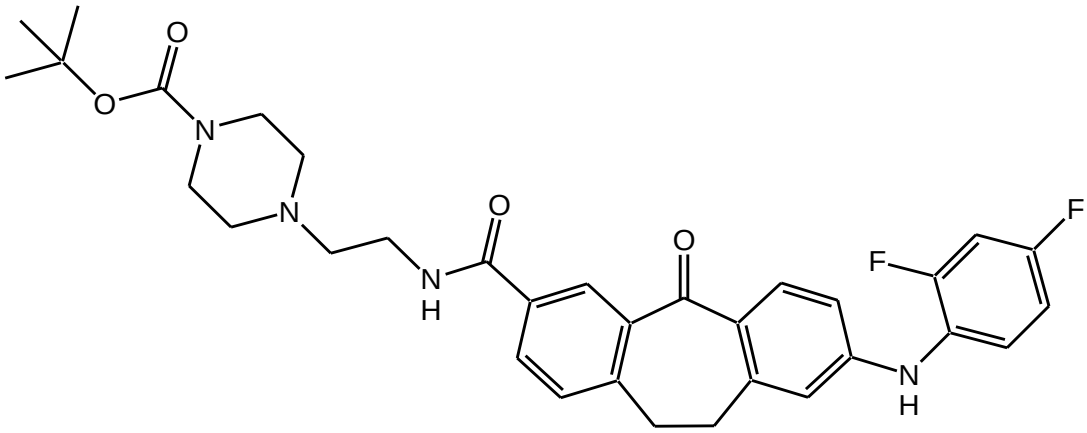

4	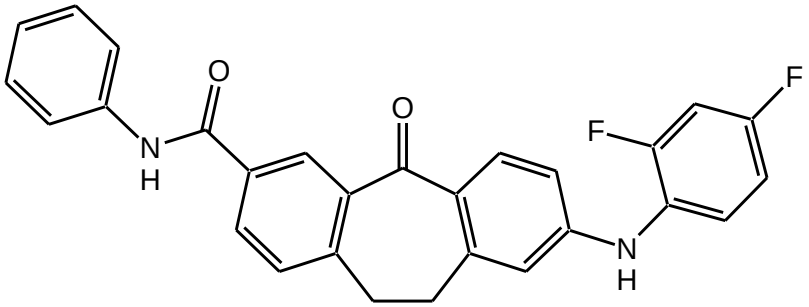
5	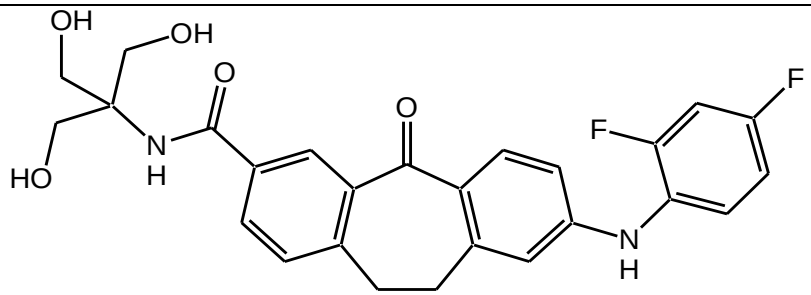
6	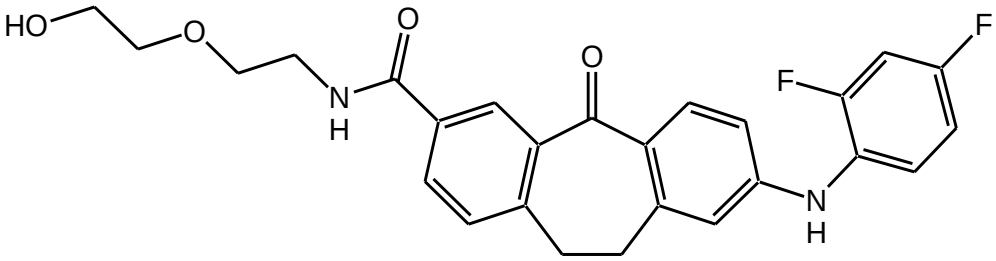
7	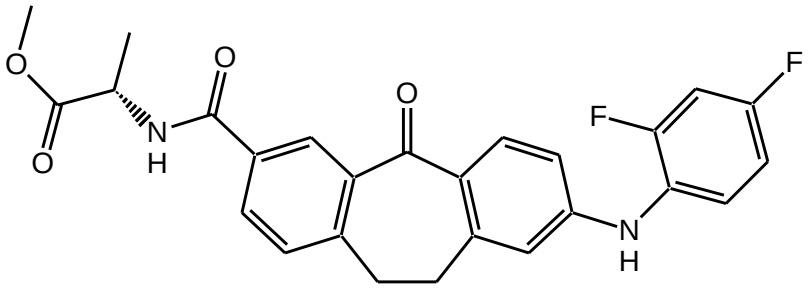
8	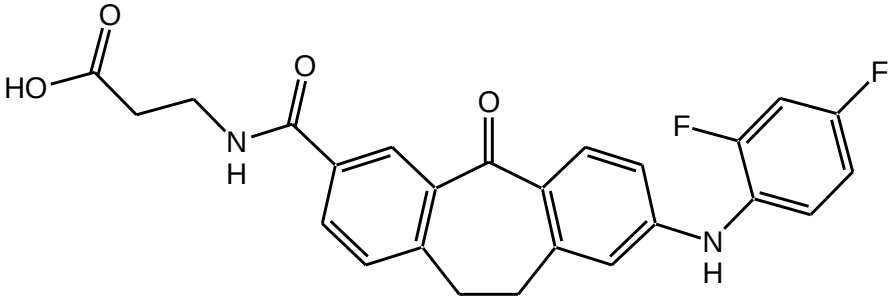

9	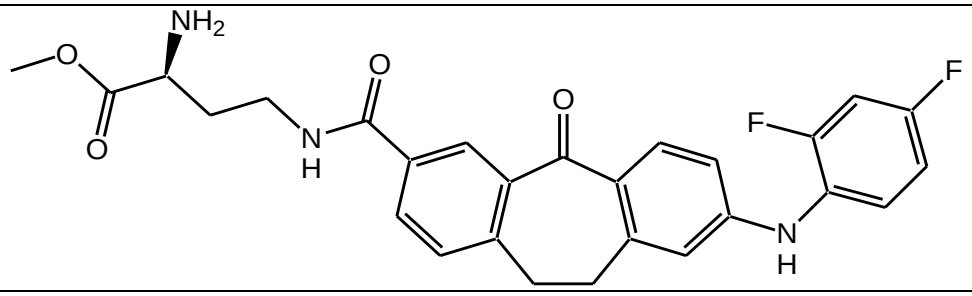
10	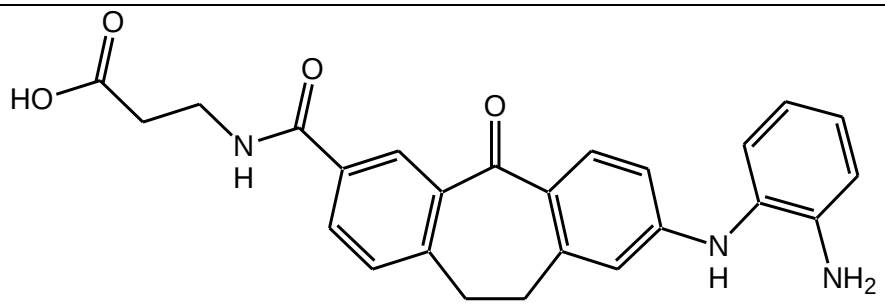
11	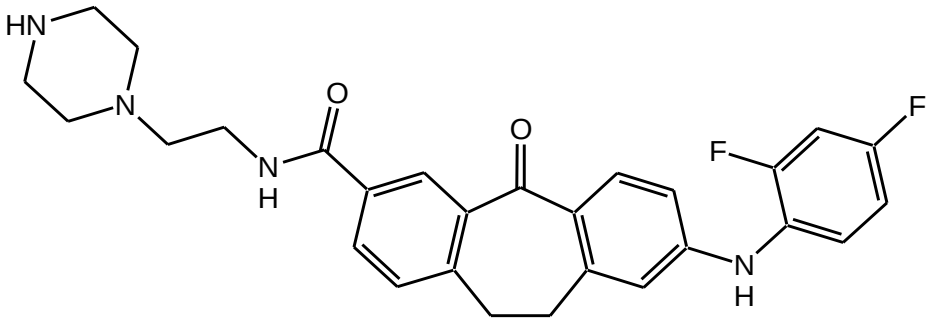
12	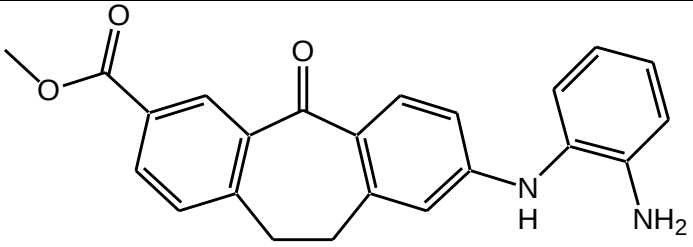
13	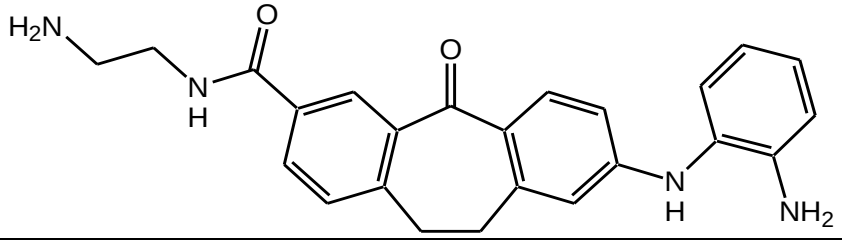

MTT on BALB/c Splenocytes:

The MTT assay consist of a colorimetric reaction that is widely used to assess cell viability. However, one must consider that the enzymatic reduction of 3-[4,5-dimethylthiazole-2-yl]-2,5-diphenyltetrazolium bromide (MTT) to MTT-formazan is catalyzed by mitochondrial dehydrogenases. Hence, the MTT assay is dependent on mitochondrial

activity and indirectly serves to assess cellular energy consumption. Splenocytes were seeded into 96-well microplates (spleens were taken from female BALB/c mice, the splenocyte isolation protocol is described in the next paragraph). After treatment with p38 MAP Kinase inhibitors, MTT solution was added to the cells with a final concentration of 0.5 mg/mL and the mixture was allowed to incubate at 37 °C for 2 h. Afterwards, the supernatant was removed and cell pellets resuspended in acidified isopropyl alcohol (0.04 N HCl). After an incubation period of 30 min at room temperature, the absorbance of the formazan solution was read spectrophotometrically at 570 nm.

ELISA IL-6 and TNFα on BALB/c Splenocytes:

Female BALB/c mice were terminated with CO_2 and spleens were harvested. Individual spleens were put into a small petri dish and sliced lengthwise with a scalpel; 2-3 mL sterile PBS was added and the tissue was teased apart using a disposable plastic loop. To prepare single-cell suspensions, cell aggregates were broken up by pulling them several times through a 5 mL plastic syringe. The cell suspension was then transferred into 15 mL plastic tubes and left to stand for 5 min to allow larger lumps of cells to settle. Erythrolysis was performed using red blood cell (RBC) lysis buffer (1 g Sodium Bicarbonate ($NaHCO_3$), 8 g Ammonium Chloride (NH_4Cl), 2 mL 0.5 M EDTA in 1 L H_2O) and the mixture was centrifuged at 500 x g for 10 min. Cells were washed with sterile PBS (three times) and once with spleen cell medium (45 % DMEM low glucose (Gibco Invitrogen, Karlsruhe, Germany, cat- no. 31885-023), 45 % RPMI 1640 (Gibco, cat. no. 21875-034), 10 % fetal calf serum (Biochrom Ag, Berlin, Germany, cat no. S0115, 50 µM β-mercaptoethanol (Roth GmbH, Karlsruhe, Germany, cat. no. 4227.1)). The supernatant was then transferred into 2 mL tubes and spun down at 400 x g for 10 min. The pellet was carefully resuspended in spleen cell medium and spun again. After resuspending the pellet for the second time, the cell density was determined and the cell suspension diluted accordingly. OD 600 nm = 0.1 corresponded to $2x10^6$ cells/mL. The cell suspension was added to 96-well round-bottom plates (Nunc, Rosklide, Denmark) at a density of 2×10^6 cells per well, and stimulated with 500 ng Lipopolysaccharide (LPS) (E.coli 0111:B4, this LPS-type and stock was used for all following experiments) per well overnight, in a total volume of 200 µL spleen culture medium. In the negative control, splenocytes received no LPS stimulation, instead sham stimulation (sterile PBS was used). Cell culture supernatants were removed after overnight incubation, and assayed for TNFα - or IL-6-release. In both cases, standard curve ranges were prepared by making serial dilutions from 500 pg/mL to 7.5 pg/mL (BioLegend ® ELISA MAX™ *Standard*).

ELISA IL-6 and TNFα on C57BL/6 Mouse Whole Blood:

Adult female C57BL/6 mice were terminated with CO_2, heparinized heart blood was collected and stored on ice. Whole blood was used to perform ELISA and immune cells were stimulated with 500 ng LPS per well overnight, in a total volume of 150 µL. In the negative control, cells received no LPS stimulation (instead, sterile PBS was used as sham stimulus). Next, plates were centrifuged at 500 x g for 10 minutes. Supernatants were removed and assayed for TNFα - or IL-6-release. In both cases, standard curve ranges were prepared by making serial dilutions from 500 pg/mL to 7.5 pg/mL (BioLegend ® ELISA MAX™ *Standard*).

ELISA IL-6 and TNFα on HBC:

Human buffy coat extracted from human full blood was kindly provided by ZKT Tübingen GmbH (Otfried-Müller-Straße 4/1, 72076 Tübingen). Erythrolysis was performed using RBC lysis buffer (1 g Sodium Bicarbonate ($NaHCO_3$), 8 g Ammonium Chloride (NH_4Cl), 2 mL 0.5 M EDTA in 1 L H_2O) and the mixture was centrifuged at 500 x g for 10 min. Cells were washed with PBS (three times) and once with medium (RPMI medium supplemented with 10 % FBS (1 mM Pyruvate and 100 µg/mL penicillin-streptomycin)). The cell pellet was resuspended in sterile medium and stimulated with 100 ng LPS per well overnight in a total volume of 200 µL. In the negative control, HBC cells received no LPS stimulation (instead, sterile PBS was used as sham stimulus). Next, plates were centrifuged at 500 x g for 10 minutes. Cell culture supernatants were removed and assayed for TNFα - or IL-6-release. In both cases, standard curve ranges were prepared by making serial dilutions from 500 pg/mL to 7.5 pg/mL (BioLegend ® ELISA MAX™ *Standard* for IL-6 and R&D System for TNFα).

Uptake with HBC cells (Analytic):

HBC cells were used for this assay at a concentration of $1*10^6$ cells/mL in a 1.5 mL tube and incubated with p38 MAP Kinase inhibitors at a concentration of 100 µM. During incubation at different time points (0, 15 min, 1 h, 2 h, 4 h, 24 h), tubes were centrifuged at 500 x g for 10 minutes. Supernatants were then transferred and acetonitrile (ACN) and internal LC-MS standard (terbuthylazine) were added to supernatants and pellets at respective time-points. Tubes were then centrifuged at 500 x g for 10 minutes and both (supernatant and pellet) were stored at 4 °C until MS-analytics were performed.

In vivo experiments:

In vivo experiments were performed in accordance with German animal welfare law. All experiments were approved by the Regierungspräsidium Tübingen under animal

application number SYN 11/18. Briefly, 12-week-old, female C57BL/6-mice were treated either i.v. or p.o. with 0.4 mg/kg and 5 mL/kg of p38 MAP Kinase inhibitors in cassettes, with four compounds per cassette based on their molecular weight (MW). The experiment was done using six different peripheral tail vein blood sampling time points: 5 min, 15 min, 30 min, 1h, 2h and 4h. Termination of animals was performed at two different time-points: 2h and 4h post substance application; compound concentrations were analyzed in heart plasma, liver, kidney, brain right hemisphere and brain left hemisphere by LC-MS in order to evaluate BBB penetration, peripheral organ availability and plasma levels of the respective p38 MAP Kinase inhibitors. Formulations for i.v. applications were done with 10 % DMSO (stock solutions of p38 MAP Kinase inhibitors) and 90 % C57BL/6 female mouse serum. Formulations for p.o. applications were done with 10 % DMSO (stock solutions of p38 MAP Kinase inhibitors) and 90 % 0.5 % citric acid, 0.5 % hydroxypropyl methylcellulose (HPMC) in sterile, ultra-pure water.

LC-MS analysis:

The analytical methodology used was an HPLC instrument, which comprises an Agilent 1260 Binary Pump (Inv. 0408), the CTC PAL Autosampler (Inv. 0409) and an Agilent 1260 thermostatted Column Compartment (Inv.0202). The HPLC system was coupled to a Triple Quadrupole API 4500 (Inv. 0406) (PM-41) Mass Spectrometer (ABSciex, Redwood City, California, USA). Data acquisition and processing were carried out with the Analyst® Instrument Control and Data Processing Software v. 1.6.2. Chromatographic separation took place at 40 °C using Restek Biphenyl 2.7 µm, 50*2.1 mm column. The mobile phase consisted of a gradient (see **Table 2**) of water + 0.1 % formic acid, and ACN + 0.1 % formic acid at a flow rate of 500 µL/min and injection volume of 4 µL.

Table 2. Method mobile phase gradient.

Total time (min)	Flow rate (µl/min)	A (%)	B (%)
0	500	90	10
1	500	90	10
3	500	0	100
6	500	0	100
7	500	90	10
10	500	90	10

A: Water+0.1 % Formic acid

B: ACN+0.1 % Formic acid

Positive ion electrospray ionization (ESI) mass spectrum assessment of p38 MAP Kinase inhibitors and the Internal Standard (IS) was carried out. P38 MAP Kinase inhibitors and terbuthylazine (IS) Q1/Q3 masses, dwell time and mass spectrometer analytes specific parameters can be found in **Table 3**.

Table 3. Mass spectrometer parameters for P38 MAP Kinase inhibitors and terbuthylazine.

Compound	Q1 mass (Da)	Q3 mass (Da)	DP (volts)	EP (volts)	CE (volts)	CXP (volts)
terbuthylazine	230.026	174.1	6	10	25	8
1	422.099	405.1	116	10	27	16
4	455.092	362.2	116	10	41	16
5	483.113	362.1	86	10	39	14
6	467.114	178.1	111	10	73	8
8	450.430	178.1	106	10	73	8
9	493.500	341.2	21	10	29	16
10	429.470	341	116	10	29	16
11	491.323	405.2	146	10	39	24
13	401.207	384.2	81	10	25	24

DP: Declustering potential. EP: Entrance potential. CE: Collision energy. CXP: Collision cell exit potential

Valve:

	Total time (min)	Position
1	0	Waste
2	3.5	MS
3	6.0	Waste

The calibration curves and quality controls were obtained by preparing a stock solution in DMSO with a final concentration of 10 mM. The calibration curve ranges were set from 5 to 100000 nM. The QCs have a concentration of 100, 1000, and 10000 nM.

Preparation and handling of samples for LC-MS analysis:

The samples produced were stored at -20°C in Synovo's facilities until sample processing shortly prior to the HPLC/MS/MS process. The already processed samples were introduced directly into the auto-sampler or stored at 4 °C until measurement. The remaining samples were stored at -20 °C for further needs or requirements.

Plasma sample preparation for LC-MS analysis:

The samples were transferred into individual tubes and six volumes of ACN containing the IS (ACN-IS) were added to each sample (e.g. 10 µL plasma + 60 µL ACN-IS). After mixing and centrifuging for 5 min at 10000-11000 RCF (Eppendorf Centrifuge 5417R 10,000 rpm), the supernatant was transferred into a properly labelled glass auto-sampler vial.

When dilution of the samples was needed due to too high concentration or too little sample volume, the samples were diluted in a similar matrix as the samples (e.g. plasma from same animal strain). When diluting the samples, the dilution factor was considered in the data acquisition and subsequent calculations.

Tissue sample preparation (e.g. brain, liver) for LC-MS analysis:

The tissue samples were weighed and one volume of proteinase K solution was added. The tissue was digested by incubation with proteinase K at 50 °C for 1-3 h. After the incubation, the tissue is mechanically broken. The digested tissue was mixed with six volumes of ACN containing the internal standard. After centrifugation, the supernatant was taken and introduced in a properly labelled glass auto-sampler vial.

1.3 Results

MTT showed no cytotoxic activity for any of the candidate compounds

In order to evaluate possible cytotoxic effects of the tested compounds, an MTT assay was performed on splenocytes of Balb/c mice in triplicate using three different doses for each compound (1 nM, 10 nM and 100 nM). While compound **3** showed an increase of the metabolic activity of the cells at 1 nM and 10 nM (see **Figure 4a** and **b**), the assay showed that no cytotoxicity was observed.

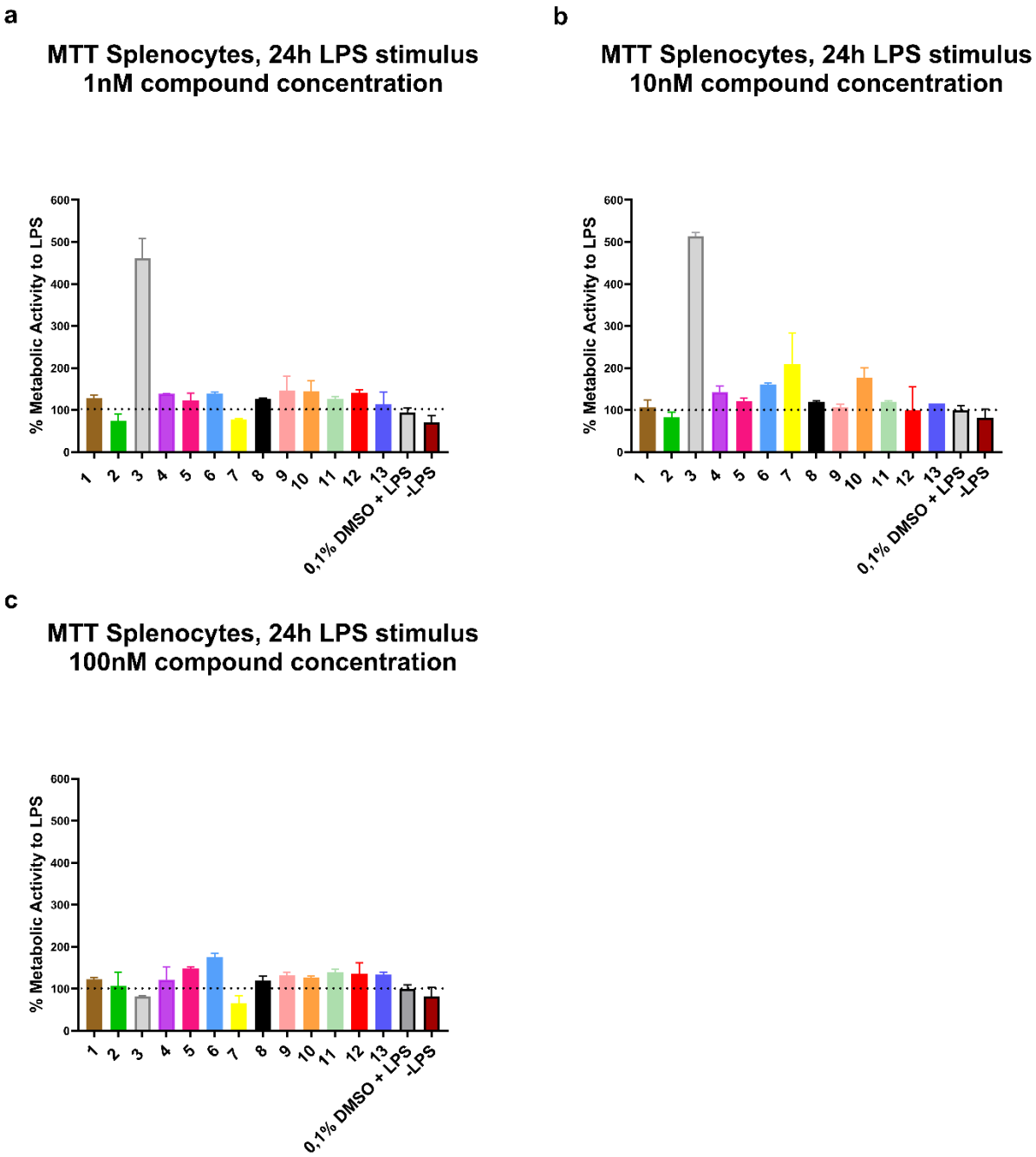

Figure 4. MTT assay on BALB/c splenocytes of inhibitors **1**, **2**, **3**, **4**, **5**, **6**, **7**, **8**, **9**, **10**, **11**, **12** and **13** at a) 1 nM, b) 10 nM and c) 100 nM. This Figure is adapted from: Tormählen NM. and Martorelli M. *et. al*. 2022.[27]

IL-6 and TNFα ELISA assay on splenocytes, MWB and HBC showed promising anti-inflammatory p38α MAP Kinase candidates

In order to evaluate potency *ex vivo* and *in vitro* of the compounds, an ELISA assay was performed on Balb/c splenocytes (n=3), C57BL/6 whole blood (n=3) and in HBC from three different donors using three different concentrations (1 nM, 10 nM and 100 nM). Inhibition activity of the different p38 MAP Kinase compounds was evaluated after measuring IL-6 and TNFα levels after LPS stimulus and compound exposure (24 h). The inhibition of these two pro-inflammatory cytokines showed that the ability to inhibit inflammatory processes varies between the different compounds. Compounds **2**, **3**, **4**, **7**, **8**, **10** and **12** showed no dose response in the reduction of the IL-6 and TNFα response in splenocytes' ELISA (see **Figure 5a** and **b**). Compound **12** showed no significant reduction of both pro-inflammatory cytokines in the MWB ELISA assay, while all the other p38 MAP Kinase inhibitors showed dose response reduction of the % of the release of IL6 and TNFα levels compared to the LPS control (see **Figure 6a** and **b**). Again, compounds **2**, **3**, **4**, **7**, **8**, **10** and **12** were found to be less active in the inhibition of both cytokines in the HBC ELISA assay if compared to compounds **1, 5, 6, 9, 11** and **13**. Overall, compounds **11** and **13** showed dose response and high IL-6 and TNFα inhibition in all the ELISA assays performed (**Table 4**, **Figure 5**-**7**). IC_{50} was calculated based on the data from the TNFα inhibition of the HBC ELISA assay (see **Table 5**), showing that in this assay compound **11** and **13** are among the most potent of all the tested compounds (IC_{50} = 1.3 ± 0.1 and 5.3 ± 0.6 nM, respectively).

Table 4. IL-6 and TNFα levels detected by ELISA. Values are % versus LPS untreated samples (100 %). *In vitro* data are the mean ± 1 standard deviation (3 biological replicates, each n = 3).

1 nM					
	IL-6			**TNFα**	
	11	**13**		**11**	**13**
Splenocytes	31 ± 1.7	34 ± 9.0	**Splenocytes**	9 ± 3.1	31 ±26.5
MWB	54 ± 7.8	31 ± 20.4	**MWB**	8 ± 1.2	13 ± 5.3
HBC	35 ± 10.4	44 ± 4.2	**HBC**	8 ± 6.7	35 ± 16.0

10 nM					
	IL-6			**TNFα**	
	11	**13**		**11**	**13**
Splenocytes	20 ± 10.7	14 ± 1.0	**Splenocytes**	5 ± 2.4	12 ± 3.0
MWB	47 ± 4.5	19 ± 11.4	**MWB**	6 ± 2.8	3 ± 2.5
HBC	17 ± 11.8	23 ± 4.1	**HBC**	7 ± 4.2	31 ± 18.5

100 nM					
	IL-6			**TNFα**	
	11	**13**		**11**	**13**
Splenocytes	0	14 ± 1.5	**Splenocytes**	3 ± 0.8	7 ± 1.0
MWB	45 ± 0.8	18 ± 10.3	**MWB**	4 ± 2.8	9 ± 7.0
HBC	2 ± 1.7	14 ± 1.2	**HBC**	5 ± 0.2	13 ± 4.9

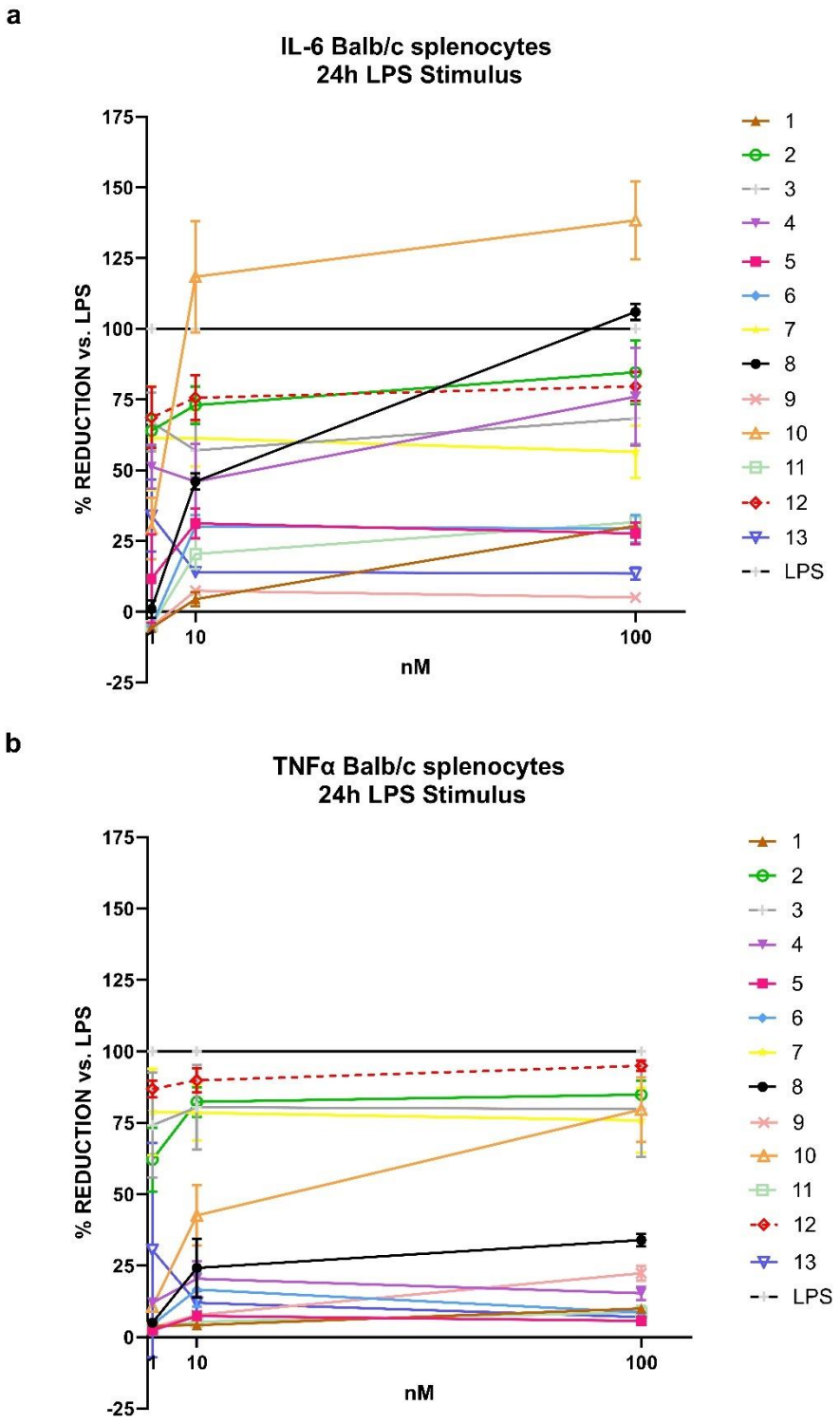

Figure 5. Reduction of IL-6 (**a**) and TNFα release (**b**) on BALB/c splenocytes of inhibitors **1, 2, 3, 4, 5, 6, 7, 8, 9, 10, 11, 12** and **13** after 24 h LPS stimulus (500 ng). This Figure is adapted from: Tormählen NM. and Martorelli M. *et. al*. 2022.[27]

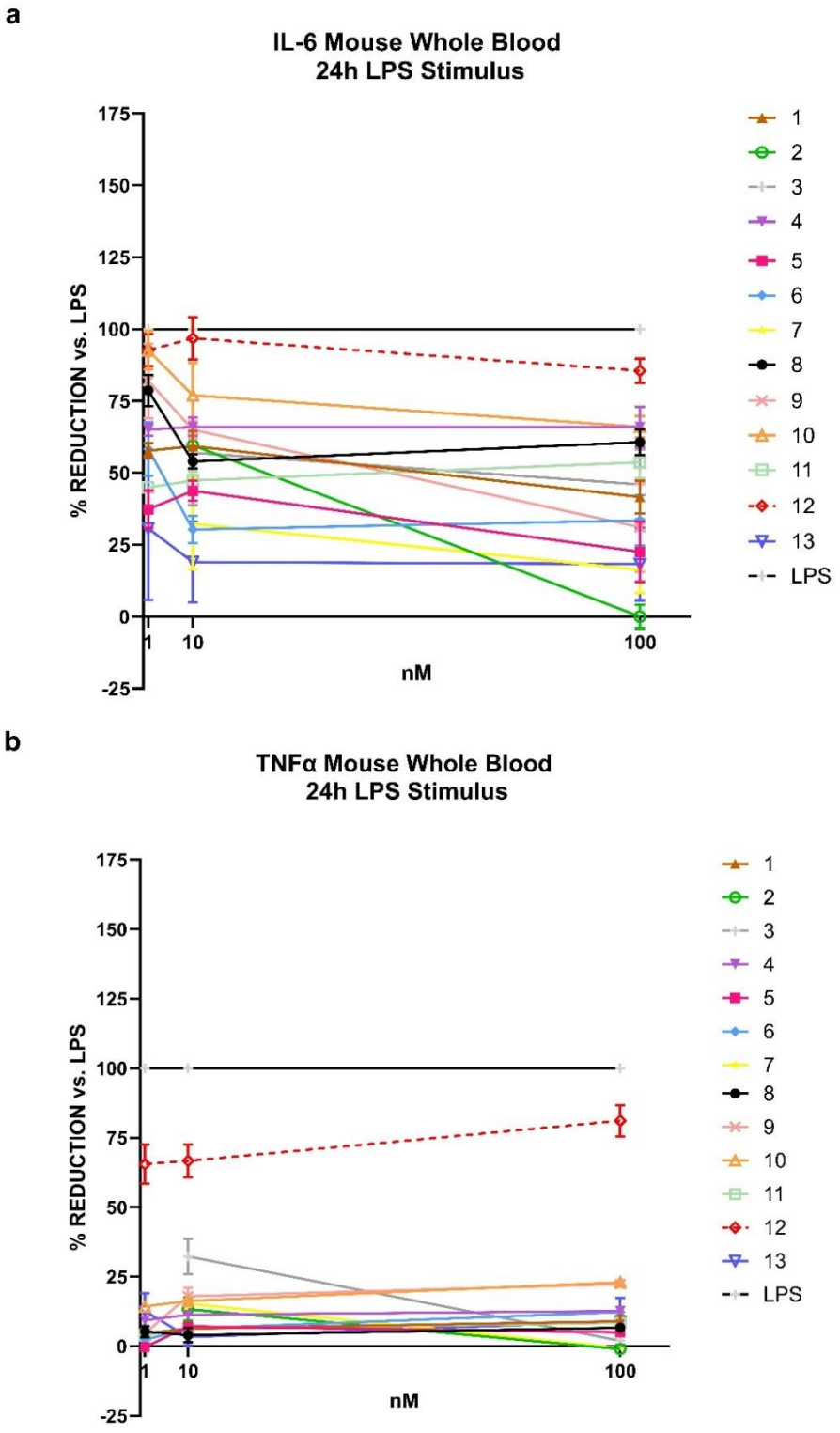

Figure 6. Reduction of IL-6 (**a**) and TNFα release (**b**) on C57BL/6 mouse whole blood of inhibitors **1, 2, 3, 4, 5, 6, 7, 8, 9, 10, 11, 12** and **13** after 24 h LPS stimulus (500 ng). This Figure is adapted from: Tormählen NM. and Martorelli M. *et. al*. 2022.[27]

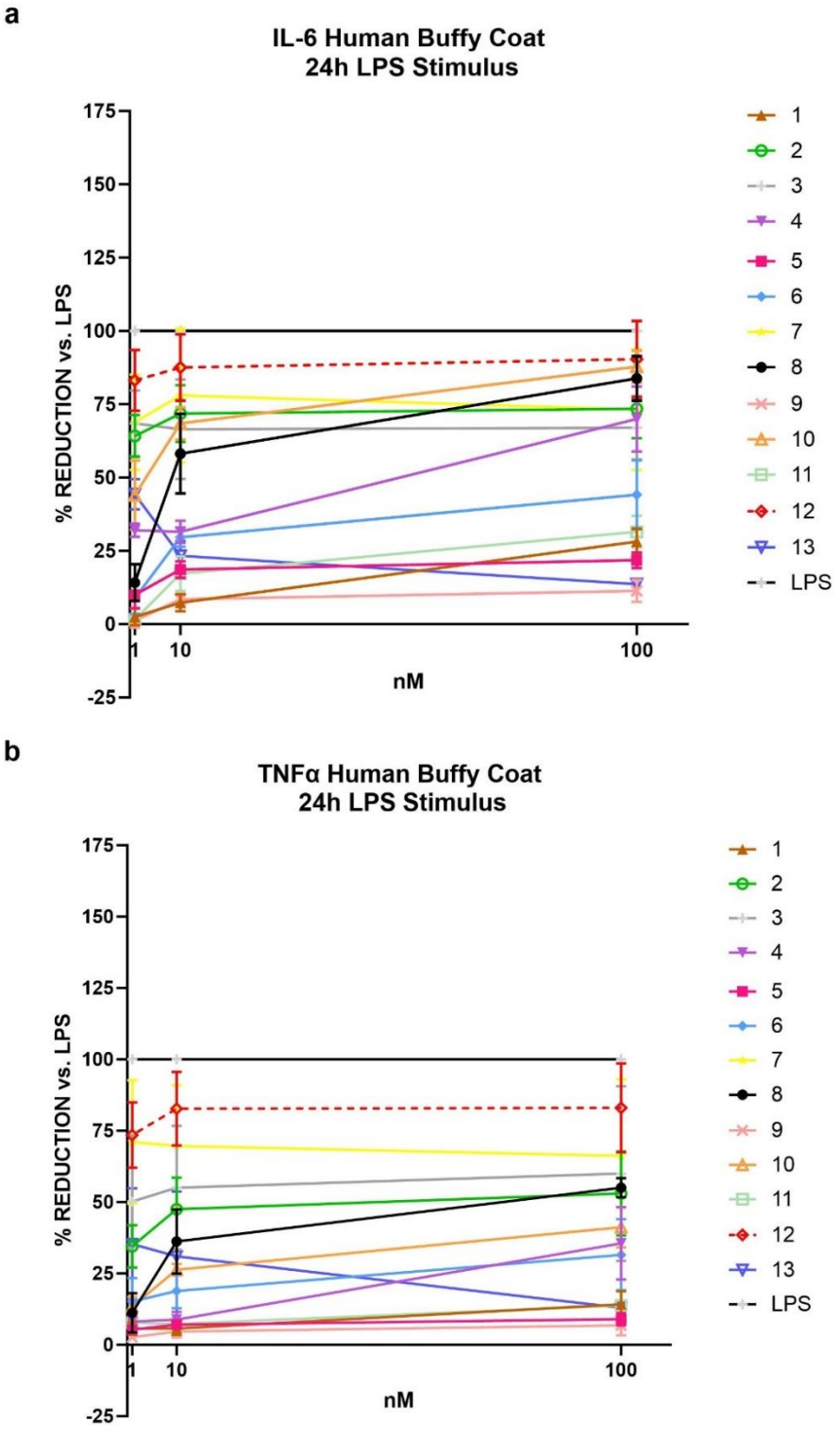

Figure 7. Reduction of IL-6 (**a**) and TNFα release (**b**) on human buffy coat of inhibitors **1, 2, 3, 4, 5, 6, 7, 8, 9, 10, 11, 12** and **13** after 24 h LPS stimulus (100 ng). This Figure is adapted from: Tormählen NM. and Martorelli M. *et. al*. 2022.[27]

Table 5. Inhibition of LPS-stimulated TNFα release from HBC. IC_{50} was estimated using the fitted line obtained for each compound, e.g.: Y= a*X + b, IC_{50}= (0.5 – b)/a.

Cpd.	IC_{50} [nM][a]	SEM
1	2.5	0.4
2	3.5	0.1
3	2.4	0.1
4	2.4	0.2
5	3.1	0.1
6	1.7	0.3
7	2.9	0.2
8	5.5	0.1
9	5.4	0.8
10	1.0	0.7
11	1.3	0.1
12	512	0.1
13	5.3	0.6

[a]mean value of two experiments

Uptake with HBC cells showed different cell pellet/supernatant ratio of the p38α MAP Kinase inhibitor compounds

HBC cells uptake was performed to test the *in vitro* cellular distribution of the selected compounds. Human peripheral leukocytes were incubated for 15 min and 240 min with the respective p38 MAP Kinase inhibitors (see **Table 6** and **7**). The uptake was evaluated

by calculating the ratio between cell pellet and supernatant concentration of each compound measured.

Table 6. Cell uptake at 15 min.

Cpd.	Medium (nM)	Cell (nM)	Cell (%)
1	45.18	30.81	68
4	50.17	50.53	101
5	78.82	32.17	41
6	78.03	81.07	104
8	68.81	45.54	66
9	54.29	24.47	45
10	134.52	15.55	12
11	41.79	67.50	162
13	44.64	37.57	84

Table 7. Cell uptake at 240 min.

Cpd.	Medium (nM)	Cell (nM)	Cell (%)
1	47.05	41.54	88
4	58.52	40.70	69
5	73.26	37.06	51
6	100.11	---	---
8	132.44	14.54	11
9	41.53	33.13	79
10	72.08	4.57	7
11	85.13	27.24	32
13	56.76	52.88	92

As expected, the selected compounds acted differently, while compounds **5**, **9** and **10** showed low cells versus supernatant ratio at 15 min, compounds **4**, **6**, **11** and **13** ratios were already above 80 % (**Table 6**). Uptake kinetics was evaluated by calculating the ratio at 240 min time point (**Table 7**). While compounds **6**, **8** and **10** showed values from 0 to

11 %, the other p38α MAP Kinase inhibitors were found to have a cell/supernatant ratio above 30 %.

Pharmacokinetic in C57BL/6-mice showed BBB-penetrant ability of some of the p38 MAP Kinase compounds

Briefly, in order to evaluate BBB penetration, peripheral organ availability and plasma levels of the respective inhibitors, 12-week-old, female C57BL/6-mice were treated either i.v. or p.o. with 0.4 mg/kg and 5 mL/kg of inhibitors **1**, **4**, **5**, **6**, **8**, **9**, **10, 11** and **13** in cassettes, with four compounds per cassette. The experiment was done using six different peripheral tail vein blood sampling time points: 5 min, 15 min, 30 min, 1 h, 2 h and 4h (see **Figure 8a** and **b**). Termination of animals was performed at two different time-points: 2 h and 4 h post substance application; compound concentrations were analyzed in heart plasma, liver, kidney, brain right hemisphere and brain left hemisphere by LC-MS.

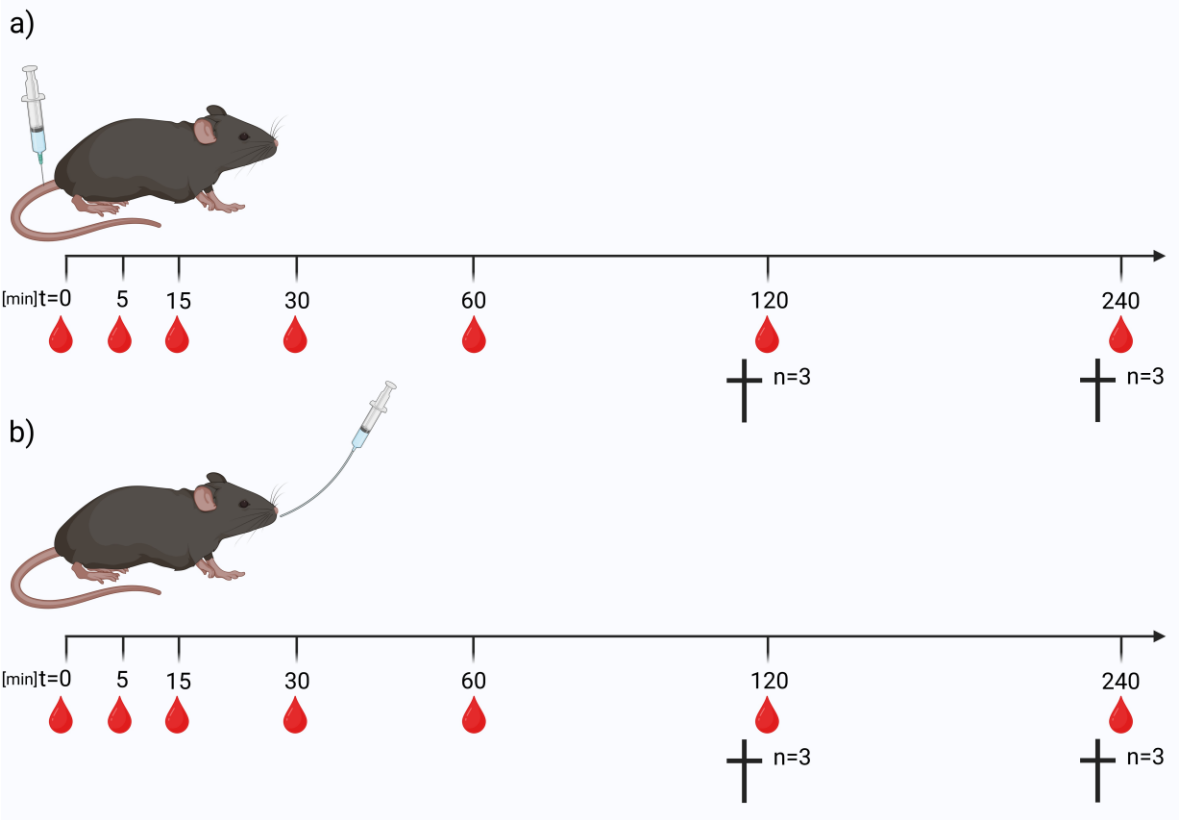

Figure 8. Overview of *in vivo* experiments in C57BL/6 mice; blood spots indicate timing of tail blood samples taken while the cross indicates termination time point, **a)** i.v. applications to study systemic bioavailability, **b)** p.o. applications to study oral bioavailability. All measurements were done with n=3 animals. This Figure is adapted from: Tormählen NM. and Martorelli M. *et. al*. 2022.[27]

Brain versus tail plasma ratio was calculated in order to evaluate BBB-penetrant compound either i.v. or/and p.o. injected. In both applications (i.v. and p.o.) compound **13** was found in the brain with a concentration of ~ 280 nM and ~ 372 nM respectively 240 min post injection (see **Table 15** and **Table 23**). Compound **10** displayed BBB-penetrance after p.o. application at the 240 min termination time point (~ 563 nM, see **Table 21**), but the brain versus tail plasma ratio was low if compared to compound **13**.

Table 8. In vivo data of **1** in C57BL/6-mice treated i.v. with 0.4 mg/kg.

Cpd.	time points (min)	tail plasma (nM)	heart plasma (nM)	liver (nM)	kidney (nM)	brain r. (nM)	brain l. (nM)	brain av. (nM)	brain/ plasma	AUCt	$t_{1/2}$ (min)
1	5	1									
	15	0									
	30	0									
	60	0									
	120	0	5	13	4	8	5	6.5	1.30		
	240	0	5	6	4	3	6	4.5	0.90	5	-

Table 9. In vivo data of **4** in C57BL/6-mice treated i.v. with 0.4 mg/kg.

Cpd.	time points (min)	tail plasma (nM)	heart plasma (nM)	liver (nM)	kidney (nM)	brain r. (nM)	brain l. (nM)	brain av. (nM)	brain/ plasma	AUCt	$t_{1/2}$ (min)
4	5	0									
	15	0									
	30	0									
	60	0									
	120	0	8	17	3	19	8	13.5	1.69		
	240	0	1	4	2	10	1	5.5	5.50	0	-

Table 10. In vivo data of **5** in C57BL/6-mice treated i.v. with 0.4 mg/kg.

Cpd.	time points (min)	tail plasma (nM)	heart plasma (nM)	liver (nM)	kidney (nM)	brain r. (nM)	brain l. (nM)	brain av. (nM)	brain/ plasma	AUCt	$t_{1/2}$ (min)
5	5	3									
	15	2									
	30	1									
	60	1									
	120	1	3	1	2	1	1	1	0.33		
	240	0	4	1	1	1	0	0.5	0.13	198	89

Table 11. In vivo data of **6** in C57BL/6-mice treated i.v. with 0.4 mg/kg.

Cpd.	time point (min)	tail plasma (nM)	heart plasma (nM)	liver (nM)	kidney (nM)	brain r. (nM)	brain l. (nM)	brain av. (nM)	brain/ plasma	AUCt	$t_{1/2}$ (min)
6	5	4									
	15	1									
	30	1									
	60	0									
	120	0	14	11	4	8	7	7.5	0.54		
	240	0	4	5	3	3	5	4	1.00	55	14

Table 12. In vivo data of **9** in C57BL/6-mice treated i.v. with 0.4 mg/kg.

Cpd.	time point (min)	tail plasma (nM)	heart plasma (nM)	liver (nM)	kidney (nM)	brain r. (nM)	brain l. (nM)	brain av. (nM)	brain/ plasma	$t_{1/2}$ (min)
9	5	25								
	15	11								
	30	6								
	60	3								
	120	1	1	21	2	1	2	1.5	1.50	
	240	1	1	13	2	1	0	0.5	0.50	56

Table 13. In vivo data of **10** in C57BL/6-mice treated i.v. with 0.4 mg/kg.

Cpd.	time points (min)	tail plasma (nM)	heart plasma (nM)	liver (nM)	kidney (nM)	brain r. (nM)	brain l. (nM)	brain av. (nM)	brain/ plasma	AUCt	$t_{1/2}$ (min)
10	5	32									
	15	14									
	30	11									
	60	10									
	120	7	9	28	8	5	6	5.5	0.61		
	240	5	7	10	7	5	6	5.5	0.79	1963	116

Table 14. In vivo data of **11** in C57BL/6-mice treated i.v. with 0.4 mg/kg.

Cpd.	time points (min)	tail plasma (nM)	heart plasma (nM)	liver (nM)	kidney (nM)	brain r. (nM)	brain l. (nM)	brain av. (nM)	brain/ plasma	AUCt	$t_{1/2}$ (min)
11	5	1									
	15	1									
	30	1									
	60	1									
	120	0	16	11	8	40	13	26.5	1.66		
	240	0	9	9	5	18	10	14	1.56	85	-

Table 15. In vivo data of **13** in C57BL/6-mice treated i.v. with 0.4 mg/kg.

Cpd.	time points (min)	tail plasma (nM)	heart plasma (nM)	liver (nM)	kidney (nM)	brain r. (nM)	brain l. (nM)	brain av. (nM)	brain/ plasma	AUCt	$t_{1/2}$ (min)
13	5	23									
	15	6									
	30	3									
	60	2									
	120	20	3	284	357	354	289	321	16.05		
	240	1	2	515	498	332	167	250	250		

Table 16. In vivo data of **1** in C57BL/6-mice treated p.o. with 0.4 mg/kg.

Cpd.	time points (min)	tail plasma (nM)	heart plasma (nM)	liver (nM)	kidney (nM)	brain r. (nM)	brain l. (nM)	brain av. (nM)	brain/ plasma	AUCt	$t_{1/2}$ (min)
1	5	2									
	15	1									
	30	1									
	60	1									
	120	1	3	3	1	0	3	1.5	0.50		
	240	1	4	2	1	0	2	1	0.25	240	545

Table 17. In vivo data of **4** in C57BL/6-mice treated p.o. with 0.4 mg/kg.

Cpd.	Time points (min)	tail plasma (nM)	heart plasma (nM)	liver (nM)	kidney (nM)	brain r. (nM)	brain l. (nM)	brain av. (nM)	brain/ plasma	AUCt	$t_{1/2}$ (min)
4	5	3									
	15	1									
	30	0									
	60	0									
	120	0	0	0	0	0	3	1.5	NA		
	240	0	0	0	0	0	1	0.5	NA	28	-

Table 18. In vivo data of **5** in C57BL/6-mice treated p.o. with 0.4 mg/kg.

Cpd.	time points (min)	tail plasma (nM)	heart plasma (nM)	liver (nM)	kidney (nM)	brain r. (nM)	brain l. (nM)	brain av. (nM)	brain/ plasma	AUCt	$t_{1/2}$ (min)
5	5	3									
	15	2									
	30	1									
	60	1									
	120	1	5	3	1	0	19	9.5	1.90		
	240	0	7	1	0	1	4	2.5	0.36	198	89

Table 19. In vivo data of **6** in C57BL/6-mice treated p.o. with 0.4 mg/kg.

Cpd.	time points (min)	tail plasma (nM)	heart plasma (nM)	liver (nM)	kidney (nM)	brain r. (nM)	brain l. (nM)	brain av. (nM)	brain/ plasma	AUCt	$t_{1/2}$ (min)
6	5	2									
	15	1									
	30	1									
	60	0									
	120	0	1	2	1	0	2	1	1.00		
	240	0	1	1	1	0	2	1	1.00	45	27

Table 20. In vivo data of **9** in C57BL/6-mice treated p.o. with 0.4 mg/kg.

Cpd.	time points (min)	tail plasma (nM)	heart plasma (nM)	liver (nM)	kidney (nM)	brain r. (nM)	brain l. (nM)	brain av. (nM)	brain/ plasma	AUCt	$t_{1/2}$ (min)
9	5	11									
	15	7									
	30	5									
	60	4									
	120	3	5	8	6	3	8	5.5	1.10		
	240	2	5	5	3	2	5	3.5	0.70	825	113

Table 21. In vivo data of **10** in C57BL/6-mice treated p.o. with 0.4 mg/kg.

Cpd.	time point (min)	tail plasma (nM)	heart plasma (nM)	liver (nM)	kidney (nM)	brain r. (nM)	brain l. (nM)	brain av. (nM)	brain/ plasma	AUCt	$t_{1/2}$ (min)
10	5	531									
	15	350									
	30	285									
	60	240									
	120	192	126	415	394	604	568	586	4.65		
	240	179	118	334	275	548	534	541	4.58	52263	188

Table 22. In vivo data of **11** in C57BL/6-mice treated p.o. with 0.4 mg/kg.

Cpd.	time point (min)	tail plasma (nM)	heart plasma (nM)	liver (nM)	kidney (nM)	brain r. (nM)	brain l. (nM)	brain av. (nM)	brain/ plasma	AUCt	$t_{1/2}$ (min)
11	5	83									
	15	39									
	30	21									
	60	17									
	120	14	16	12	9	10	32	21	1.31		
	240	11	15	11	8	9	25	17	1.13	4060	26

Table 23. In vivo data of **13** in C57BL/6-mice treated p.o. with 0.4 mg/kg**.**

Cpd.	time point (min)	tail plasma (nM)	heart plasma (nM)	liver (nM)	kidney (nM)	brain r. (nM)	brain l. (nM)	brain av. (nM)	brain/ plasma	AUCt	$t_{1/2}$ (min)
13	5	7									
	15	4									
	30	9									
	60	52									
	120	29	3	20	16	165	710	437	15.06		

Metabolic Stability

Inhibitors **11** and **13** were further evaluated for their metabolic stability in liver S9 fraction (the 9000g supernatant of a liver homogenate of human liver tissue) from different patients (**Table 24**). All the compounds investigated displayed excellent metabolic stability.

Table 24. Metabolic stability in liver S9 fraction summary from compound **11** and **13.**

11			
	peak area		
	n = 1	n = 2	n = 3
stabi	3,821,979	4,072,476	3,511,560
w/o S9	3,539,366	4,039,635	3,408,273
w/o Cof	3,637,444	3,748,968	4,057,365
Ph1	3,709,546	3,869,043	3,607,382
Ph2	3,698,285	3,396,009	3,719,245
Ph1+2	2,796,992	3,191,084	3,174,744

360 nm

11				
	peak area normalized to stabi			
	n=1	n=2	n=3	MV
stabi	100 %	100 %	100 %	100 %
w/o S9	93 %	99 %	97 %	96 %
w/o Cof	95 %	92 %	116 %	101 %
Ph1	97 %	95 %	103 %	98 %
Ph2	97 %	83 %	106 %	95 %
Ph1+2	97 %	86 %	99 %	94 %

13			
	peak area		
	n = 1	n = 2	n = 3
stabi	2,922,073	2,855,660	2,755,154
w/o S9	2,199,603	2,679,624	2,190,332
w/o Cof	2,869,666	2,988,692	2,679,351
Ph1	2,567,128	2.807,959	2,412,882
Ph2	3,152,951	2,673,802	2,653,592
Ph1+2	2,512,296	2,788,526	2,384,258

254 nm

13				
	peak area normalized to stabi			
	n=1	n=2	n=3	MV
stabi	100 %	100 %	100 %	100 %
w/o S9	75 %	94 %	79 %	83 %
w/o Cof	98 %	105 %	97 %	100 %
Ph1	88 %	98 %	88 %	91 %
Ph2	108 %	94 %	96 %	99 %
Ph1+2	86 %	98 %	87 %	90 %

1.4 Discussion

The aim of this study was to produce p38α MAP Kinase inhibitors with IC_{50} in the single digit nanomolar range, high brain-to-plasma ratios, ideally paired with high metabolic stability and a low level of side-effects. Because of their inhibitory activity, p38α MAP Kinase inhibitors are currently largely investigated for their potential use in different neurodegenerative disease such as AD and MS. Recent studies showed that Neflamapimod (**Figure 1a**, VX 745, described p38 MAP Kinase inhibitor)[17], selected for Phase II trials for the treatment of AD (NCT02423200, NCT02423122 & NCT03402659), but while it showed effects on amyloid removal and cognition, it failed at meeting its primary endpoint, the improvement of episodic memory in the REVERSE-SD trial, in a Phase II trial including 161 mild AD patients.[17,28] Neflamapimod was then discontinued due to side-effects (falls, nausea, headache, diarrhea, and upper respiratory tract infection) in clinical studies.[18] In support of my hypothesis that sees p38α MAP Kinase inhibitors as potential therapeutic drugs for neurodegenerative disease, another brain penetrant pryidinylpyridazine-based p38α MAP Kinase inhibitor MW150 (**Figure 1b**) was also investigated in diverse animal models of neurological disorders including models of AD.[11,19,20,21,22] The effective dose reported to improve results in the Morris water maze (MWM) on APP/PS1 mice was 2.5 mg/kg and due to its efficacy, pharmacodynamic data and safety profile, MW150 is currently being investigated in early stage clinical trials.[22]

In this study, 13 novel dibenzosuberone derivatives **1**-**13** (Skepinone-L and -N series) were characterized *in vitro* and *in vivo* in order to evaluate their ability to inhibit p38α MAP Kinase. The metabolic activity assay showed that none of the analyzed compounds were cytotoxic (**Figure 4**), while IL-6 and TNFα ELISA displayed that out of the 13 tested compounds, compound **10**, **11** and **13** were potent (**Figure 5-7**) with a TNFα IC_{50} in the single digit nanomolar range while compound **12** inhibitory activity resulted weak in both mice and human samples analyzed (TNFα IC_{50} = 512 ± 0.1 nM). In order to evaluate the pharmacokinetic activity, the same compounds were tested *in vivo* to evaluate organ distribution activity after p.o. and i.v. injections. It was observed that, while compounds **10** (p38α, IC_{50} = 1.0 nM) and **13** (p38α, TNFα IC_{50} = 5.3 nM) crossed the BBB (concentration in brain after 2 h and 0.4 mg/kg p.o. treatment, ~ 563 nM, ~ 372 nM) and displayed good brain-to-plasma ratios of 4.5 and 9.9, respectively (**Table 21** and **22**), compound **11** was not BBB-penetrant (**Table 22**). Also, none of the other inhibitors turned out to be BBB penetrant either after i.v. or p.o. application (**Tables 8-23**). Inhibitors **10**, **11** and **13** were further evaluated for their metabolic stability in HLMs, with all of them showing excellent metabolic stability (**Table 24**). The combination of a comparably high affinity for p38α MAP Kinase and comparably high CNS exposure has not been obtained for MW150 (p38α, IC_{50} = 230 nM). Results for compounds **10** (p38α, IC_{50} = 1.3 nM) and **13** (p38α, IC_{50} = 5.3 nM) suggest that these compounds have adequate potency and physical proprieties to effectively modulate p38α MAP Kinase activity in the brain.

1.5 Conclusion

The IC_{50}, metabolic stability and the organ affinity of 13 novel Skepinone-based p38α MAP Kinase inhibitors were characterized *in vitro* and *in vivo* respectively. Compounds **10**, **11** and **13** were further investigated based on their *in vitro* TNFα inhibition potency: the 3 inhibitors were selective and showed high metabolic stability. Due to these attributes and their good CNS distribution, compounds **10** and **13** are promising candidates for future studies investigating the role of p38α MAP Kinase inhibitors in the development of CNS pathology in murine models of CNS degeneration like MS and AD models. Compound **11**, as potent as the other two but not BBB-penetrant, could be used to better investigate the role of the peripheral inflammation, typically occurring in both diseases. To test this hypotheses, compounds **11** and **13** were tested in follow-up analysis in different inflammatory and neurodegenerative models of AD or MS (**Chapters 3** and **4** of the thesis).

Chapter 2

Influence of diet, age and MOG_{35-55}-peptide preparation on severity, survival, incidence and body weight in experimental autoimmune encephalomyelitis

Mariella Martorelli, Matthias Dengler, Julian Laux, Tina Fischer, Agne Vaiceliunaite, Ulrike Hahn, Thilo Weinstein, Santiago Cruces, Christina Pokoj, Luciano de Oliveira da Cunha, Lara Wohlbold, Pierre Koch, Stefan Laufer, Michael Burnet and Florian Maier. *A robust, high incidence and moderate severity form of EAE mediated by a low fiber diet and sonicated CFA/MOG emulsion.* Under peer review in the Journal of Neuroinflammation.

Abbreviations

%, Percentage;

°C, Celsius degree;

AD, Alzheimer's disease;

BBB, Blood-brain-barrier;

CFA, Complete Freund's Adjuvant;

CNS, Central nervous system;

CO_2, Carbon dioxide;

DMDs, Dimethyl disulfide;

EAE, experimental autoimmune encephalomyelitis;

HBC, Human Buffy Coat;

HCl, Hydrogen chloride;

i.p., Intra Peritoneal

IL1β, interleukin 1 beta;

IL-6, Interleukin 6;

MAP, Mitogen-activated protein;

MBP, Myelin Based protein;

MOG_{35-55}, Myelin Oligodendrocyte Glycoprotein;

MS, Multiple sclerosis;

NDF, Neutral Detergent Fiber;

OPCs, Oligodendrocyte Progenitor Cells;

p.o., Per oral;

pg, Picogram;

PTX, Pertussis Toxin;

qPCR, Quantitative Polymerase Chain Reaction;

ROS, Reactive Oxygen Species;

TMEV, Theiler's Murine Encephalomyelitis Virus;

TNFα, Tumor necrosis factor α.

2.1 Introduction

Multiple sclerosis (MS) is a chronic autoimmune disease that affects the central nervous system (CNS), which includes the brain and spinal cord. In MS, the immune system mistakenly attacks the protective covering of nerve fibers called myelin. Myelin acts as an insulating layer, facilitating the transmission of electrical signals along the nerve fibers. When myelin is damaged, the transmission of these signals is disrupted, leading to a wide range of neurological signs.[29]

The exact cause of multiple sclerosis is still unknown, but it is believed to involve a combination of genetic and environmental factors. Certain genetic variations have been identified that increase the risk of developing MS. Additionally, environmental factors such as viral infections, low levels of vitamin D, dietary habit and smoking have been associated with an increased risk of developing the disease.[30]

MS affects approximately 2.8 million people worldwide, according to estimates by the Multiple Sclerosis International Federation (MSIF). The disease predominantly affects young adults, with the majority of cases being diagnosed between the age of 20 and 50. MS is more prevalent in certain regions, such as Europe, North America, and Australia, compared to equatorial regions.[31]

The immune system plays a crucial role in the development and progression of MS. In MS, immune cells, particularly T cells, become activated and migrate into the CNS. These immune cells release inflammatory molecules that attack the myelin sheath, leading to its destruction. The resulting inflammation causes damage to the underlying nerve fibers and disrupts the normal functioning of the CNS.[32]

Various disease-modifying therapies (DMTs) are available to help manage MS and slow its progression. These treatments aim to modulate the immune system and reduce the frequency and severity of relapses, as well as delay the accumulation of disability. DMTs may include interferons, monoclonal antibodies, and other immunomodulatory drugs.[33]

The myelin oligodendrocyte glycoprotein 35-55 (MOG_{35-55})-peptide induced experimental autoimmune encephalomyelitis (EAE) model is a widely used animal model for studying MS, an autoimmune disease affecting the central nervous system. While EAE has provided valuable insights into MS pathogenesis, there are some challenges regarding reproducibility and translatability to the human model. Among all, the EAE model is known to have reproducibility issues. It has been shown that, even when using the same induction protocol, there is a variability in disease severity, incidence and progression among different EAE studies. This variability makes it difficult to compare results across different laboratories or reproduce findings consistently.[34] In addition, the lack of standardization of the EAE model is often due to the induction protocols that can vary in various factors such as the choice of antigen, adjuvants, administration route, and dosing

regimen. This lack of standardization contributes to the challenges in reproducing experimental results. Moreover, the strain dependency can play a key role in the lack of reproducibility of this model: The susceptibility to EAE and its phenotype can vary among different mouse or rat strains. This strain dependency further complicates the reproducibility of EAE studies, as findings in one strain may not hold true for others.[35]

Due to the complex nature of MS and the variation in disease manifestation, the translatability issues of the EAE model to humans are well known. These are due to different causes: a) Immunopathological differences. EAE is induced by actively sensitizing animals with myelin antigens, leading to the development of autoimmune inflammation in the central nervous system. However, the immunopathological mechanisms and the immune cell populations involved in EAE may not fully recapitulate the complexity of human MS. This disparity limits the direct translation of findings from EAE studies to human disease; b) Lack of remyelination: One hallmark of MS is the demyelination of nerve fibers, which can be followed by varying degrees of remyelination. In contrast, EAE models often lack substantial remyelination, making it challenging to study this critical aspect of MS pathology; c) Therapeutic responses: Some therapeutic strategies that show promise in EAE models have not been as successful in human clinical trials. This discrepancy suggests that the response to treatment can differ between the two systems, highlighting the limitations in translatability.[30,34]

It is important to note that despite these limitations, the EAE model continues to be valuable for studying certain aspects of MS and developing potential therapeutic approaches. However, caution should be exercised when interpreting and extrapolating findings from EAE studies to human MS.

The EAE model, like many other disease models, can be influenced by various factors, including diet. While there is limited research specifically addressing the effects of diet on EAE, some studies have investigated the impact of specific dietary components on disease outcome. It has been shown that iron is an essential nutrient involved in various physiological processes, including immune function. Studies have suggested that iron levels can influence the severity of EAE. High iron levels have been associated with increased disease severity and immune dysregulation in EAE models.[36–38]

A recent study demonstrates that protein content in the diet is crucial for maintaining overall health and immune function. Limited evidence suggests that protein intake may affect EAE outcomes. One study demonstrated that a low-protein diet reduced EAE severity and delayed disease onset in mice. However, more research is needed to establish the precise role of protein in EAE.[39]

Vitamin E is an antioxidant known for its immunomodulatory properties. Some studies have investigated the effects of vitamin E supplementation in EAE models, with mixed results. While vitamin E has shown potential protective effects against EAE in some

studies, others have reported no significant impact. Further research is required to clarify its role in EAE.[40,41]

It is also known that high sugar intake has been associated with chronic inflammation and increased risk of various diseases. However, the direct influence of sugar on EAE remains largely unexplored. Given the potential pro-inflammatory effects of excessive sugar consumption, it is reasonable to speculate that it could exacerbate inflammation in EAE. However, more research is needed to establish a definitive link.[42]

Different studies show that dietary fiber has been recognized for its beneficial effects on overall health, including modulation of the gut microbiota and immune system. While there is limited research specifically on fiber in EAE, studies in other inflammatory conditions suggest that fiber-rich diets may have immunomodulatory effects. These effects could potentially influence EAE outcome, but more research is needed in this area.[43]

It is important to note that the studies cited above may not directly address the influence of these dietary components on EAE. Further research is necessary to fully understand the specific effects of diet on EAE outcome and to establish dietary recommendations for individuals with MS. Yet, similar to MS, EAE is also heterogeneous, characterized by high variability of both disease incidence and course.[44]

The variability between protocols introduces discrepancies in clinical disease and CNS pathogenesis, limiting the comparability between studies and slowing much-needed translational research.[45]

Secondly, for a robust induction of EAE, the preparation and viscosity of the MOG_{35-55}-peptide emulsion and pertussis toxin (PTX) doses, used to induce the EAE phenotype play important roles. Additionally, considering that more mature animals develop a trained and tolerogenic immune system, the role of the age and immunological maturity of the mice were also investigated.[46] For this reason, with the objective to establish a robust EAE model displaying high incidence, little phenotypic variability and strong reproducibility, I systematically evaluated the above listed factors for their impact on the EAE induction in adolescent (14 weeks old) and aged (33 weeks old) female C57BL/6 mice. Establishing a stable protocol to reliably induce a homogenous disease phenotype in mice is essential for obtaining a solid, reproducible in vivo model in order to get reliable results to drug efficacy testing.

Aim

The objective of this study was to optimize a robust EAE model with high incidence, low variability, but with only moderate severity to reliably induce a homogenous disease phenotype in mice that is essential for obtaining a solid, reproducible in vivo model in order to get reliable results to drug efficacy testing. Furthermore, I aimed to proove the theory that animal age and immune system training has a major impact on disease severity in the EAE model. To this end, diet and CFA/MOG emulsion preparation were systematically evaluated for their impact on EAE induction in adolescent (14 weeks old) and mature (33 weeks old) female C57BL/6 mice. AIN 93M (low fiber) and VRF1 (high fiber) diet were tested in combination with two different CFA/MOG emulsion preparation methods (sonicated versus un-sonicated). The Incidence and severity of this murine model was detected by different techniques: **a**) *in vivo* parameters such as body weight loss and EAE disease scoring, **b**) qPCR methodic with selected markers for reflecting infiltration, inflammation and demyelination processes, **c**) histological findings to determin myelin loss and astrocyte proliferation in brain and spinal cord.

2.2 Material and Methods

Induction materials:

Heat-inactivated M. tuberculosis (strain H37RA) and Complete Freund's Adjuvant (CFA) (1 mg/mL heat-inactivated mycobacterium tuberculosis) were both obtained from Difco, Product No. 11719062, USA; the murine MOG_{35-55}-peptide (MEVGWYRSPFSRVVHLYRNGK) was obtained from Panatecs, Product No. AU-P-3596, Germany while Pertussis toxin was obtained from Sigma Aldrich, Germany.

Diets:

The certified, cereal-based rodent diet SM R/M-Z VRF1 and the purified EF R/M acc. AIN 93M diet from SSNIFF® Spezialdiäten GmbH, Soest, Germany were used as experimental diets as indicated in Figure 9. *V 1534 - 000* SSNIFF® R / M-H, 10 mm mouse and rat fortified complete maintenance diet served as a control diet. The control diet is, among other ingredients, composed of grain and grain by-products, and oil seed products, which may vary due to seasonal crop. This also applies for the VRF1-diet, while seasonality of crop is no influence factor on the AIN 93M-diet due to the purified nature of ingredients.

Table 25. Overview of relevant differences in composition between the experimental diets VRF1 and AIN 93M, thought to impact disease manifestation in both EAE and human MS. Detailed description of diet content is listed in **Table 26**, **27** and **28**. NDF: neutral detergent fiber.

Diet	VRF1	AIN 93M	Control diet
Protein (% of total kJ)	23	13	24
Sugar (%)	5.6	11.2	5.4
NDF (%)	16.3	-	16.9
Crude fiber (%)	4.5	5.0	5.0
Vitamin E (mg/kg)	135	75	110
Iron (mg/kg)	185	47	189

Table 26. Description of the AIN 93M Control Diet for rodents – maintenance: This purified diet corresponds to the diet published by the American Institute of Nutrition (AIN). This diet was designed for the maintenance of rats and mice. Although the concentrations of the macro- and micronutrients are low, all requirements will be met with that diet.

		MJ/kg	KJ %	[%]	per kg
Gross Energy (GE)		18.0			
Metabolizable Energy (ME)		15.6			
Fat			10		
Protein			13		
Carbohydrates			77		
Crude Nutrients	Crude protein			12.3	
	Crude Fat			4.1	
	Crude fiber			5.0	
	Crude ash			3.0	
	Starch			44.8	
	Dextrin			15.3	
	Sugar			11.2	
	N free extracts			71.8	
Minerals	Calcium			0.55	
	Phosphorus			0.36	
	Ca / P			1.55 : 1	
	Sodium			0.16	
	Magnesium			0.09	
	Potassium			0.54	
Fatty Acid	C 12:0			-	
	C 14:0			0.02	
	C 16:0			0.50	
	C 17:0			0.01	
	C 18:0			0.15	
	C 20:0			0.02	
	C 16:1			0.01	

	C 18:1			1.03	
	C 18:2			2.11	
	C 18:3			0.23	
Amino Acids	Lysine			1.03	
	Methionine			0.38	
	Cystine			0.23	
	Met+Cys			0.61	
	Threonine			0.54	
	Tryptophan			0.16	
	Arginine			0.69	
	Histidine			0.37	
	Valine			0.86	
	Isoleucine			0.70	
	Leucine			1.23	
	Phenylalanine			0.64	
	Phe+Tyr			1.29	
	Glycine			0.25	
	Glutamic acid			2.78	
	Aspartic acid			0.92	
	Proline			1.41	
	Serine			0.74	
	Alanine			0.37	
Vitamins	Vitamin A				4,000 IU
	Vitamin D_3				1,000 IU
	Vitamin E				75 mg
	Vitamin K				4 mg
	Thiamine (B_1)				12 mg
	Riboflavin (B_2)				16 mg
	Pyridoxine (B_6)				7 mg
	Cobalamin (B_{12})				25 mg
	Nicotinic acid				29 mg
	Pantothenic acid				15 mg
	Folic acid				2 mg
	Biotin				200 mg
	Choline				980 mg
Trace elements	Iron				47 mg
	Manganese				21 mg
	Zinc				39 mg
	Copper				10 mg
	Iodine				0.3 mg
	Selenium				0.2 mg

Table 27. Description of the VRF1-Breeding Diet composition, fortified (autoclavable / γ-irradiated), complete feed for mice and rats: This diet has been designed for the breeding of rats and mice. The dietary nutrients contents and the energy density are adjusted to the high-

performance during reproduction to meet the increased nutrient requirements. This diet is fortified for sterilization processes.

		MJ/kg	KJ %	[%]	per kg
Gross Energy (GE)		16.6			
Metabolizable Energy (ME)		14			
Fat			13		
Protein			23		
Carbohydrates			64		
Crude Nutrients	Crude protein			19	
	Crude Fat			5.0	
	Crude fiber			4.5	
	NDF			16.3	
	ADF			6.9	
	Crude ash			6.3	
	Starch			34.8	
	Sugar			5.6	
	N free extracts			53.9	
Minerals	Calcium			0.90	
	Phosphorus			0.65	
	Ca / P			1.38 : 1	
	Sodium			0.30	
	Magnesium			0.27	
	Potassium			0.95	
Fatty Acid	C 12:0			-	
	C 14:0			0.02	
	C 16:0			0.62	
	C 18:0			0.16	
	C 20:0			0.02	
	C 16:1			0.03	
	C 18:1			1.13	
	C 18:2			2.70	
	C 18:3			0.30	
Amino Acids	Lysine			1.42	
	Methionine			0.67	
	Cystine			0.34	
	Met+Cys			1.01	
	Threonine			0.70	
	Tryptophan			0.24	
	Arginine			1.16	
	Histidine			0.48	
	Valine			0.91	
	Isoleucine			0.79	
	Leucine			1.41	
	Phenylalanine			0.88	
	Phe+Tyr			1.49	
	Glycine			0.86	

	Glutamic acid			4.00	
	Aspartic acid			1.85	
	Proline			1.29	
	Serine			0.98	
	Alanine			0.88	
Vitamins	Vitamin A				25,000 IU
	Vitamin D_3				1,500 IU
	Vitamin E				135 mg
	Vitamin K				20 mg
	Thiamine (B_1)				87 mg
	Riboflavin (B_2)				33 mg
	Pyridoxine (B_6)				31 mg
	Cobalamin (B_{12})				150 mg
	Nicotinic acid				145 mg
	Pantothenic acid				59 mg
	Folic acid				10 mg
	Biotin				720 mg
	Choline				1,450 mg
Trace elements	Iron				185 mg
	Manganese				62 mg
	Zinc				88 mg
	Copper				15 mg
	Iodine				2.1 mg
	Selenium				0.3 mg

Table 28. Description of Rat/Mouse-Maintenance Complete feed for mice and rats diet: This diet has been designed for rats and mice and is suitable for long term experiments (e.g., chronic toxicity studies), because of the moderate energy density and the very low nitrosa-mine contents.

		MJ/kg	**KJ %**	**[%]**	**per kg**
Gross Energy (GE)		16.2			
Metabolizable Energy (ME)		13.5			
Fat			9		
Protein			24		
Carbohydrates			67		
Crude Nutrients	Crude protein			19	
	Crude Fat			3.3	
	Crude fiber			5.0	
	NDF			16.9	
	ADF			7.1	
	Crude ash			6.4	
	Starch			35.9	
	Sugar			5.4	
	N free extracts			54.6	
Minerals	Calcium			1.00	
	Phosphorus			0.70	

	Ca / P			1.43 : 1	
	Sodium			0.24	
	Magnesium			0.22	
	Potassium			0.92	
Fatty Acid	C 12:0			-	
	C 14:0			0.01	
	C 16:0			0.45	
	C 18:0			0.09	
	C 20:0			0.01	
	C 16:1			0.01	
	C 18:1			0.62	
	C 18:2			1.76	
	C 18:3			0.23	
Amino Acids	Lysine			1.00	
	Methionine			0.33	
	Cystine			0.35	
	Met+Cys			0.68	
	Threonine			0.71	
	Tryptophan			0.25	
	Arginine			1.19	
	Histidine			0.48	
	Valine			0.90	
	Isoleucine			0.79	
	Leucine			1.39	
	Phenylalanine			0.88	
	Phe+Tyr			1.49	
	Glycine			0.86	
	Glutamic acid			4.10	
	Aspartic acid			1.79	
	Proline			1.29	
	Serine			0.99	
	Alanine			0.82	
Vitamins	Vitamin A				15,000 IU
	Vitamin D_3				1,100 IU
	Vitamin E				110 mg
	Vitamin K				7 mg
	Thiamine (B_1)				18 mg
	Riboflavin (B_2)				22 mg
	Pyridoxine (B_6)				21 mg
	Cobalamin (B_{12})				100 mg
	Nicotinic acid				115 mg
	Pantothenic acid				40 mg
	Folic acid				7 mg
	Biotin				510 mg
	Choline				1,370 mg
Trace elements	Iron				189 mg

	Manganese				68 mg
	Zinc				91 mg
	Copper				15 mg
	Iodine				2.1 mg
	Selenium				0.3 mg

Preparation and administration of CFA/MOG$_{35-55}$-peptide emulsion:

First, to ensure homogeneity, two vials each containing 10 mL of CFA (1 mg/mL heat-inactivated mycobacterium tuberculosis) were thoroughly mixed. Subsequently, the contents of both CFA vials were transferred into a 50 mL centrifuge tube and mixed. Then, an additional 100 mg of heat-inactivated mycobacterium tuberculosis (MT) was added to the mixture, vortexed and thoroughly mixed for a final CFA concentration solution of 6 mg/mL MT in 20 mL final volume. Secondly, the MOG$_{35-55}$-peptide solution was prepared at RT with a final concentration of 4 mg/mL (300 µg MOG final concentration) or 2mg/mL (150 µg MOG final concentration) in 1X PBS. Both the prepared MOG$_{35-55}$ solution and CFA stock were kept on ice until processing. Using a 1 mL pipet with filter tips, 1 mL of MOG$_{35-55}$-peptide solution was then added into a 5 mL syringe and 1 mL of CFA-solution was then added into a second 5 mL syringe. Both syringes, one containing 1 mL CFA and the other containing 1 mL of the MOG$_{35-55}$-peptide solution, were connected to each other with a 3-way valve connector. The contents were mixed by vigorous up- and down- pipetting several times until a homogeneous emulsion was obtained (non-sonicated groups). For the groups with sonication steps (sonicated groups), the syringe containing the emulsion was disconnected from the 3-way valve. Subsequently, these samples were dipped into a 0.34 cm diameter ultra-sonicator (Hielscher Ultrasonics, UP50H, No. 35039908/1) and sonicated 4-times with 70 % amplitude for 10 s. The syringe containing the sonicated emulsion was again connected to the 3-way valve connector and the whole process was repeated three times. Taking care to avoid any air bubbles, these emulsions were then transferred to 1 mL syringes. Each mouse was then injected subcutaneously with 150 µL (equaling 300 µg or 150 µg MOG$_{35-55}$-peptide per mouse) of either the non-sonicated or the sonicated emulsion at the base of the tail (100 µL on one side of the tail-base, 50 µL on the other side, alternating between mice for randomization).

Preparation and injection of PTX solution:

The PTX stock was freshly prepared by diluting powdered PTX with sterile 1X PBS to a final concentration of 1.2 µg/mL (240 ng) or 0.6 µg/mL (120 ng). The first PTX-injection (i.p.) was done immediately after the administration of the MOG$_{35-55}$-peptide emulsion, the second PTX-injection (i.p.) was given 48 h after the first. Groups were either injected with 240 ng or with 120 ng PTX on both days (**Table 31** and **32**).

Animals:

7-week-old female C57BL/6 mice were obtained from Janvier Labs. Before the study was initiated, an acclimation phase of seven days was necessary. In Study 1, in order to determine short to moderate term dieting effects, animals were held six weeks prior to MOG/PTX induction on the respective distinctly different test-diets (**Figure 9**). In the second study, to evaluate long-term feeding effects, each group, consisting of four animals for the Control diet group, eight animals in the AIN 93M and VRF1 groups, were pre-fed with the respective diet for 24 weeks (**Figure 9**). In both studies, animals were provided with respective food and water ad libitum and on day 0 induced with MOG_{35-55}-peptide sonicated or non-sonicated emulsion and PTX (**Figure 10** and **11**). Euthanasia was performed by CO_2 inhalation, either at study termination or upon reaching pre-defined termination criteria (either due to animal welfare or satellite animals in study 2) (**Figure 9**). Brain and spinal cord samples were collected for qPCR (flash-frozen in liquid nitrogen and stored at -80 °C until processing) and for histological samples (directly transferred to 4 % PFA, and 24 h later stored in 70 % EtOH until further workup, see histology paragraph of the Materials and Methods section). Ethical approval for the study was obtained from local authorities (Regierungspräsidium Tübingen).

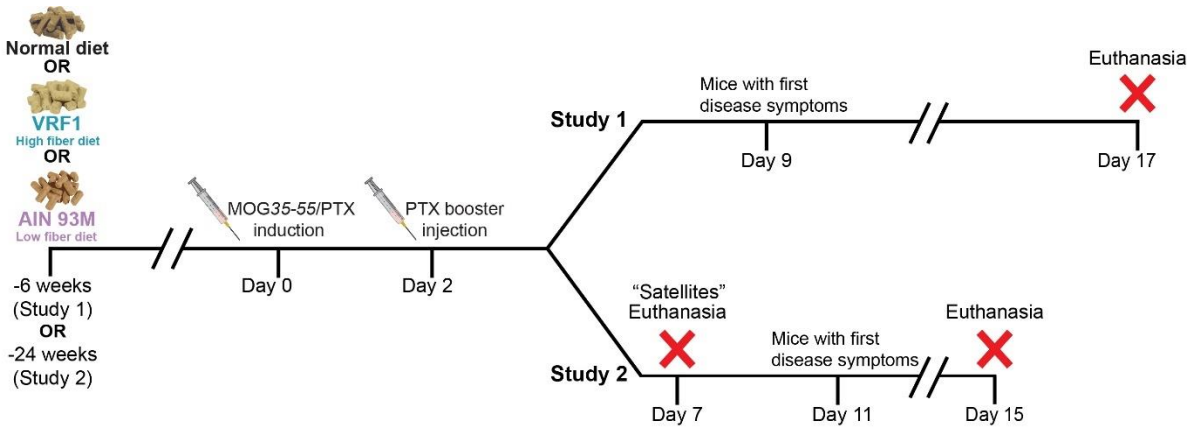

Figure 9. C57BL/6 female mice were pre-fed for six weeks (Study 1) and 24 weeks (Study 2) with three different diets. Then, EAE was induced by subcutaneous injection of differing MOG_{35-55}-CFA emulsion preparations. MOG_{35-55}-peptide was administered either as a sonicated (+son) or non-sonicated (-son) emulsion. PTX i.p. injection was done on days 0 and 2 (relative to MOG_{35-55}-injection), while satellite animals were terminated for study 2 on day 7 post induction. On day 17, Study 1 mice were euthanised; for Study 2, animals were euthanised on day 14 post MOG_{35-55}-injection. This Figure is adapted from Martorelli *et.al*. 2024, under revision.

Figure 10. Scheme of variables examined in Study 1: different diet compositions (Control diet, VRF1 and AIN 93M respectively) and variations in MOG_{35-55}-peptide emulsion preparation (+son versus -son). This Figure is adapted from Martorelli *et.al*. 2024, under revision.

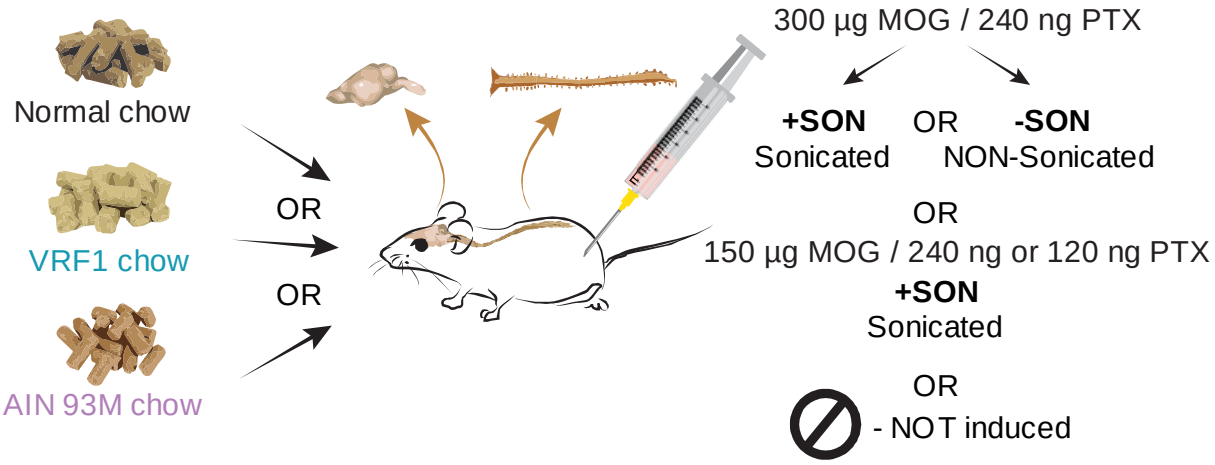

Figure 11. Scheme of variables examined in Study 2: different diet compositions (Control diet, VRF1 and AIN 93M respectively), variations in MOG_{35-55} peptide dose (150 µg versus 300 µg) and emulsion preparation (+son versus -son), and variation of PTX dose (120 ng versus 240 ng). This Figure is adapted from Martorelli *et.al*. 2024, under revision.

Clinical observations were detected according to a standardized scoring system (see **Table 29**). Body weight was assessed daily, starting on day 1 until the end of the experiment. Exemptions being day 0, where, in order to avoid additional stress for the mice that could impact disease development, the weighing was skipped. The scoring was evaluated by the same operator daily, beginning on the respective day of symptom-onset. Incidence is calculated as percentage of symptomatic mice (EAE score ≥ 0.5) per time-point.

Table 29. Mouse EAE Scoring system.

Score	***Clinical observation***
0	No obvious changes in motor function compared to non-immunized mice. When picked up by the tail base, the tail has tension and is erect. Hind legs are usually spread apart. When the mouse is walking, there is no gait or head tilting.
0.5	Tip of tail is limp. When picked up by the tail base, the tail has tension except for the tip. Muscle straining is felt in the tail, while the tail continues to move.
1.0	Limp tail. When picked up by base of tail, instead of being erect, the whole tail drapes over finger. Hind legs are usually spread apart. No signs of tail movement are observed.
1.5	Limp tail and hind leg inhibition. When picked up by base of tail, the whole tail drapes over finger. When the mouse is dropped on a wire rack, at least one hind leg falls through consistently. Walking is very slightly wobbly.
2.0	Limp tail and weakness of hind legs. When picked up by base of tail, the legs are not spread apart, but held closer together. When the mouse is observed walking, it has a clearly apparent wobbly walk. One foot may have toes dragging, but the other leg has no apparent inhibitions of movement.
2.5	Limp tail and dragging of hind legs. Both hind legs have some movement, but both are dragging at the feet (mouse trips on hind feet). - or – No movement in one leg/completely dragging one leg, but movement in the other leg.
3.0	Limp tail and complete paralysis of hind legs (most common). - or – Limp tail and almost complete paralysis of hind legs. One or both hind legs are able to paddle, but neither hind leg is able to move forward of hind hip.

3.5	Limp tail and complete paralysis of hind legs. In addition to: Mouse is moving around the cage, but when placed on its side, is unable to right itself. Hind legs are together on one side of the body. - or – Mouse is moving around the cage, but the hind quarters are flat like a pancake, giving the appearance of a hump in the front quarters of the mouse.
4.0	Limp tail, complete hind leg and partial front leg paralysis. Often euthanasia is recommended after the mouse scores 4,0 for 2 days. However, with daily s.c. fluids most C57BL/6 mice may recover to 3,5 or 3,0, while SJL mice may fully recover even if they reach score 4,0 at the peak of disease. When the mouse is euthanized because of severe paralysis, a score of 5,0 is entered for that mouse for the rest of the experiment.
4.5	Complete hind and partial front leg paralysis, no movement around the cage. Mouse is not alert. Mouse has minimal movement in the front legs. Mouse barely responds to contact. Euthanasia is recommended.
5.0	Mouse is euthanized because of severe paralysis (e.g., a score of 4 or greater for 2 consecutive days), a score of 5,0 is entered for that mouse for the rest of the experiment. - or – Mouse is found dead due to paralysis.

Total RNA isolation and quantitative RT-PCR:

Using a FastPrep-24 5G instrument (MP Biomedicals), flash frozen brain and spinal cord samples were homogenized in lysis buffer (Jena Bioscience). Total RNA was isolated using Total RNA Purification Kit (Jena Bioscience) according to the manufacturer's instructions. RNA quantity and purity were evaluated spectrophotometrically with the Nanodrop NP-80 instrument (Implen). After DNase I treatment (PerfeCTa DNase I, Quanta Bioscience), 500 ng of total RNA was transcribed into cDNA with 5x PrimeScript RT Mastermix (Takara). using Blue S'Green qPCR Mix Separate ROX (Biozym) according to the manufacturer´s instructions, the qPCR reaction was performed on the QuantStudio® 3 real-time polymerase chain reaction (PCR) system (ThermoFisher Scientific/Quantstudio™ Design & Analysis Software v.1.4.3). Relative expression levels were determined using the

2−ΔΔCT method and HPRT was used as reference gene[47] and the Control diet not-induced animals were used as control group. Primer sequences are listed in **Table 30**. In the spinal cord analysis, IL-10 marker was not evaluated due to insufficient sample material and observed signals being below the lower limit of detection (see **Figure 14**, **16** and **19**).

Table 30. Primer list used for quantitative RT-PCR

Gene	Forward Primer	Reverse Primer
Hprt	AGTTCTTTGCTGACCTGCTG	CCACCAATAACTTTTATGTCCCC
Mbp	CGAGGAGAGGCTGGAAAGAA	TGCTTGGAGTCTGTCACCG
Gm-csf	GGGGCAATTTCACCAAACTCAA	TCCGCATAGGTGGTAACTTGT
H2-Ab1	TGCAGACACAACTACGAGGG	TGAGCAGACCAGAGTGTTGT
Mog	TTGTGGAGCTTCTCTTGGCC	GTACCAACCCACCTCCATGC
Gfap	GCAAGAGACAGAGGAGTGGT	ACTCCAGATCGCAGGTCAAG
Olig2	CCACACACACACCTTTTGCC	CACGTTGTAATGCAGGTCGC
Foxp3	TCGAGGAGCCAGAAGAGTTT	AGACTGCACCACTTCTCTCT
IL-10	AGAGAAGCATGGCCCAGAAA	CTCCACTGCCTTGCTCTTATTT
Cspg4	GACCAACCCCCTGTTCTCAC	TGGGCCCGAATCATTGTCTG
Tbx21	CAAGGGGGCTTCCAACAATG	GCTCTCCATCATTCACCTCCA

Histology instruments:

Histological preparation of samples was performed using a paraffin dispenser fitted with an MPS/S dispensing module (SLEE Medical), Paraplast Plus (Leica BioSystem, art.-no. X881.1 REF 39602004). An HM325 Manual Microtome (Leica BioSystem) was used to perform 5 µm cuts. Cuts were mounted on glass Superfrost PLUS or Superfrost R (Langenbrinck GmbH, art.-no.03- 0060) slides. Using the same exposure and intensity for each sample, immunofluorescent images were acquired with a Keyence BZ-810 fluorescence microscope (Keyence, Tokyo, Japan) using a 20X, 40X and/or 100X/1.45 oil-immersion objective lens. The ImageJ software was used to quantify % of area of positive cells stained by respective antibodies versus total area analyzed for each organ.

Staining protocol:

MBP, Neuron, Astrocytes, DAPI immunostaining:

After deparaffinizing and dehydrating steps using 100 % xylene (isomeric mixture, ACROS ORGANICS), increasing ethanol (VWR Chemicals) dilutions and water, antigen (epitope) retrieval was performed using citrate buffer (45 min at 90 °C). After washing steps (3 x 5 min in PBS), blocking was performed for 60 min at room temperature with 5 % Normal

serum Blocking solution (BioLegend) in 0.3 % Triton X-100 in PBS. Incubation with the primary antibodies was done overnight at 4 °C (MBP, NeuN, GFAP). After washing steps (3 x 5 min in PBS), incubation with the secondary antibodies was done for 45 min at room temperature (1:400 dilution, dylight-488 horse anti rabbit IgG, Vector Lab, Cat.No. DI-1088-1.5; AlexaFluor-647 donkey anti goat IgG, abcam, Cat.No. ab150135; Cy3 horse anti mouse IgG, Vector Lab, Cat.No. CY-2300-1). DAPI BioMount aqueous mounting glue (Bio-Optica, 05-1740) was used as counterstain for nuclei. Negative controls were performed using 1X PBS buffer as primary antibody incubation step and used to set up the background fluorescent exposure threshold of each stained organ.

Statistics:

Statistical analysis and preparation of graphs were done using GraphPad Prism 9.3.1. All experimental results were tested for normal distribution using the Shapiro-Wilk test. Before conducting further statistical analysis, the Brown-Forsythe test was used to test data for homoscedasticity while ordinary one-way ANOVA was used for multiple comparisons (Bonferroni correction). Incidence was compared using the Chi^2 test and p-values were corrected with the Bonferroni method for multiple comparisons. EAE-scores were compared using multiple Mann-Whitney tests with two-stage step-up (Benjamini, Krieger, and Yekutieli), p-values were corrected with the Bonferroni method for multiple comparisons. In addition, two-way ANOVA was used to test for differences in body weight data, p-values were corrected with the Bonferroni method for multiple comparisons. Significance levels are indicated by * $p < 0.05$; ** $p < 0.01$; *** $p < 0.001$; **** $p < 0.0001$.

2.3 Results

In order to obtain a stable and reproducible EAE mouse model to use for the evaluation of drug effects, a study was designed to assess the influence of the MOG_{35-55}-peptide preparation and of two different diets in mice with different age (young *versus* middle-aged) to evaluate disease manifestation and variability of EAE induction. Moreover, the MOG_{35-55}- and PTX concentration used for induction were varied with the aim to investigate the possibility to obtain different EAE severity models.

To this end, at first a study with 36 female C57BL/6 mice was performed (**Table 31**). Due to the known impact of dietary factors like fiber content, antioxidants, sugar, iron and protein levels on MS and EAE disease manifestation[48–50], the purified low fermentative diet AIN 93M was used and compared it with the pro-fermentative diet VRF1, rich in non-digestible fiber and protein. The AIN 93M diet is characterized by a low non-digestible fiber content and overall fewer antioxidants combined with a higher energy density, compared to VRF1. A basic maintenance diet (*V 1534 - 000* SSNIFF®; Control diet) was used to feed the control mice group. To allow adaptation to the respective diets, mice

were pre-fed for 6 weeks with the indicated diets, before disease induction on day 0 (**Figure 9**).

In Study 1, the mice were divided into five treatment groups (**Table 31**) and either fed with the maintenance diet (control group 1, four animals) or with the experimental diets VRF1 (group 2 and 3, eight animals) or AIN 93M (group 4 and 5, eight animals). I additionally wanted to assess the influence of different MOG_{35-55} preparations on EAE induction. To this end, two different preparations of the MOG_{35-55}-peptide were tested: one where homogenization of the peptide in CFA emulsion was achieved via the double-syringe method and one emulsion that was prepared via sonication with an ultra-sonicator to ensure complete homogenization as described in Material and Methods. At day 0, mice were injected with 150 µL of the respective homogenate (300 µg MOG_{35-55} /animal) at the base of the tail, except for the control mice (group 1) which did not receive any injection.

Table 31. Study 1 experimental groups.

Group No.	N	Chow	MOG_{35-55} per animal	PTX per animal	Emulsion preparation
1	4	Control diet	-	-	-
2	8	VRF1	300 µg	240 ng	-son
3	8	VRF1	300 µg	240 ng	+son
4	8	AIN 93M	300 µg	240 ng	-son
5	8	AIN 93M	300 µg	240 ng	+son

Body weight was assessed daily, starting on day 1 (post EAE induction) until the end of the experiment (17 days post induction). Exemptions being day 0, where the weighing was skipped in order to avoid additional stress, which could impact the disease development. Starting from the first manifestation of disease signs (scoring ≥ 0.5), animals were scored daily (**Figure 9**).

As expected, body weight did not differ noticeably between groups during the first half of the study (day 0 to day 9), representing the typical symptom free phase of the EAE-model (**Figure 12b**). However, on day 10, differences became noticeable between groups 2 and 3 (AIN 93M diet) and 4 and 5 (VRF1 diet). AIN 93M-fed mice displayed substantial and continuous loss in body weight reaching an overall weight loss of 13 % (group 4, AIN $93M^{-son}$) and 16 % (group 5, AIN $93M^{+son}$) at study termination (day 17). In contrast, both

groups fed on VRF1 diet (2 and 3, VRF1^{-son} and VRF1^{+son}) reached a loss in body weight of only 3 %.

As expected, the disease scores obtained for the different groups matched the differences observed in body weight. Average symptom scores, calculated as AUC, differed significantly between the diets ($p < 0.01$ for VRF1^{+son} versus AIN 93M^{+son}, $p < 0.05$ for VRF1^{-son} versus AIN 93M^{-son}), but not between the different emulsion preparation methods. On day 17, AIN 93M^{+son} fed mice reached a disease score of 4.6 ± 0.6, representing severe signs, compared to a mild score of 1.9 ± 1.3 and 1.8 ± 1.4, obtained for the VRF1-fed animals. Due to the aggressiveness of the model, the study was terminated ahead of schedule (on day 17) (**Figures 9** and **12e**, **Table 32**). At day 15 of the first study, animals with scores ≥ 4.0 were euthanized (**Figure 12**): 3 in the AIN 93M^{-son} group (62,5 % survival) and 6 in the AIN 93M^{+son} group (25 % survival). It was observed that survival rates differed significantly between AIN 93M^{+son} and VRF1-treatment groups ($p = 0.0027$).

The incidence of EAE manifestation was analyzed dependent on the disease scores (**Figure 12h**). 100 % incidence was shown only by the mice on the AIN 93M diet, independent of the MOG_{35-55} peptide preparation method (**Tables 32** and **34, Figure 12h, i** and **j**). In contrast, disease incidence was lower in both the VRF1^{-son} and VRF1^{+son} groups: In the former, only 62.5 % of animals displayed disease signs by the end of the study, and 75 % in the latter. Additionally, a delay of the first occurrence of signs was observed: occurrence in VRF1 groups was observed two days later compared to the AIN 93M^{+son} group (day 11 versus day 9) (**Tables 32** and **34, Figure 12h**).

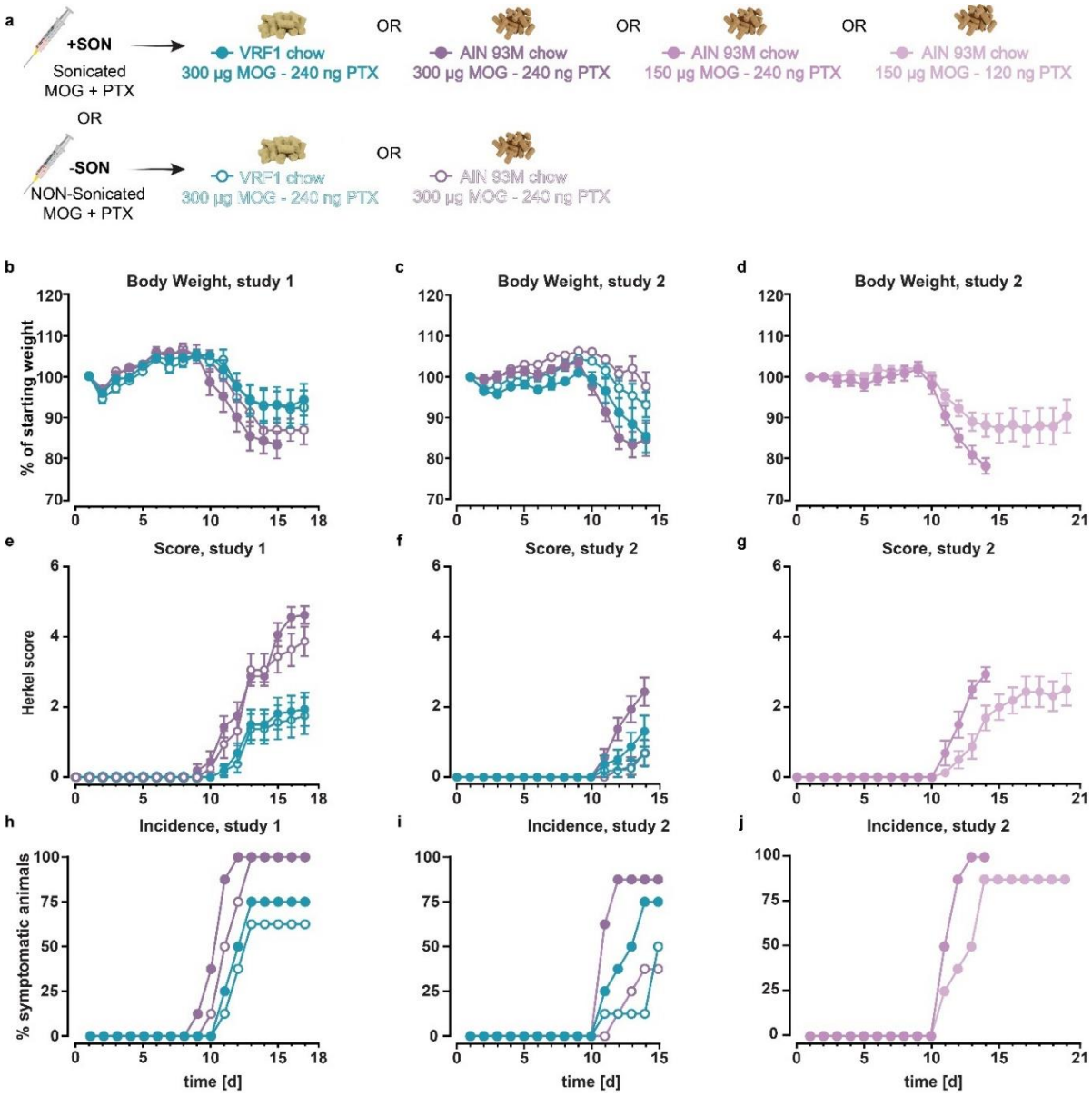

Figure 12. Comparison of different induction methods of the EAE model: i) preparation of MOG_{35-55}-peptide emulsion by +son versus -son, a low-fiber, low-antioxidant diet versus a pro-fermentative diet and high versus low doses of MOG_{35-55}-peptide and PTX; ii) also the pre-feeding time was compared: six weeks in Study 1 versus. 6 months in Study 2. Body weight (**b-d**) and symptom scores (**e-g**) were assessed daily and total incidence of animals developing EAE was recorded (**h-j**). Data are displayed as mean ± SD of the mean, n = 8. AIN 93M results displayed in purple and VRF1 results displayed in cyan.

a) Summary of the tested variables.

b-d) Average body weight of studies 1 and 2 of mice post-immunization with MOG_{35-55}-peptide over time. When comparing the last day of the study, animals fed with the AIN 93M diet experienced a significant loss of BW versus animal fed the VRF1 diet. (n = 8).

e-g) Average symptom score of studies 1 and 2 of mice post-immunization with MOG_{35-55}-peptide over time n = 8. Signs developed earlier and more severely in the groups fed with the AIN 93M diet. Sonication of the MOG_{35-55}-peptide emulsion further increased severity in the AIN 93M groups. (**h-j**) Incidence per group. Animals were counted as "symptomatic" when their EAE score reached values ≥ 0.5. Data are displayed as percentiles (n = 8). This Figure is adapted from Martorelli *et.al*. 2024, under revision.

Table 32. Disease incidence and EAE score of Study 1 at the end of the study (day 17 post-immunization, n = 8). Animals were counted as "symptomatic" when their EAE score reached values > 0. Summary of the EAE score: VRF1 diet versus AIN 93M diet.

	VRF1 diet incidence	AIN 93M diet incidence	VRF1 diet EAE score	AIN 93M diet EAE score
MOG 300, PTX 240 double syringe	62.5 %	100 %	1.8 ± 1.4	3.9 ± 1.1
MOG 300, PTX 240 sonication	75 %	100 %	1.9 ± 1.3	4.6 ± 0.6

In order to evaluate the robustness of the detected effects caused by both, diet- and emulsion preparation, and to test the effect of long-term dieting and ageing (trained immune system)[46] , the *in vivo* study was repeated with adaptations. In the second study, animals were pre-fed with the respective diets for 24 weeks (**Figure 11**). Additional groups were included in order to firstly evaluate the optimal dose of MOG_{35-55} peptide and secondly to assess the optimal dose of the intraperitoneal booster injections of PTX. In the second study, a total of 68 C57BL/6 mice were included (**Figure 11** and **Table 33**). Similar to study 1, mice were either fed with Control diet (group 1; 4 animals) or with experimental diets VRF1 (group 2, 4, and 5; 8 animals) or AIN 93M (group 3, 6-9; 8 animals). EAE was induced by immunization with either 300 or 150 µg MOG_{35-55} per mouse as indicated in **Table 33**. Similar to study 1, MOG_{35-55} peptide emulsion was prepared either by non-sonicated double-syringe or ultrasound-sonication method. Intraperitoneal booster injections with PTX were performed twice at a dose of 240 or 120 ng/mL, first on study day 0, directly after MOG_{35-55} induction and then again on study day 2 (**Figure 9**). The body weight of the animals was checked daily, starting on day 1. Exemptions being day 0 to avoid additional stress for the mice during the induction period.

Table 33. Study 2 experimental group design.

Group No.	N	Chow	MOG_{35-55} Concentration	PTX Concentration	Emulsion preparation
1	4	Control diet	-	-	-
2	8	VRF1	-	-	-
3	8	AIN 93M	-	-	-
4	8	VRF1	300 µg	240 ng	-son
5	8	VRF1	300 µg	240 ng	+son
6	8	AIN 93M	300 µg	240 ng	-son
7	8	AIN 93M	300 µg	240 ng	+son
8	8	AIN 93M	150 µg	240 ng	+son
9	8	AIN 93M	150 µg	120 ng	+son

As observed in study 1 (**Figure 12b**, **e**, **h**), body weight did not diverge noticeably between groups during the first nine days (see **Figure 12c**, **d**). At study day 10, differences became noticeable. Interestingly, animals treated with non-sonicated MOG_{35-55} emulsion displayed the lowest impact on body weight, irrespective of diet, with a final body weight loss of 3 % and 5 % in AIN $93M^{-son}$ and $VRF1^{-son}$ animals, respectively. In contrast, $VRF1^{+son}$ and AIN $93M^{+son}$ animals suffered a weight loss of 13 % to 15 %, respectively at study termination (**Figure 12c**). Within the groups treated with sonicated MOG_{35-55} emulsion, the higher MOG_{35-55} dose (300 µg versus 150 µg) resulted in stronger overall body weight loss, as expected (15 % versus. 5 %). The same was observed for PTX - the higher dose of PTX (240 ng) was associated with a more severe body weight loss (**Figure 12d**). Disease scoring reflected the observations in body weight. AIN $93M^{+son}$ animals displayed the highest disease score (**Table 34, Figure 12**). Interestingly, despite the profound body weight loss, $VRF1^{+son}$ animals only reached a disease score of 1.3 ± 1.2, which is similar to the score achieved by this diet/treatment combination in the first study (study 1 $VRF1^{+son}$ score: 1.8 ± 1.4). Animals treated with non-sonicated, inverted MOG_{35-55} emulsion displayed the lowest score. Again, the higher dose of PTX (240 ng/animal) and MOG_{35-55} emulsion (300 µg/animal) resulted in increased disease scores reflecting a more severe phenotype (see **Figure 12g** and **Table 34**).

Table 34. Disease incidence of Study 2 at the end of the study (day 14 post-immunization, n = 8). Animals were counted as "symptomatic" when their EAE score reached values > 0. Summary of the EAE score: VRF1 diet versus AIN 93M diet. n.d.: not done.

	VRF1 diet incidence	AIN 93M diet incidence	VRF1 diet EAE score	AIN 93M diet EAE score
MOG 300, PTX 240 double syringe	50 %	38 %	0.7 ± 1.0	0.7 ± 0.9
MOG 300, PTX 240 sonication	75 %	85 %	1.3 ± 1.2	2.4 ± 1.1
MOG 150, PTX 240 sonication	n.d.	100 %	-	2.9 ± 0.5
MOG 150, PTX 120 sonication	n.d.	85 %	-	2.5 ± 1.2

These results indicate that variability in disease manifestation is caused by a) diet, with AIN 93M diet-fed animals displaying a less variable phenotype; and b) the MOG_{35-55} peptide emulsion preparation: the data at hand imply that +son emulsion reduces variability of the EAE-model introduced by the MOG_{35-55} peptide preparation.

Disease incidence in study 2 (**Figure 12i** and **j**) was reproducible despite variation in overall disease (body weight loss and EAE scores) displayed by similar treatment groups of the two different studies: independent from MOG_{35-55} peptide preparation method used, mice held on AIN 93M diet displayed a high incidence (85 or 100 %) in both, study 1 and study 2 (**Tables 32** and **34, Figure 12h, i** and **j**). Also, AIN 93M diet-fed but half dose induction (150 ng/mouse MOG_{35-55} peptide, sonicated and 120 µg/mouse PTX injection) resulted in an incidence of 85 %. On the other hand, disease incidence was lower in both VRF1-fed groups: the incidence resembled what was seen in study 1, with lower incidence for $VRF1^{-son}$ mice (62.5 %) and a slightly higher one for $VRF1^{+son}$ animals (75 %) (**Table 34** and **Figure 12h, i** and **j**).

In order to evaluate effects of MOG_{35-55}-peptide preparation and diet on overall survival, data was evaluated combining similar groups of both studies (n = 16 mice per group). In the short-term study (6 weeks pre-fed animals), no mice were found dead in the cage or had to be euthanized due to the development of severe signs over the end of the study. This was observed for both tested MOG_{35-55}-peptide preparation methods. On the other side, for the AIN 93-fed mice, three animals were euthanized until study day 17 in the AIN $93M^{-son}$ group (62,5 % survival) and six animals in the AIN $93M^{+son}$ group due to severe signs reported by the operator (25 % survival). Overall, survival rates differed statistically significantly between both VRF1-treatment groups and AIN $93M^{+son}$ ($p = 0.0027$). Also, in the long-term study (24 weeks pre-fed animals) no mice were euthanized or found dead in cage due to development of severe signs.

MOG_{35-55}-peptide preparation and diet play different roles in the regulation of immune cell marker and myelin related genes in brain and spinal cord

With the aim to evaluate the role of the MOG_{35-55}- peptide preparation and tested diets on the EAE induction in more detail, the effects on demyelination processes and the grade of inflammation in brain and spinal cord were assessed by gene expression analysis. To this end, the expression levels of relevant inflammatory cytokines (*IL-10*, *GM-CSF*), immune cell markers (*FoxP3*, *GFAP*, *TBX21*, *H2-Ab1*) and related markers for myelination processes (*MOG*, *MBP*, *OLIG2*, *CSPG4*) were determined in brain and spinal cord samples taken from euthanized mice of study 2 at day 15 by RT-qPCR (**Figures 13-16**; **18-20**).

The results of this analysis revealed that *Mbp*, in brain samples of $VRF1^{+son}$ and in both AIN 93M fed mice groups, was significantly downregulated (**Figure 13c**). While *Olig2* and *Mog* expression in the brain did not significantly differ between the groups (**Figure 13d**, **e**), *Cspg4* was also significantly downregulated in brain samples of $VRF1^{-son}$ and $AIN\ 93M^{-son}$ mice (**Figure 13b**). In spinal cord of -son MOG preparation mice, mRNA levels of myelin related genes were diminished (**Figure 14b–e**). Markers which are known to be associated with the activation of astrocytes (*Gfap*)[51] and microglia (*H2-Ab1)*[52] were correlated to EAE scores and incidence. Both, *Gfap* and *H2-Ab1*, were primarily upregulated in mice that were induced with sonicated MOG_{35-55} preparation with an even stronger induction in AIN 93M fed mice (**Figure 13f, g** and **Figure 13f, g**). As an indirect readout for the disruption of the blood brain barrier, T-cell markers *Tbx21* and *Foxp3* were measured. In mice that received the sonicated MOG preparation, regulatory effects of these markers could be observed (**Figure 13h**, **i** and **Figure 14h**, **i)**. In order to evaluate general inflammation processes in the brain and spinal cord, mRNA levels of the cytokines *Gm-csf* and *IL-10* were analyzed. *Gm-csf* expression levels were significantly upregulated in spinal cord samples of mice that were induced with sonicated MOG_{35-55} preparation (**Figure 14j**), while in brain samples, only VRF1-fed mice showed significant upregulation of *Gm-csf* in combination with the sonicated MOG_{35-55} preparation (**Figure 14j**). Due to low expression levels of *IL-10* in the spinal cord, mRNA levels were only quantified in brain samples, where a significant upregulation could be observed in mice with sonicated MOG_{35-55} preparation.

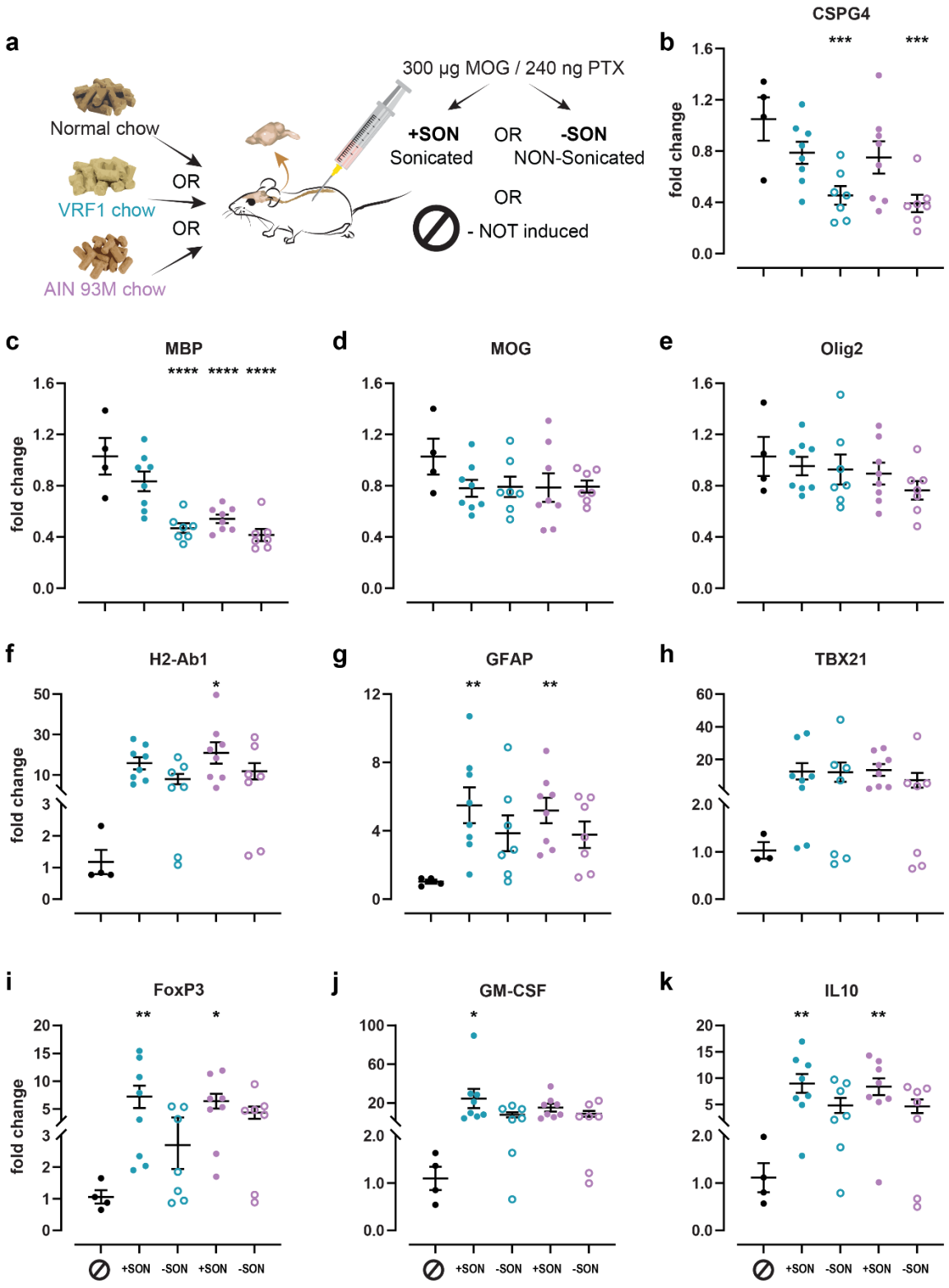

Figure 13. qPCR on brains of EAE induced mice with different MOG emulsion preparation. **a**) Effect of MOG_{35-55} preparation and diet (VRF1 versus AIN 93M) of induced female C57BL/6 mice (300 µg MOG_{35-55}, 240 ng PTX) normalized to healthy control animals (Control diet fed) in the brain. **b-e**) Quantitative analysis of myelin (*MBP* and *MOG*) and oligodendrocytes markers (*CSPG4*, *Olig2*)

showing a more relevant diet effect in comparison to the MOG_{35-55} preparation for the *CSPG4* marker (oligodendrocytes precursor) and *MBP* (Myelin Base Protein). **f-k**) Quantitative analysis of the immune cell profile showing in the brain in the MOG_{35-55} sonicated emulsion groups an upregulation and higher infiltration of T-cells different subpopulations. * $p < 0.05$; ** $p \leq 0.01$; *** $p \leq 0.001$; **** $p \leq 0.0001$. Data are displayed as mean ± SD of the mean, n = 4 to 8. AIN 93M results displayed in purple and VRF1 results displayed in cyan. This Figure is adapted from Martorelli *et.al*. 2024, under revision.

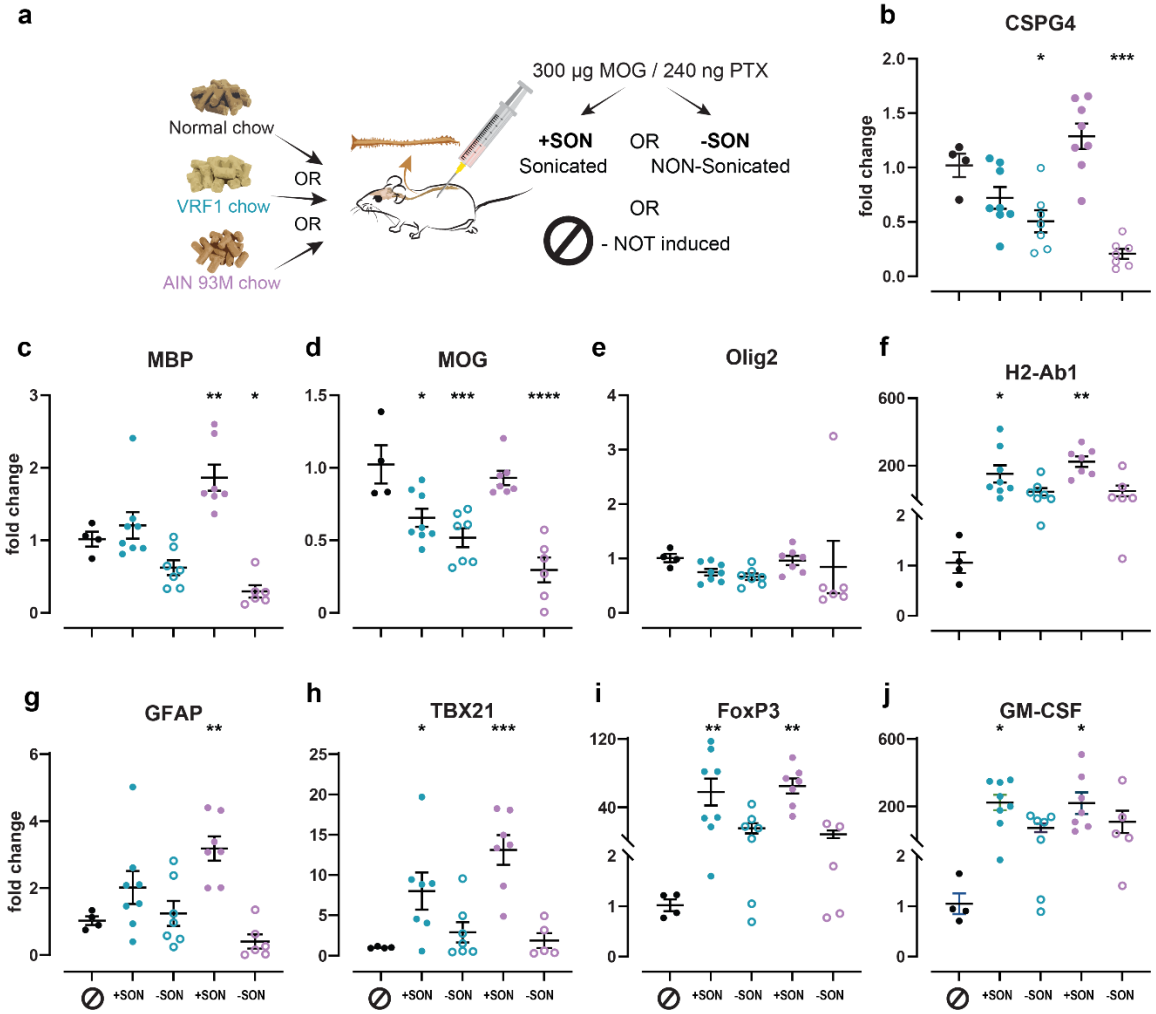

Figure 14. qPCR on spinal cords of EAE induced mice with different MOG emulsion preparation. **a**) Effect of MOG_{35-55} preparation and diet (VRF1 versus AIN 93M) on induced female C57BL/6 mice (300 µg MOG_{35-55}, 240 ng PTX) normalized to healthy control animals (Control diet fed) in the spinal cord. **b-e**) Quantitative analysis of myelin (*MBP* and *MOG*) and oligodendrocytes markers (*CSPG4*, *Olig2*) showing a more relevant diet effect in comparison to the MOG_{35-55} preparation for the *CSPG4* marker (oligodendrocytes precursor) and *MBP* (Myelin Base Protein). **f-j**) Quantitative analysis of the immune cell profile showing in the spinal cord in the MOG_{35-55} sonicated emulsion groups upregulation and higher infiltration of T-cells different subpopulation. * $p < 0.05$; ** $p \leq 0.01$; *** $p \leq 0.001$; **** $p \leq 0.0001$. Data are displayed as mean ± SD of the mean, n = 4 to 8. AIN

93M results displayed in purple and VRF1 results displayed in cyan. This Figure is adapted from Martorelli *et.al*. 2024, under revision.

The PTX dose highly affect the severity of the EAE model

Different PTX and MOG_{35-55} doses were tested on +son emulsion induced mice in Study 2 (long-term). It was observed that the severity of signs was dependent on the PTX dose, but remained unaffected by lowering the amount of MOG_{35-55}-peptide from 300 to 150 µg used for induction (**Figure 15** and **16**). Results also showed that a higher dose of PTX (240 ng) is associated with the severity of the EAE signs in terms of: **a**) body weight loss, **b**) EAE scoring. At day 13, PTX higher dose (240 ng) induced animals showed an incidence of 100 % (see **Figure 12j**), a body weight loss of 20 % (**Figure 12d**) and animals had an EAE score of 2.9 ± 0.5 on average (mean ± SD, **Figure 12g** and **Table 34**).

This effect was not directly reflected by the analysis of myelin related genes. *Cspg4* was significantly downregulated in brains of 240 ng PTX / 150 µg MOG_{35-55} group and 120 ng PTX / 150 µg MOG_{35-55} induced mice (**Figure 15b**). In all induced mice *Mbp* was downregulated (**Figure 15c**), while the downregulation of *Mog* expression could only be observed in the 150 µg MOG_{35-55} / 240 ng PTX group (**Figure 15d**). For the *Mog* target, diminished mRNA levels could only be detected in spinal cord samples of the 240 ng PTX / 150 µg MOG_{35-55} group (**Figure 16b-e**). Activation markers for microglia (*H2-ab1*) and astrocytes (*Gfap*), T-cell markers (*Foxp3 and Tbx21*) and the cytokines (*Gm-csf and IL-10*) were primarily upregulated in brain samples and spinal cords of mice that received the higher PTX dose (240 ng, 150 µg MOG_{35-55}) (**Figure 15f-k**, **Figure 16f-j**), while the low PTX dose (120 ng) was not sufficient to induce T-cell (*Tbx21*) infiltration through the BBB. Additionally, the low dose PTX (120 ng) animals were terminated at day 21 versus the high dose PTX (240 ng) animals terminated at day 15. These difference in time could have affect the gene expression pattern. It has been already shown in literature that in this murine model the peak of disease severity occurred between days 14-16.[53] These findings indicate that the PTX dose increases the severity of signs in a dose-dependent manner. The severity of the EAE model can be explained by different processes, in particular the disruption of the BBB, astrocyte and microglia activation and T-cell infiltration.

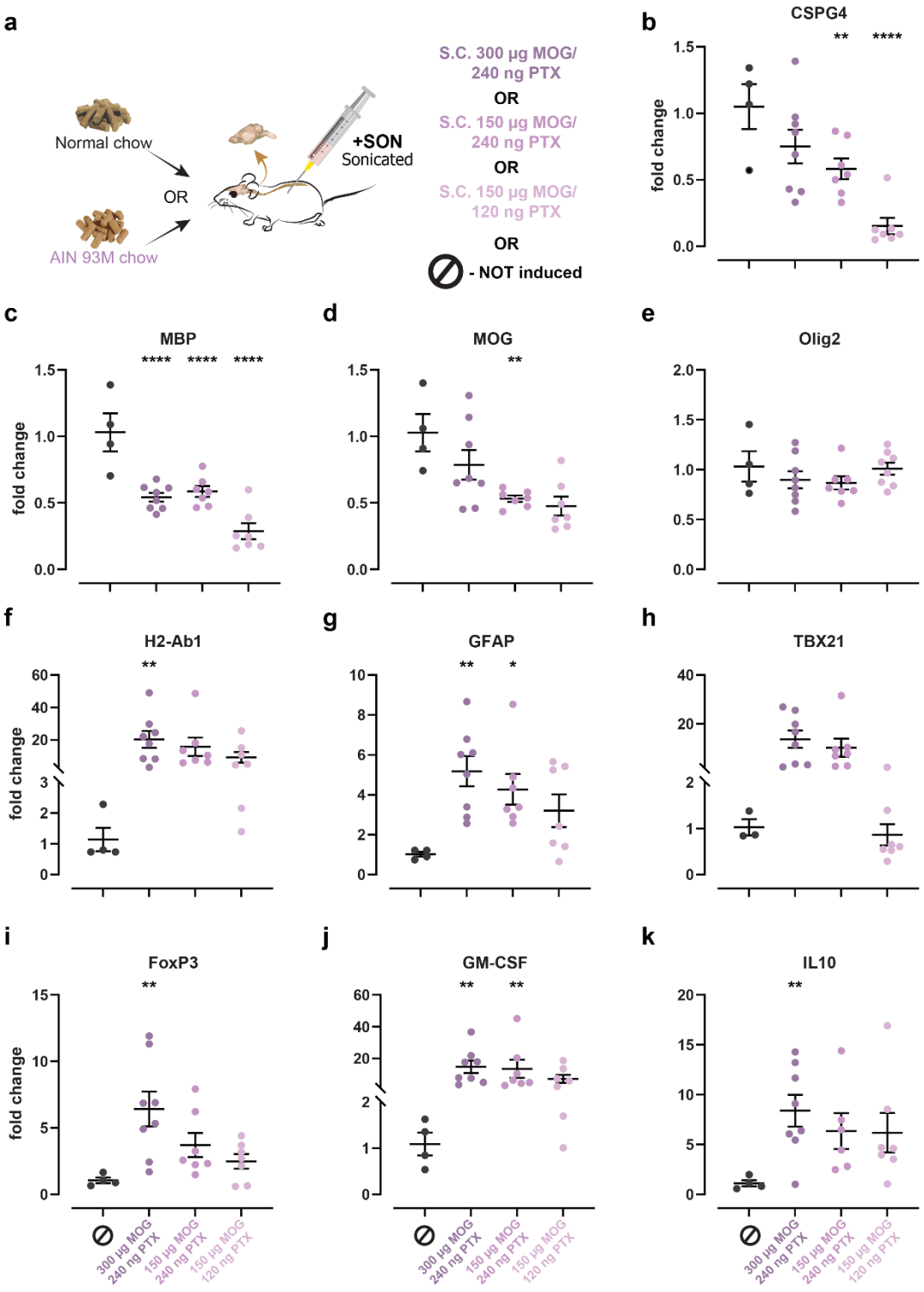

Figure 15. qPCR on the brains of EAE induced mice with different MOG doses. (**a**) Effect of PTX dose and MOG_{35-55} in the brain of induced female C57BL/6 mice (300 µg MOG_{35-55}, 240 ng PTX, 150 µg MOG_{35-55}, 240 ng PTX, and 150 µg MOG_{35-55}, 120 ng PTX) compared to healthy animals (Control diet fed). (**b-e**) Quantitative analysis of oligodendrocytes markers (*Olig2*, *CSPG4*) and myelin (*MOG* and *MBP*) showing a more relevant PTX effect with respect to the MOG_{35-55} one for

the *MBP* and *CSPG4* marker (oligodendrocytes precursor). (**f-k**) Brain quantitative analysis of the immune cell profile showing higher infiltration of T-cells and upregulation in different subpopulations with the highest PTX and MOG_{35-55} dose. * $p < 0.05$; ** $p \leq 0.01$; *** $p \leq 0.001$; **** $p \leq 0.0001$. Data are displayed as mean ± SD of the mean, n = 4 to 8. This Figure is adapted from Martorelli *et.al*. 2024, under revision.

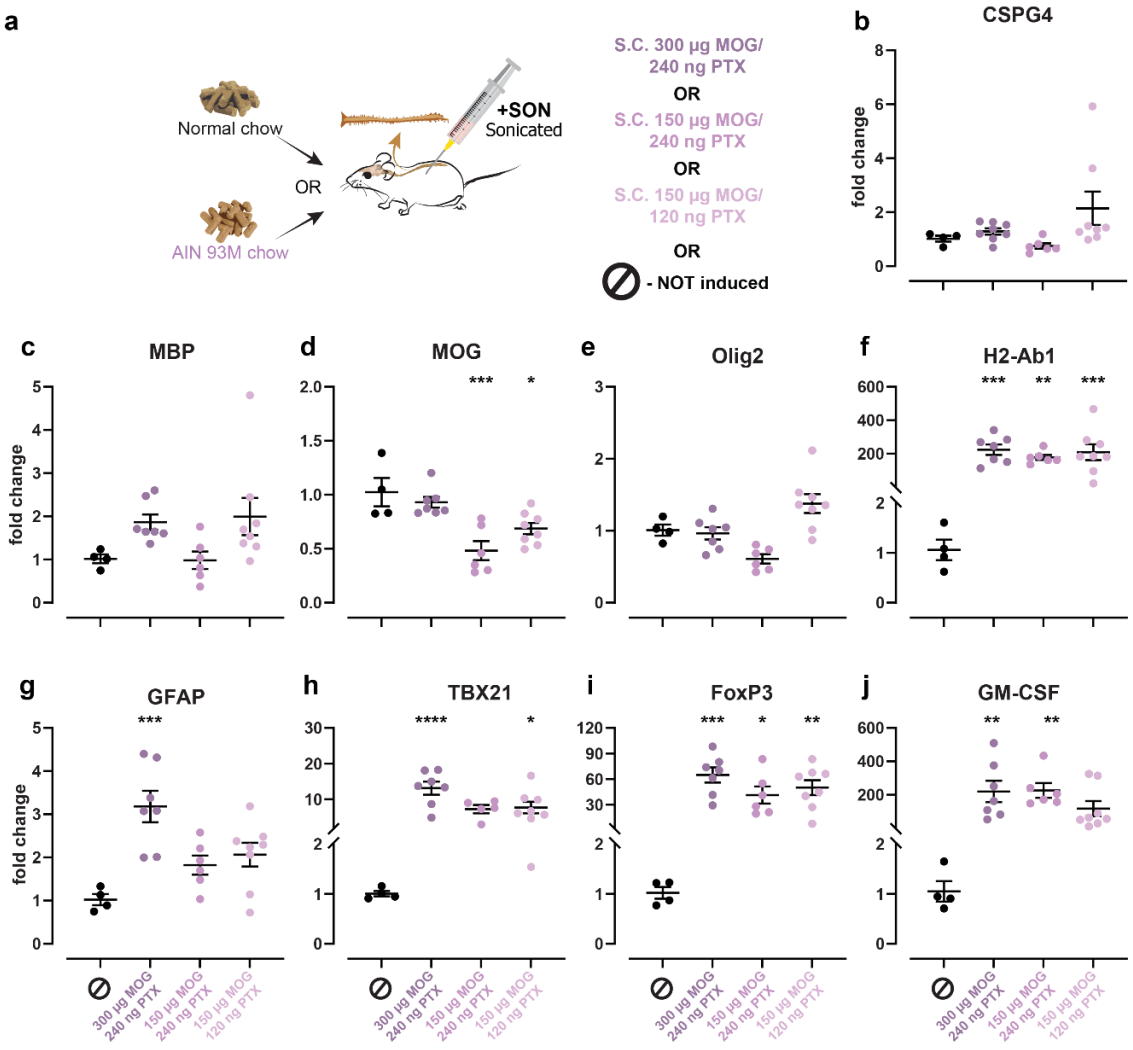

Figure 16. qPCR on the spinal cords of EAE induced mice with different MOG doses. (**a**) Effect of PTX dose and MOG_{35-55} in the spinal cord of induced female C57BL/6 mice (300 µg MOG_{35-55}, 240 ng PTX, 150 µg MOG_{35-55}, 240 ng PTX, and 150 µg MOG_{35-55}, 120 ng PTX) compared to healthy animals (Control diet fed). (**b-e**) Quantitative analysis of oligodendrocytes markers (*Olig2*, *CSPG4*) and myelin (*MOG* and *MBP*) showing a more relevant PTX effect with respect to the MOG_{35-55} one for the *MBP* and *CSPG4* marker (oligodendrocytes precursor). (**f-k**) Spinal cord quantitative analysis of the immune cell profile showing higher infiltration of T-cells and upregulation in different subpopulations with the highest PTX and MOG_{35-55} dose. * $p < 0.05$; ** $p \leq 0.01$; *** $p \leq 0.001$; **** $p \leq 0.0001$. Data are displayed as mean ± SD of the mean, n = 4 to 8. This Figure is adapted from Martorelli *et.al*. 2024, under revision.

Severe demyelination and inflammation in the spinal cord and brain of MOG_{35-55}-peptide EAE induced mice is highly correlated to AIN 93M low fiber diet

In order to evaluate inflammation and demyelination processes and to complement the qPCR results obtained for study 2, histological analysis was performed in the brain and spinal cord of AIN $93M^{+son}$ and $VRF1^{+son}$ animals (these groups were specifically selected to check for the suspected diet effect, while the emulsion preparation method resulted mostly in increased variability). Due to both the robust incidence and expression of target genes, this analysis was done only for the two groups induced with 300 µg MOG_{35-55}-peptide and 240 ng PTX, both +son emulsions. At termination day (15 days after EAE-induction), mice were sacrificed and brains and spinal cords were harvested for myelin basic protein (MBP) and activated astrocytes (GFAP) analysis. KEYENCE inverted fluorescence microscope BX-Z810 was used to digitalize stained sections. 20X and 100X magnification images (**Figure 17c** and **b**), respectively for spinal cord and brain, were used for all quantitative analysis. Astrocyte-positive fraction stained with a GFAP antibody (yellow channel) and myelin-positive cell fraction stained by an MBP antibody (green channel) were quantified while as contra-staining was used a neuronal marker (Neun, red channel). Folded organ sections were excluded from analysis because they led to false positive results. On both AIN 93M diet-fed and VFR1 diet-fed induced mice, as expected, the percentage of the MBP+ area showed statistically significant reduction ($p \leq 0.0001$ and $p \leq 0.05$, respectively) but interestingly, not on spinal cord, even though the analysis showed an area reduction in the spinal cord of AIN $93M^{+son}$ mice of ~30 %. On the other hand, in both brain and spinal cord, the percentage of GFAP+ area showed a statistically significant increase only in AIN 93M diet induced mice ($p \leq 0.01$).

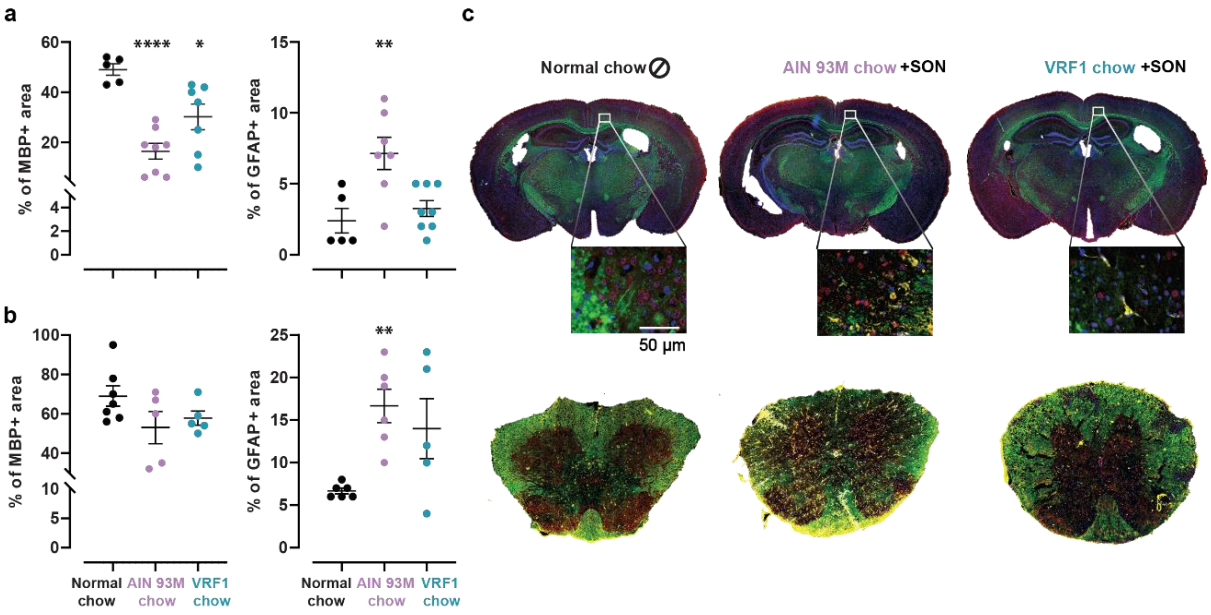

Figure 17. Histopathological examination of brains and spinal cords of female C57BL/6 mice (300 µg MOG_{35-55}, 240 ng PTX, AIN 93M^{+son} and VRF1^{+son} groups, Study 2). **a**) Percentage of MBP and GFAP positive area on coronal brain sections of AIN 93M^{+son} and VRF1^{+son} induced mice normalized versus Control diet not-induced mice; **b**) Percentage of MBP and GFAP positive area on spinal cord sections of AIN 93M^{+son} and VRF1^{+son} induced mice normalized versus Control diet not-induced mice; **c**) As expected, MOG_{35-55} immunization resulted in demyelination and inflammation in brain and spinal cord. Control diet fed not-induced mice showed healthy condition in both organs, while VRF1^{+son} fed mice displayed mild demyelination (MBP – green) and moderate inflammation (astrocytes – yellow) in brain and spinal cord versus a severe inflammation and demyelination compared to AIN 93M fed mice. * $p \leq 0.05$; ** $p \leq 0.01$; *** $p \leq 0.001$; **** $p \leq 0.0001$. Data are displayed as mean ± SD of the mean, n = 4 to 8. AIN 93M results displayed in purple and VRF1 results displayed in cyan. This Figure is adapted from Martorelli *et.al*. 2024, under revision.

Asymptomatic satellite animals' brain samples shown downregulation of myelin-related genes

In Study 2, asymptomatic satellite animals were sacrificed at day 7, in order to investigate parameters like diet or preparation of emulsion by the expression kinetics of the selected targets and molecular mechanisms involved in the onset of the disease. Interestingly, myelin related genes were primarily downregulated in brain samples of satellites, followed by an increase to basal expression levels (*Cspg4*) (**Figure 18b**), respectively from high to moderate significance (*Mbp* in AIN 93M fed mice) (**Figure 18c**), until the peak of the disease. This effect could not be observed in spinal cord samples. The mRNA levels of *H2-Ab1*, *Gfap*, *Tbx21*, *Foxp3*, *Gm-csf* and *IL-10* remained unregulated in both spinal cord and brain samples of the satellite animals (**Figure 18** and **19**).

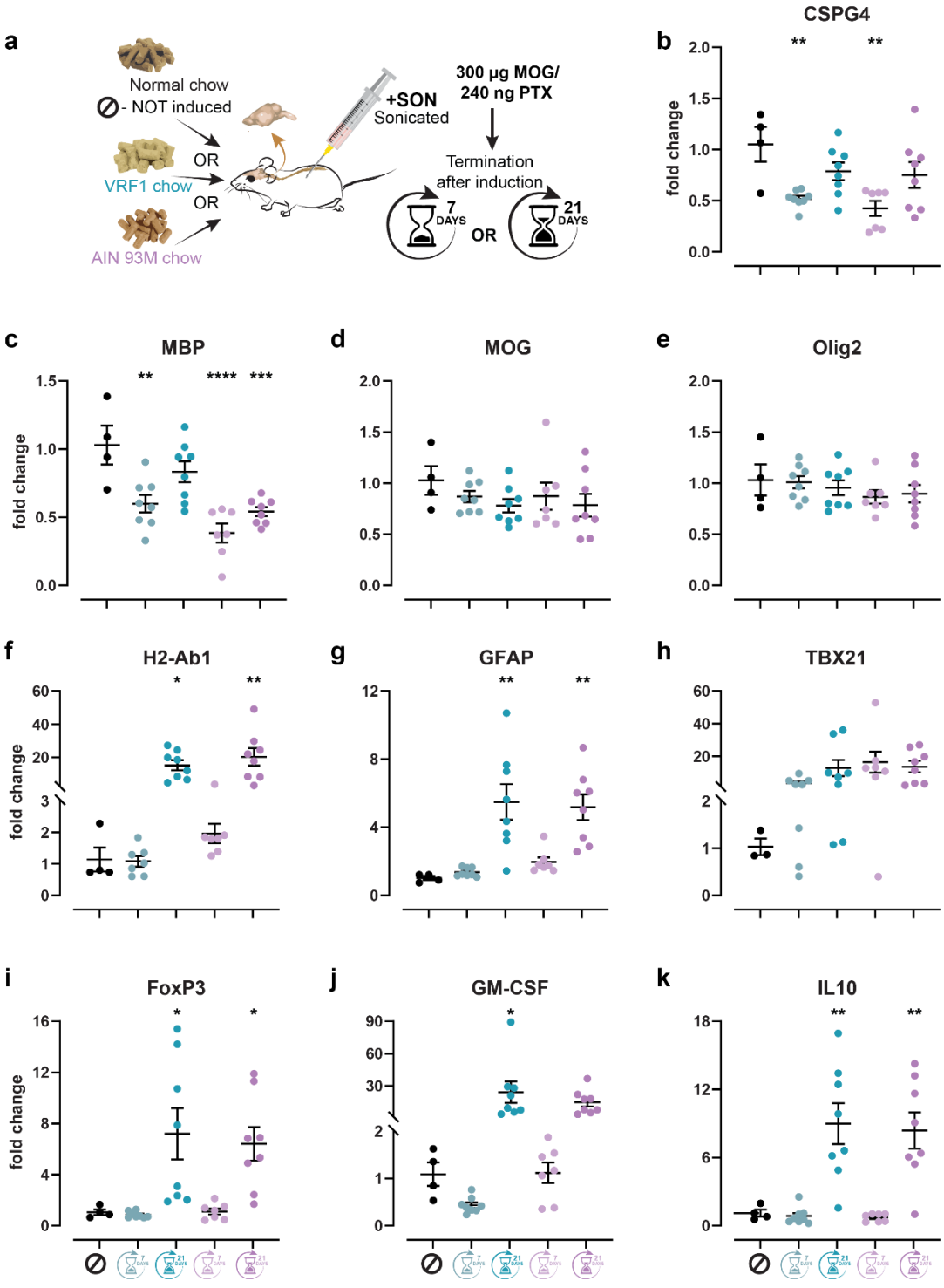

Figure 18. qPCR on satellite brains of EAE induced mice. **a**) Satellites animals (terminated 7 days after induction) compared to +son induced C57BL/6 mice 300 µg MOG_{35-55}, 240 ng PTX (terminated 15 days post induction) and NOT-induced healthy animals (Control diet fed) on expression levels in the brain. **b-e**) Quantitative analysis of oligodendrocytes markers (*CSPG4*, *Olig2*) and myelin (*MBP* and *MOG*) showing strong downregulation of the *CSPG4* marker (oligodendrocytes precursor) and *MBP* in the initial asymptomatic phase post MOG_{35-55} and PTX

induction in both, AIN 93M and VRF1 fed animals. **f-k**) Quantitative analysis of the immune cell profile showing upregulation and higher infiltration of T-cells different subpopulation only after 7 days post MOG_{35-55} and PTX induction. * $p < 0.05$; ** $p \leq 0.01$; *** $p \leq 0.001$; **** $p \leq 0.0001$. Data are displayed as mean ± SD of the mean, n = 4 to 8. AIN 93M results displayed in purple and VRF1 results displayed in cyan. This Figure is adapted from Martorelli *et.al*. 2024, under revision.

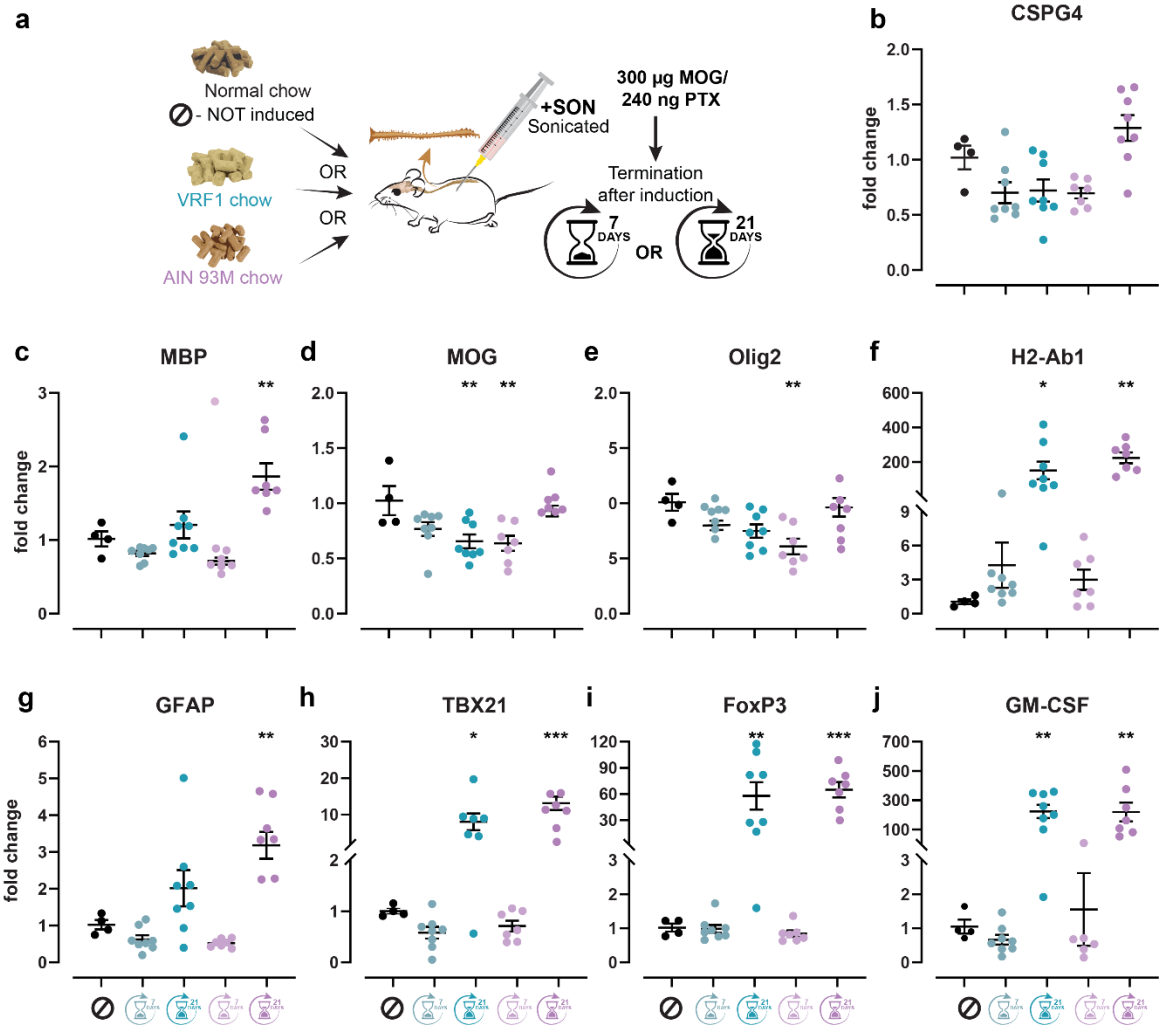

Figure 19. qPCR on satellite spinal cords of EAE induced mice **a**) Satellites animals (terminated 7 days after induction) compared to +son induced C57BL/6 mice 300 µg MOG_{35-55}, 240 ng PTX (terminated 15 days post induction) and NOT-induced healthy animals (Control diet fed) on expression levels in the spinal cord. **b-e**) Quantitative analysis of oligodendrocytes markers (*CSPG4*, *Olig2*) and myelin (*MBP* and *MOG*) showing recovery of *CSPG4* marker (oligodendrocytes precursor) and *MBP* at day 15 post MOG_{35-55} and PTX induction in both, VRF1 and AIN 93M fed animals. **f-j**) Quantitative analysis of the immune cell profile showing upregulation and higher infiltration of T-cells different subpopulation. * $p < 0.05$; ** $p \leq 0.01$; *** $p \leq 0.001$; **** $p \leq 0.0001$. Data are displayed as mean ± SD of the mean, n = 4 to 8. AIN 93M results displayed in purple and VRF1 results displayed in cyan. This Figure is adapted from Martorelli *et.al*. 2024, under revision.

Dietary effect on the expression level of astrocyte, microglia and myelin related genes markers in the brain of naïve control mice

To shed more light on the diet-effect, qPCR analysis in brain and spinal cord samples of naïve AIN 93M- and VRF1 fed- mice was performed. Surprisingly, gene expression analysis of naïve, not-induced mice revealed a regulatory effect of both diets on astrocyte, and microglia markers, as well as on myelin related genes in the brain, but not on inflammation and immune cell markers. *Cspg4, Mbp* and *Gfap* mRNA was significantly downregulated in both AIN 93M and VRF1 fed mice, this effect can be seen to a greater extent in AIN 93M mice (**Figure 20b**, **c**). These observations are comparable to EAE induced mice, where low fiber fed mice displayed higher incidence and EAE scoring (more severe disease). However, *Mog* expression was only decreased in VRF1 fed mice (**Figure 13d**). Moreover, reduced *Gfap* and *H2-Ab1* expression levels were detected in brains of AIN 93M and VRF1 fed mice (**Figure 20f**, **g**). On the other hand, in spinal cord samples the analysed targets remained unregulated (**Figure 21**); thus, diet effects on gene regulation could only be observed in the brain, but not in the spinal cord of naïve, diet-pre-fed mice.

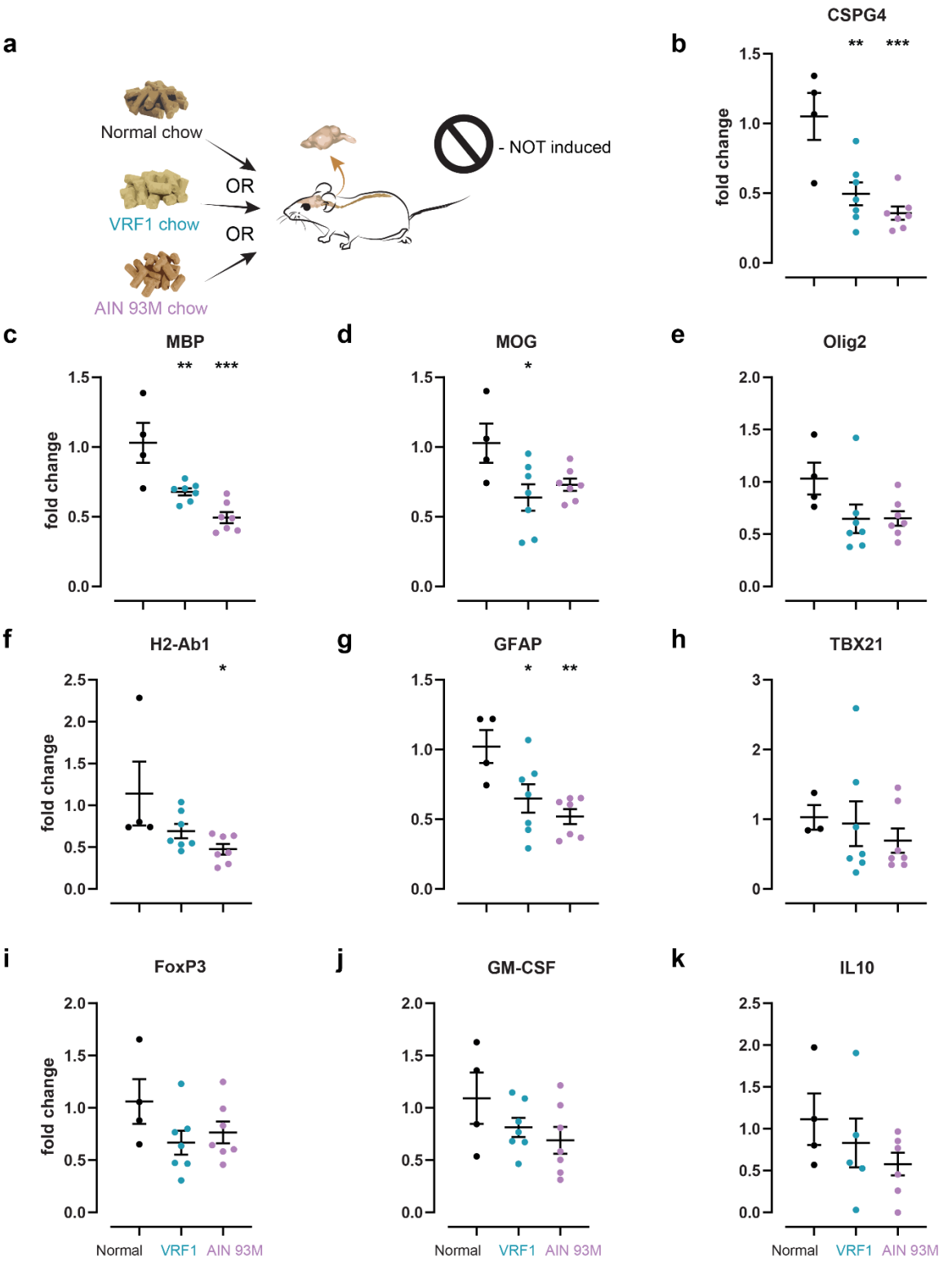

Figure 20. qPCR on brains of un-induced mice pre-fed with different diets. **a**) Effect of diet (VRF1 versus AIN 93M versus Control diet) on not-induced, naïve female C57BL/6 mice in the brain. **b-e**) Quantitative analysis of oligodendrocytes markers (*CSPG4*, *Olig2*) and myelin (*MBP* and *MOG*) showing downregulation in mice fed with AIN 93M and VRF1 diet in comparison to Control diet.

f-k) Quantitative analysis of the immune cell profile showing no significant regulation of T-cells and GM-CSF, in contrast to astrocytes (*GFAP*) in brain of mice fed with AIN 93M diet. * $p < 0.05$; ** $p \leq 0.01$; *** $p \leq 0.001$; **** $p \leq 0.0001$. Data are displayed as mean ± SD of the mean, n = 4 to 8. AIN 93M results displayed in purple and VRF1 results displayed in cyan. This Figure is adapted from Martorelli *et.al*. 2024, under revision.

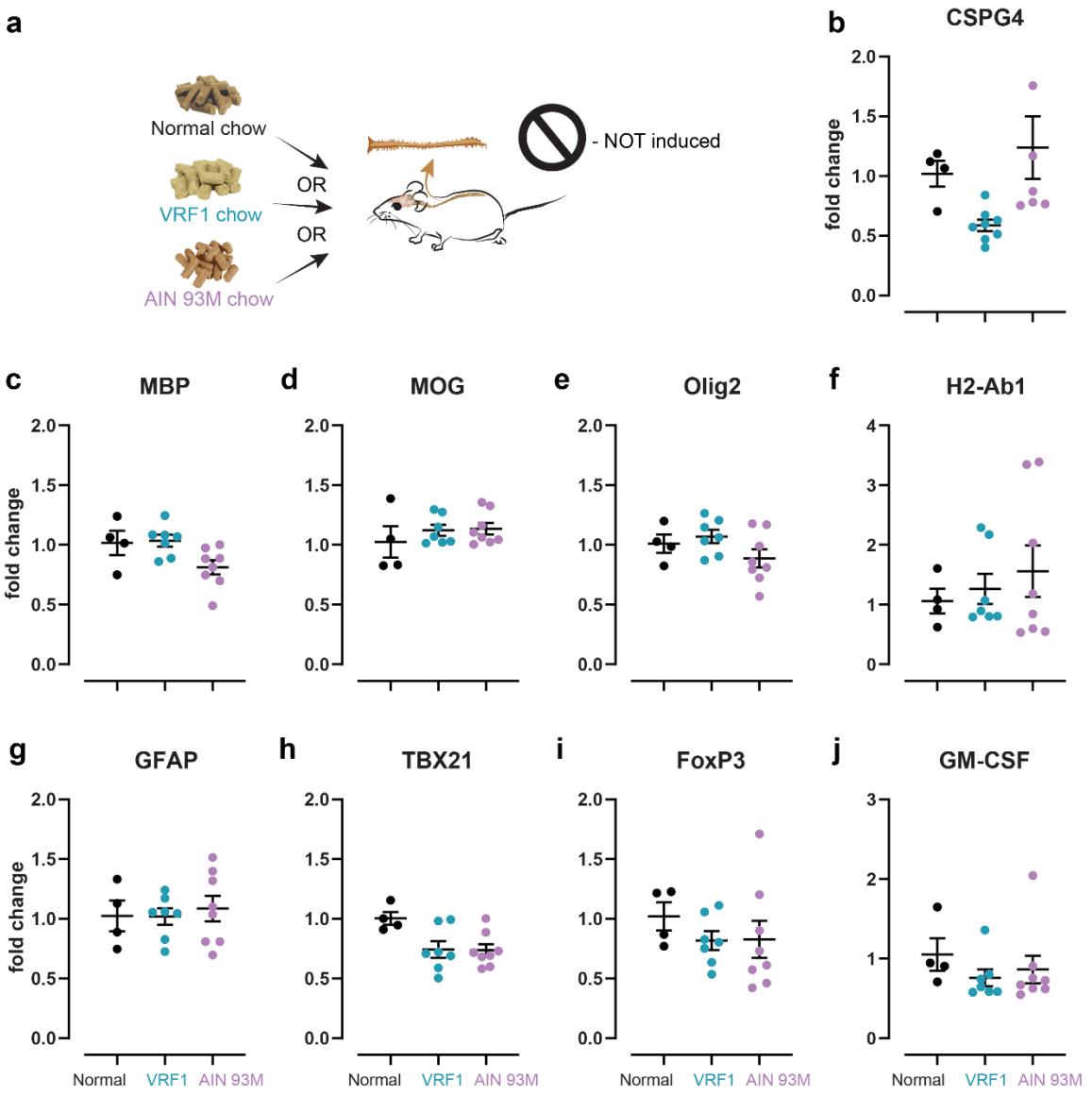

Figure 21. qPCR on spinal cords of un-induced mice pre-fed with different diets. **a**) Effect of diet (VRF1 versus AIN 93M versus Control diet) on NOT-induced female C57BL/6 mice in the spinal cord. **b-e**) Quantitative analysis of oligodendrocytes markers (*CSPG4*, *Olig2*) showing no diet effect on myelin markers. **f-j**) Quantitative analysis of the immune cell profile showing no difference, irrespective of diet. Data are displayed as mean ± SD of the mean, n = 4 to 8. AIN 93M results displayed in purple and VRF1 results displayed in cyan. This Figure is adapted from Martorelli *et.al*. 2024, under revision.

2.4 Discussion

The mouse model of MOG_{35-55}-induced experimental autoimmune encephalomyelitis delivered critical insight into the pathological mechanisms of human MS. For both, EAE in mouse and MS in human, auto-immunity, demyelination, inflammation and gliosis are critical disease hallmarks. Thereby, severity, incidence and disease onset can be modulated in the mouse via PTX-concentrations used for prime and boost, but also via variation of the mycobacterium tuberculosis content of the used Complete Freund´s Adjuvant (CFA).[54,55] In addition, important influential factors for the afore-mentioned disease hallmarks are the used diet and the age.[39,46,56] In addition, while the EAE model is well-validated in young C57BL/6 mice, usually in the age range of 6 to 12 weeks, there is a paucity of information and studies on middle-aged mice. This is especially the case for long dietary pre-feeding periods mimicking long-term dietary habits in humans. Thus, I investigated short-term (six weeks pre-feeding), as well as long-term (6 months pre-feeding) dietary effects on young and middle-aged mice, respectively. Overall, model aggressiveness was increased in younger animals in comparison to middle-aged mice. This is probably due to the observed downregulation of inflammatory cell markers, that was caused by both diets (VRF1 and AIN93 M). Thus, a prolonged exposure to these diets dampened the immune response and effectively caused a milder disease severity. On the other hand, downregulation of *CSPG4* (a hallmark protein of oligodendrocyte progenitor cells) after a short-term feeding period could amplify the damage in the short-term feeding model observed in adolescent mice (**Figure 13**). Moreover, a trained immune system has the effect of dampening immune response, especially autoimmunity.[57]

It has been shown for both mouse and human, that diet heavily influences and also controls encephalomyelitis disease.[48,49,56,58,59] Dietary components influencing onset, EAE-severity, weight-loss and incidence include, but are not limited to: sugar-, fiber-, iron-, vitamin E- or total protein content.[36–38,40,50,58–61] Three different diets were chosen for specific reasons: the control maintenance diet used in this study is a standard rodent diet used by many laboratories from all different areas of expertise, in both mice and rats. VRF1 on the other hand is for example used by Charles River as maintenance and breeding diet for C57BL/6 and Balb/c mice (personal correspondence with Charles River). Furthermore, in 1993, AIN 93 diets were developed in order to be produced from purified ingredients at reasonable costs to make in vivo experiments more consistent and reproducible. In particular, the AIN 93M diet is lower in protein and fat content, which makes it suitable for long term studies.[62] In direct comparison, the AIN 93M diet is produced from purified source material, while the used control maintenance diet and VRF1 are produced from seasonal grain by respective manufacturers (**Tables 26-28**). Thus, it is conceivable that seasonality can translate to differences in dietary composition (e.g., phytohormone content, which is not regularly tested by manufacturers), while

seasonality is improbable for the purified AIN 93M diet. This study clearly demonstrates that the purified AIN 93M diet causes a more severe EAE-model in comparison to the VRF1 diet, with higher average symptom scores, increased mortality and body weight loss. Data also showed a statistically significant difference in incidence between the two diets, with lower incidence in the VRF1 groups and a later onset of signs (**Figure 12**).

A critical factor for immune modulation in several autoimmune diseases is, in fact, associated with gut microbiota and their metabolites, which are heavily influenced by dietary macro- and micronutrients. Several studies show that diets rich in fiber, vitamin E and protein, while having a low sugar content, can play a key role in preserving gut microbiome composition, especially by regulating host physiology and macronutrients.[36,63] Various experiments underline that an altered gut microbiome is actually an environmental risk factor for autoimmune disease and it was also recently demonstrated that in MS patients, the microbiome is characterized by a reduction of bacteria belonging to the Clostridrium family.[64] Several studies show how changes in microbiome composition are associated with the regulation of pro-inflammatory cytokines. This shift towards a pro-inflammatory state has been demonstrated to have effects on intestinal physiology, leading to dysbiosis and successively causing intestinal barrier disruption. In addition, it is known that BBB breakdown and immune cell infiltration in the CNS are early hallmarks of MS.[29,65] This increase in intestinal permeability due to a loss of tight junction protein complexes allows bacterial antigens to bypass the intestinal lumen and reach the periphery. Higher levels of antigens circulating in the blood are associated with systemic inflammation that can lead to disruption of BBB integrity. This process, caused by an altered gut microbiome, can result in the passage of autoreactive T cells into the CNS that then have direct pathophysiological effects on myelin sheaths.[64] While it was not investigate diet-effects on gut microbiome composition and possible dysbiosis, fiber, vitamin E, protein, and sugar content largely differed between the VRF1 and the AIN 93M diet, possibly influencing gut microbiota content and composition (VRF1 diet contains 80 % more vitamin E, 77 % more protein, 294 % more iron per kg and 50 % less sugar in comparison to the AIN 93M diet). These findings on the influence of diet on EAE occurrence are in line with the work of *Berer et.al.*, who achieved similar results in a genetically vulnerable, spontaneous EAE model. There, mice were either fed with a control diet or a diet rich in crude fiber, especially cellulose. Animals kept on control diet had a significantly higher risk to spontaneously develop EAE. However, unlike in this studies, diet had no influence on BW or scores.[56]

A recent study compared the antioxidant response of the liver of Swiss strain mice. Mice were kept either on AIN 93M, or on a commercial diet richer in vitamin E and fiber. Interestingly, mice fed with the AIN 93M diet displayed an increased Reactive Oxygen Species (ROS) production and decreased antioxidant enzyme activity. In addition, the study demonstrated that vitamin E, protein and iron affect the activity of enzymes involved in the removal of ROS – which fits to the obtained results as AIN 93M is in direct

comparison to VRF1 (among other factors) deprived in vitamin E, protein and iron.[66,67] Moreover, in MS, sugar intake leads to activation of the TGF-α immune messenger protein, resulting in enhanced proliferation of immune cells.[58] In addition, several studies demonstrated that an increased dietary protein intake is also associated with a beneficial change in the gut microbiota composition and a more balanced immune profile.[68,49,69] Dysfunction of the BBB can also be caused by abnormal metabolism of iron, and can result in iron deposition in the brain.[63] Iron is essential for the integrity of the BBB as well as for regular cell function in the CNS.[36,64] Not surprisingly, deviations in iron metabolism are often associated with neurodegenerative diseases such as MS and Alzheimer's Disease.[38,60] Furthermore, iron is essential as a co-factor for enzymes crucial for oligodendrocyte function and therefore for myelination and neuronal stability.[61,37] It has been demonstrated that astrocytes channel iron to oligodendrocytes as protein-bound iron. When oligodendrocytes are deprived of iron, proliferation and differentiation of oligodendrocyte precursor cells (OPCs) is impaired, leading to a delay in remyelination after injury in vivo.[43,61] Astrocytes are the most abundant cell population in the CNS. They have different functions in maintaining the integrity of the CNS, such as BBB stability and transmission and modulation of nutrients for neurons. Excessive astrocyte activation, following inflammatory mechanisms occurring in neurodegenerative disease, leads to neuronal toxicity and scar formation, both in the brain and spinal cord. Studies also showed that astrocyte activation is often affected by multiple factors, one of the most important being gut flora mediated metabolites.[70] Simply increasing vitamin content can reduce EAE severity while decreased sugar intake also has beneficial effects in the EAE model.[46] In addition, Vitamin E has been shown to increase remyelination [47], which could also explain the less severe disease development in mice fed with VRF1 diet. In summary, the VRF1 diet contains higher amounts of ingredients which are known for their antioxidative properties, as well as for their beneficial effects on microbiota composition, inflammation, astrocyte and oligodendrocyte proliferation and activity.

To investigate the impact of diet, MOG_{35-55} preparation and PTX dose, gene expression analysis of markers associated with BBB damage, neuroinflammation, demyelination and neurodegeneration were analyzed. These findings showed that disease severity and incidence is strongly associated with neuroinflammation and BBB disruption, as expected. Furthermore, in AIN 93M fed mice, microglia and astrocyte associated markers were upregulated, underlining their key role for disease development and severity. These findings were underlined by histological examinations, proving higher-grade demyelination and astrocytosis in AIN 93M fed mice, while this was attenuated by feeding the VRF1 diet.

Besides dietary effects, in this project the impact of the preparation method of the MOG_{35-55}-CFA emulsion used for induction of EAE was investigated. I compared two protocols: one preparation method included intermittent sonication of the peptide/CFA-emulsion, while the second method did not include this sonication step. Results showed

that sonication of the emulsion was associated with higher EAE scores, increased body weight loss, as well as increased incidence and mortality, although most of the effects were only apparent when comparing groups fed with the AIN 93M diet. Importantly, the sonicated emulsion resulted in robust model induction, while the un-sonicated MOG preparation led to model variability. Since sonication leads to a more homogeneous emulsion with finer droplets, I assume that the epitopes in the +son groups are more accessible to cellular antigen recognition mechanisms. In addition, smaller particles may bear a stronger resemblance to natural instigators of immune reactions (e.g., viruses or bacteria) and thus cause a more intense initial response. Alternatively, a more finely dispersed emulsion will be better distributed into nearby tissues after s.c. injection, where it activates cells of the innate immune system, and thus results in stronger effects. When comparing the different experimental groups and conditions, it is clearly evident that the change in diet had a more decisive influence on disease severity compared to the two emulsion preparation methods. Average EAE scores in the AIN 93M groups on day 17 (Study 1) were 2.2- (-son) and 2.4- (+son) -times as high as the corresponding VRF1 group scores, respectively. Conversely, sonicating the emulsion only increased average scores by 11 % (VRF1 diet) and 19 % (AIN 93M diet). Therefore, I conclude that severity of disease is mostly influenced by diet, while the sonication process is fundamental for robustness and probably also reproducibility of the model *per se*.

Finally, in this study the effect of both, MOG_{35-55}- and PTX-dose on the model was investigated. Surprisingly, lowering the dose of MOG_{35-55} used for disease induction from 300 µg per mouse to 150 µg per mouse had no effect on incidence, severity or body weight loss. In contrast, lowering both MOG_{35-55}- and PTX-dose (MOG: 300 µg to 150 µg; PTX: 240 ng to 120 ng) significantly reduced incidence, severity and body weight loss. This was reflected by reduced *TBX21-, GM-CSF-, GFAP*- and *CSPG4*-induction in the brain. In the spinal cord, on the other hand, *Olig2* and *CSPG4* were elevated in direct comparison to the remaining experimental groups (**Figures 15** and **16**). Likely, the lowered PTX-dose was insufficient for robust disruption of the BBB.

To investigate diet-effects in the early phase of EAE (pre-symptomatic phase), satellite animals were terminated 7 days after induction. For these satellite groups, sonicated emulsions was used to produce robust effects, as expected a high degree of variability in the expression level in the early phase in combination with the variable induction quality of the non-sonicated peptide emulsion preparation. Also, in the satellite groups, the full dose of both MOG_{35-55} and PTX were respectively used. Surprisingly, robust *TBX21*-expression was found at day 7 post induction in the brain, but not in the spinal cord, while *Olig2*-expression was significantly reduced in satellites that were pre-fed with AIN 93M, but not VRF1. In addition, *MOG* was also found to be significantly down-regulated in the spinal cord of AIN 93M-fed satellite animals. Thus, pre-feeding AIN 93M, but not VRF1 had an impact on the pre-symptomatic demyelination and inflammatory response to EAE-induction.

To complement this body of data, next the dietary effects in naïve animals that received no EAE-induction (AIN 93M and VRF1, as well as the Control diet were fed for 2 weeks, respectively) was also investigated. While data showed no significant differences in the expression profile of either analyzed marker in the spinal cord, dietary effects in the brain were found. *CSPG4*, *GFAP* and *MBP* were significantly downregulated in both, AIN 93M and VRF1 fed groups, while *H2-Ab1* was significantly downregulated in the AIN 93M group. These results are worrying in the context of the origin, and dietary husbandry of mice used for EAE-studies in different institutions worldwide.

2.5 Conclusions

Taken together, this project showed that age and diet have a major impact on disease severity, incidence and on the gene expression pattern in EAE-studies, while the MOG_{35-55}-CFA-emulsion preparation method has implications for robustness and variability of the model. This study demonstrates that more harmonization between centers is needed, especially with respect to mouse husbandry.

Chapter 3

P38α MAP Kinase inhibitors decrease severity of signs and increase animal survival in a mouse model of MS

Abbreviations:

%, Percentage;

°C, Celsius degree;

ACA, anterior commissure, anterior part;

ACN, Acetonitril;

AD, Alzheimer's disease;

BBB, Blood-brain-barrier;

CFA, Complete Freund's Adjuvant;

CNS, Central nervous system;

CO_2, Carbon dioxide;

DMDs, Dimethyl disulfide;

DMTs, Disease-modifying treatments (DMTs);

EAE, experimental autoimmune encephalomyelitis;

EBV, Epstein-Barr virus;

ESI, Electrospray Ionization;

FDA, Food and drugs administration;

H&E, Hematoxylin Eosin;

HPLC/MS/MS, Liquid Chromatography with tandem mass spectrometry;

i.p., Intra Peritoneal;

IL1β, interleukin 1 beta;

IL-6, Interleukin 6;

IS, Internal Standard;

LC-MS, Liquid Chromatography mass spectrometry;

MAP, Mitogen-activated protein;

MBP, Myelin Based protein;

MOG_{35-55}, Myelin Oligodendrocyte Glycoprotein;

MS, Multiple sclerosis;

NDF, Neutral Detergent Fiber;

OPCs, Oligodendrocyte Progenitor Cells;

p.o., Per oral;

pg, Picogram;

PTX, Pertussis Toxin;

qPCR, Quantitative Polymerase Chain Reaction;

ROS, Reactive Oxygen Species;

S1p, Sphingosine-1-phosphate receptors;

TMEV, Theiler's Murine Encephalomyelitis Virus;

TNFα, Tumor necrosis factor α.

3.1 Introduction

In the previous chapter it was discussed the EAE animal model and how it is used for studying MS, an autoimmune disease affecting the CNS. This well-known murine model was optimized, by immunization with MOG_{35-55}-CFA-peptide sonicated emulsion and PTX injection, in combination with a low fiber high sugar diet (AIN 93M) and obtained a more stable model in order to get reliable results for drug efficacy testing.

As already discussed in **Chapter 1**, p38α MAP Kinase inhibitors are a class of drugs that target the p38 MAP Kinase signaling pathway, which is involved in various cellular processes, including inflammation and immune responses. Due to their inhibiting activity, in this chapter, two of these inhibitors have been investigated for their potential therapeutic effects in EAE and MS.

As already described in **Chapter 2** of this thesis, MS is a chronic autoimmune/inflammatory CNS disease characterized by attacks of the myelin protein shielding the neurons or the axons. The progression of MS is varied and unpredictable. In most patients, the disease is initially characterized by episodes of reversible neurological disabilities, which is often followed over time by progressive neurological degeneration.[71] From 250,000 to 350,000 patients in the U.S. are affected by MS, and 50 % of these patients will need help walking within 15 years after the onset of the disease.[72]

The cause of this neurodegenerative disease involves a combination of genetic susceptibility and a nongenetic trigger, such as a virus, diet and metabolism, or different environmental factors, that together result in a self-sustaining autoimmune and inflammatory disorder that leads to recurrent immune attacks on the CNS, leading to demyelination of neurons by T cells, microglia and B cells.[71] The correlation between Epstein-Barr virus (EBV) infection and MS has been reported as highly associated risk in several epidemiological studies.[73] The mechanism of EBV causing MS remains unknown but it is believed to lead to the production of autoreactive immune cells responsible for the aberrant self-targeting immune response *versus* the myelin protein present in the CNS.[74] MS pathogenesis can be explained by autologous myelin reactive T cells initially primed with antigen presenting cells (APC) in the periphery (lymph nodes) that then cross the corrupted BBB entering the CNS. Within brain and spinal cord, these leukocytes could activate macrophages and microglia which both release cytokines promoting local inflammation and myelin destruction (**Figure 22**).[74] The myelin damage occurring in both brain and spinal cord can slow or block the electrical signals that carry information between the CNS and the rest of the body. Typically occurring signs are: problems with vision, movement, muscle strength, coordination and thinking.[75] Nowadays, no treatment has been officially approved by the FDA, but different immune cells modulators drugs are approved for second or third clinical phase trials such as Disease-modifying treatments

(DMTs), targeting sphingosine-1-phosphate (S1p) receptors and monoclonal antibody-based therapeutics on B cells and Tregs.[74]

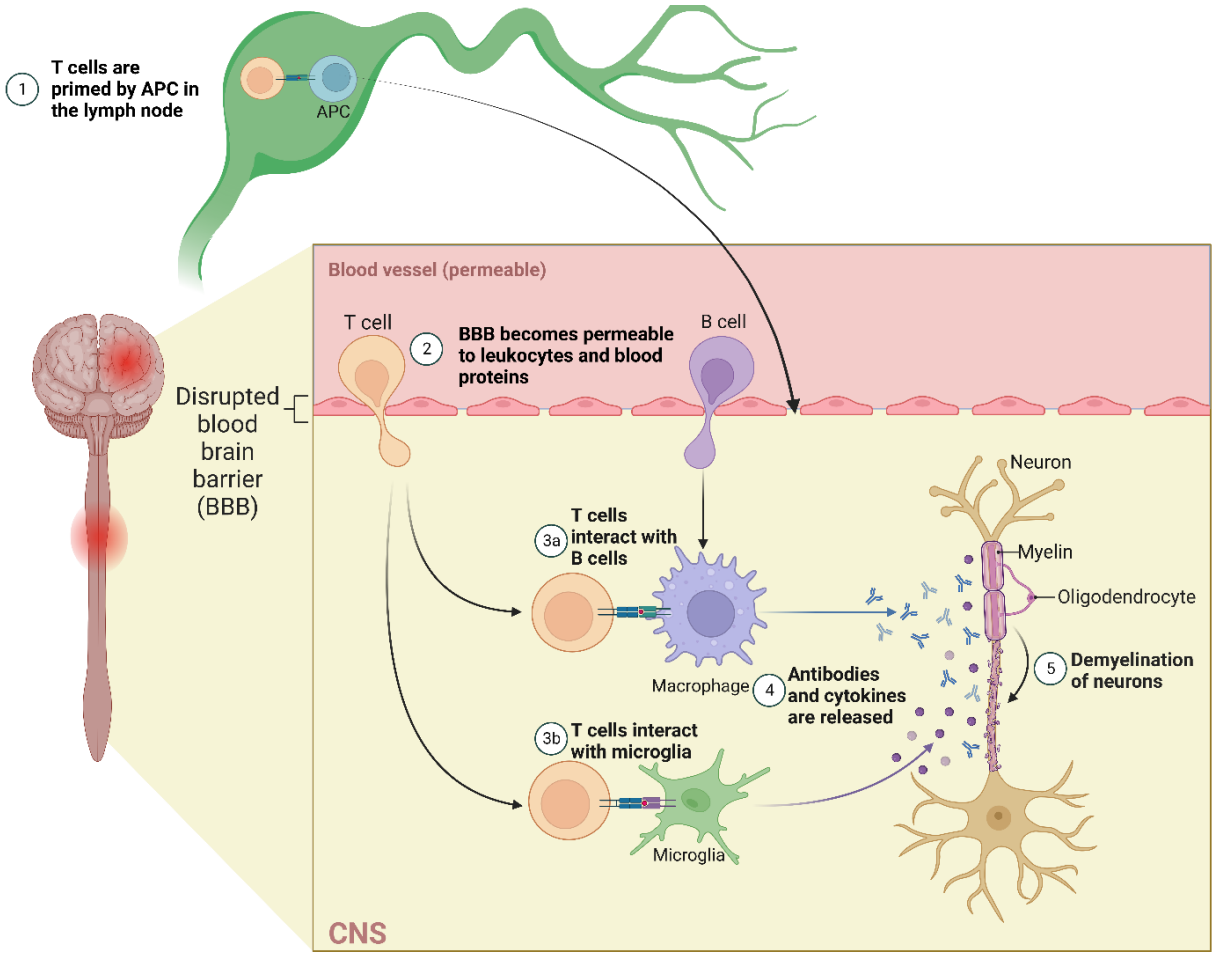

Figure 22. The inflammatory phase of multiple sclerosis. T cells are primed in the periphery (**1**) and migrating with the B cells in the CNS trough a disrupted BBB (**2**). After autoreactive T cells, B cells (including macrophages) enter the CNS primed with macrophage and microglia (**3a** and **b**), that secrete inflammatory cytokines and antibodies (**4**). The damage on the oligodendroglial cells forming the myelin sheath on axons leads to neurodegeneration (**5**). The injured myelin cannot conduct electrical impulses normally, leading to an abnormal transmitting signal and consequent symptoms such as: double vison, vision loss, eye pain, muscle weakness, and loss of sensation or coordination This figure was created with BioRender and adapted from Rongzeng Liu *et. al*.[74]

The p38 MAP Kinase pathway is involved in the production of pro-inflammatory cytokines, such as TNFα, IL-1β, and IL-6, which contribute to the inflammatory cascade observed in EAE and MS. Different hypotheses suggest that p38α MAP Kinase inhibitors are good candidates for MS treatment: **i**) by inhibiting p38 MAP Kinase, these inhibitors can reduce the production of pro-inflammatory cytokines and dampen the immune response, leading

to a decrease in disease activity; **ii**) It has also been demonstrated that, p38 MAP Kinase inhibitors can modulate the function of immune cells, such as T cells and macrophages, which play a central role in EAE pathogenesis. By inhibiting p38 MAP Kinase, these inhibitors can suppress the activation and migration of these immune cells to the CNS, where they can cause damage; **iii**) As is well known, EAE and MS involve damage to the myelin sheath and nerve cells in the CNS. P38α MAP Kinase inhibitors may have a neuroprotective effect by reducing inflammation and preventing damage to the myelin sheath and neurons; **iv**) In addition, p38α MAP Kinase inhibitors can help to maintain the integrity of the BBB. Disruption of the BBB is a common feature in EAE and MS, allowing immune cells to enter the CNS. By stabilizing the BBB, p38α MAP Kinase inhibitors may limit the infiltration of immune cells into the CNS.

In the past 10 years, several preclinical studies using the EAE model showed that p38α MAP Kinase inhibitors lead to promising results in reducing disease severity and improving neurological signs. Three of the most investigated ones are: SB203580, SB239063, and BIRB 796. As expected, these inhibitors have shown efficacy in ameliorating clinical symptoms, reducing inflammation and demyelination in the central nervous system, and inhibiting the infiltration of immune cells into the brain and spinal cord.[3]

While SB203580 was found to inhibit the activation of immune cells and reduce their infiltration into the CNS, leading to a decrease in demyelination and axonal damage, treatment with SB239063 attenuated the development of clinical symptoms, reduced inflammation in the CNS, and inhibited the production of pro-inflammatory cytokines. SB239063 was also found to modulate the balance between regulatory T cells and effector T cells, leading to a more controlled immune response. On the other hand, BIRB 796 treatment resulted in reduced disease severity, decreased inflammation and demyelination in the CNS, and improved motor function. BIRB 796 was also found to inhibit the activation of microglia, which are immune cells in the CNS involved in the inflammatory response.[3,76]

These studies collectively suggest that p38 MAP Kinase inhibitors have the potential to modulate the immune response and alleviate EAE symptoms by reducing inflammation, inhibiting immune cell activation, and protecting against demyelination and axonal damage.

However, it is important to note that the translation of these findings to clinical applications in MS patients is still in progress. While preclinical studies have shown promising results, the effectiveness and safety of p38 MAP Kinase inhibitors in human trials are yet to be fully determined. Even if some of the compounds showed promising results in the treatment of MS, none of the p38 MAP Kinase candidates resulted in a good candidate in clinical trials of MS patients. The failure of p38 MAP Kinase inhibitors in

clinical trials for MS patients can be attributed to several factors such as lack of efficacy because of side effects in the liver.[77]

In summary, p38 MAP Kinase inhibitors have shown potential in preclinical studies using EAE models by modulating the immune response, reducing inflammation, and protecting against demyelination in the CNS. However, further research is required to determine their therapeutic potential and to establish their safety and efficacy in human MS patients.

Aim

In this project, I tested two different p38 MAP Kinase inhibitors on 14 weeks-old EAE induced mice, previously characterized *in vitro* and *in vivo* (see **Chapter 1** of the thesis), that showed no toxicity effects. Their potential beneficial effect in the reduction of the severity of the EAE model were evaluated and the possible side effect on the liver was also investigated. Compound **11** and compound **13** were selected based on their *in vitro* and *in vivo* potency (TNFα IC_{50}= 1.3 ± 0.1 and 5.3 ± 0.6, respectively) and their difference in the analytic results. Compound **11** did not cross the BBB while the second compound (slightly less potent) was found in brain and spinal cord (see **Table 14**-**15** and **22**-**23**). In this study, it was demonstrated that inhibition in the periphery leads to a better therapeutic effect in terms of survival and severity of the disease. The results showed that compound **11**, mostly accumulating in liver and spleen but not in the CNS, increased the survival of the EAE induced animals while decreasing the severity of the symptoms from severe to mild-moderate.

3.2 Material and Methods

Induction materials:

Heat-inactivated M. tuberculosis (strain H37RA) and Complete Freund's Adjuvant (CFA) (1 mg/mL heat-inactivated mycobacterium tuberculosis) were both obtained from Difco, Product No. 11719062, USA; the murine MOG_{35-55}-peptide (MEVGWYRSPFSRVVHLYRNGK) was obtained from Panatecs, Product No. AU-P-3596, Germany while Pertussis toxin was obtained from Sigma Aldrich, Germany.

Diets:

The certified AIN 93M diet from SSNIFF® Spezialdiäten GmbH, Soest, Germany was used for experimental diets as indicated in the **Figure 23**.

Preparation and administration of CFA/MOG_{35-55}-peptide emulsion:

The 300 µg/mice MOG_{35-55}/CFA emulsion was prepared accordingly to **paragraph 2.2** of **Chapter 2** using the sonication method.

Preparation and injection of PTX solution:

The PTX stock was freshly prepared by diluting powdered PTX with sterile 1X PBS to a final concentration of 1 µg/mL (240 ng). The first PTX-injection (i.p.) was done immediately after the administration of the MOG_{35-55}-peptide emulsion, the second PTX-injection (i.p.) was given 48 h after the first. Groups were injected with 240 ng PTX on both days (**Table 35**).

Animals:

28 7-week-old female C57BL/6 mice were obtained from Janvier Labs. Before the study was initiated, an acclimation phase of seven days was necessary (**Figure 23**). Animals were held 6 weeks prior to MOG/PTX induction on the AIN 93M diet. Animals were provided with food and water ad libitum and on day 0 induced with MOG_{35-55}-peptide sonicated and PTX-injection (**Figure 23**). Four not induced animals were pre-fed with Control diet (**Table 28**, **Chapter 2**) and used as baseline controls for the qPCR downstream analysis (group 1) while eight induced animals per group were pre-fed with the AIN 93M diet (**Table 26**, **Chapter 2**) and treated with 0.5 % citric acid (vehicle, group 2), compound **11** (group 3) and compound **13** (group 4) (**Table 35**). After the first symptoms occurred, animals were daily p.o. treated with 0.5 % citric acid, compound **11** or **13** (12 µmol/kg) according to the group design (**Table 35**) until the end of the study. Euthanasia was performed by CO_2 inhalation at study termination (day 17). Brain and spinal cord samples were collected for qPCR (flash-frozen in liquid nitrogen and stored at -80 °C until processing) and for histological samples (directly transferred to 4 % PFA, and 24 h later stored in 70 % EtOH until further workup, see histology paragraph of the Materials and Methods section). Ethical approval for the study was obtained from local authorities (Regierungspräsidium Tübingen, approval number SYN 04/21).

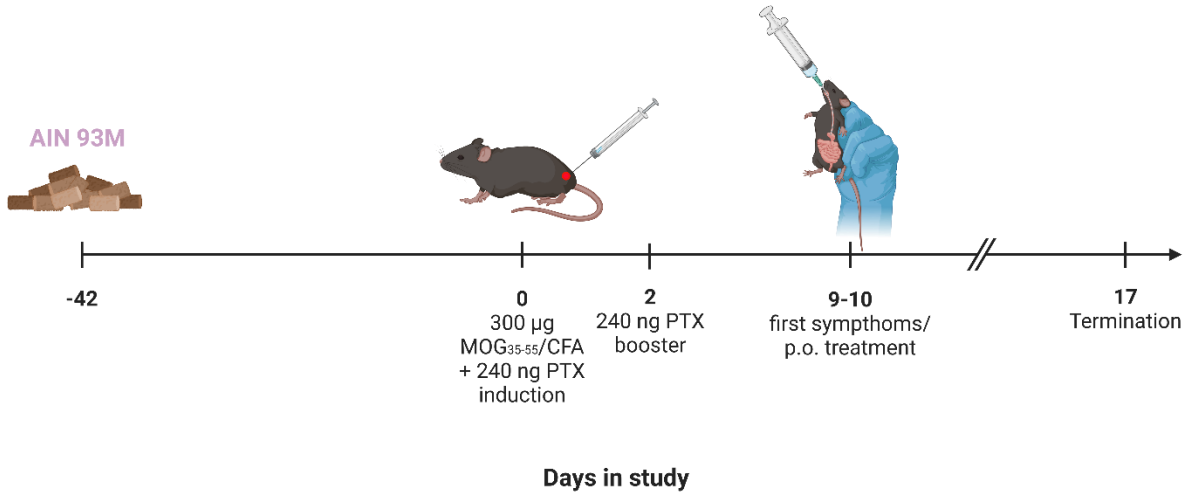

Figure 23. C57BL/6 female mice were pre-fed for six weeks with AIN 93M diet. Then, EAE was induced by subcutaneous injection of MOG_{35-55}-CFA emulsion. MOG_{35-55}-peptide was administered as a sonicated emulsion. PTX i.p. injection was done on days 0 and 2 (relative to MOG_{35-55}-injection). On day 17 post MOG_{35-55}-induction, mice were euthanised.

Table 35. Experimental groups

Group No.	N	Chow	Treatment	Route	Dose [mg/kg]	MOG_{35-55} per animal	PTX per animal	Emulsion preparation
1	4	Control diet	-	-	-	-	-	-
2	8	AIN 93M	Vehicle	p.o.	5	300 µg	240 ng	+son
3	8	AIN 93M	11	p.o.	5	300 µg	240 ng	+son
4	8	AIN 93M	13	p.o.	5	300 µg	240 ng	+son

Clinical observations were detected according to a standardized scoring system (see **Table 29**, **Chapter 2**). Body weight was assessed daily, starting on day 1 until the end of the experiment. Exemptions being day 0, where in order to avoid additional stress for the mice that could impact disease development, the weighing was skipped. The scoring was evaluated by the same operator daily, beginning on the respective day of symptom-onset.

Formulation:

Eight female 14 weeks old CFA/MOG induced mice were treated with 0.5 % citric acid, 5 mL/kg (vehicle, group 2, **Table 36**) while n=8 animals per group were treated with 12 µmol/kg of compound **11** or **13**, respectively (in 0.5 % citric acid, 5 mL/kg, group 3 and 4, **Table 36**). Not induced control diet group received no treatment (group 1, **Table 36**).

LC-MS analysis:

The analytical methodology is an HPLC instrument, which comprised an Agilent 1260 Binary Pump (Inv. 0408), the CTC PAL Autosampler (Inv. 0409) and an Agilent 1260 thermostatted Column Compartment (Inv.0202). The HPLC system was coupled to a Triple Quadrupole API 4500 (Inv. 0406) (PM-41) Mass Spectrometer (ABSciex, Redwood City, California, USA). Data acquisition and processing were carried out with the Analyst® Instrument Control and Data Processing Software v. 1.6.2. Chromatographic separation took place at 40 °C using Restek Biphenyl 2.7 µm, 50*2.1 mm column. The mobile phase consisted of a gradient (see **Table 36**) of water + 0.1 % formic acid, and ACN + 0.1 % formic acid at a flow rate of 500 µL/min and an injection volume is 4 µL.

Table 36. Method mobile phase gradient

Total time (min)	Flow rate (µl/min)	A (%)	B (%)
0	500	90	10
1	500	90	10
3	500	0	100
6	500	0	100
7	500	90	10
10	500	90	10

A: Water+0.1 % Formic acid

B: ACN+0.1 % Formic acid

Positive ion electrospray ionization (ESI) mass spectrum assessment of p38 MAP Kinase inhibitors and the Internal Standard (IS) was carried out. P38 MAP Kinase inhibitors and terbuthylazine (internal standard) Q1/Q3 masses, dwell time and mass spectrometer analytes specific parameters can be found in **Table 37**.

Table 37. Mass spectrometer parameters for P38 MAP KINASE inhibitors and terbuthylazine.

Compound	Q1 mass (Da)	Q3 mass (Da)	DP (volts)	EP (volts)	CE (volts)	CXP (volts)
terbuthylazine	230.026	174.1	6	10	25	8
11	491.323	405.2	146	10	39	24
13	401.207	384.2	81	10	25	24

DP: Declustering potential. EP: Entrance potential. CE: Collision energy. CXP: Collision cell exit potential

Valve:

	Total time (min)	Position
1	0	Waste
2	3.5	MS
3	6.0	Waste

The calibration curves and quality controls were obtained by preparing a stock solution in DMSO with a final concentration of 10 mM. The calibration curve ranges were set from 5 to 100000 nM. The QCs had a concentration of 100, 1000, and 10000 nM.

Preparation and handling of samples for LC-MS analysis:

The samples produced were stored at -20 °C in Synovo's facilities until sample processing shortly prior to the HPLC/MS/MS process. The already processed samples were introduced directly into the auto-sampler or stored at 4 °C until measurement. The remaining samples were stored at -20 °C for further needs or requirements.

Plasma sample preparation for LC-MS analysis:

The samples were transferred into individual tubes and six volumes of ACN containing the IS (ACN-IS) were added to each sample (e.g. 10 µL plasma + 60 µL ACN-IS). After mixing and centrifuging for 5 minutes at 10000-11000 RCF (Eppendorf Centrifuge 5417R 10,000 rpm), the supernatant was transferred into a properly labelled glass auto-sampler vial.

When diluting of the samples was needed due to too high concentration or too little sample volume, the samples were diluted in a similar matrix as the samples (e.g. plasma from same animal strain). When diluting the samples, the dilution factor was considered in the data acquisition and calculations.

Tissue sample preparation (e.g. brain, liver) for LC-MS analysis:

The tissue samples were weighed and one volume of proteinase K solution was added. The tissue was digested by incubation with proteinase K at 50 °C for 1-3 h. After the incubation, the tissue was mechanically broken. The digested tissue was mixed with six volumes of ACN containing the internal standard. After centrifugation, the supernatant was taken and introduced in a properly labelled glass auto-sampler vial.

Total RNA isolation and quantitative RT-PCR:

Using a FastPrep-24 5G instrument (MP Biomedicals), flash frozen liver, brain and spinal cord samples were homogenized in lysis buffer (Jena Bioscience). Total RNA was isolated using Total RNA Purification Kit (Jena Bioscience) according to the manufacturer's instructions. RNA quantity and purity were evaluated spectrophotometrically with the Nanodrop NP-80 instrument (Implen). After DNase I treatment (PerfeCTa DNase I, Quanta Bioscience), 500 ng of total RNA was transcribed into cDNA with 5x PrimeScript RT Mastermix (Takara). using Blue S'Green qPCR Mix Separate ROX (Biozym) according to the manufacturer´s instructions, the qPCR reaction was performed on the QuantStudio® 3 real-time polymerase chain reaction (PCR) system (ThermoFisher Scientific/Quantstudio™ Design & Analysis Software v.1.4.3). Relative expression levels were determined using the 2−ΔΔCT method and HPRT was used as reference gene[47] and not-induced animals fed with the same diet (AIN 93M) were used as control group. Primer sequences are listed in **Table 38**.

Table 38. Primer list used for quantitative RT-PCR

Gene	Forward Primer	Reverse Primer
Hprt	AGTTCTTTGCTGACCTGCTG	CCACCAATAACTTTTATGTCCCC
Mbp	CGAGGAGAGGCTGGAAAGAA	TGCTTGGAGTCTGTCACCG
TNFα	GAGGGAAGAAGCAGCCATTG	GGCAAGTCCCAACATCAACA
IL-6	ACTTCACAAGTCGGAGGCTTA	TCTGCAAGTGCATCATCGTT
Olig2	CCACACACACACCTTTTGCC	CACGTTGTAATGCAGGTCGC
IL17A	CCACCACGCTCTTCTGTCTA	CTGATGAGAGGGAGGCCATT
CXCL16	AGTGGGTCCGTGAACTAGTG	GTCTGGGTACTGGCTTGAGG
TGF-β1	CTACTATGCTAAAGAGGTCACCC	CCCGAATGTCTGACGTATTGA
IL-10	AGAGAAGCATGGCCCAGAAA	CTCCACTGCCTTGCTCTTATTT
GLUT5	CACTTTGAGGAGGTGAGCCG	GGCAGCTACGTTGTACCCAT

Histology instruments:

Histological preparation of samples was performed using a paraffine dispenser fitted with an MPS/S dispensing module (SLEE Medical), Paraplast Plus (Leica BioSystem, art.-no.

X881.1 REF 39602004). A HM325 Manual Microtome (Leica BioSystem) was used to perform 5 µM cuts. Cuts were mounted on glass Superfrost PLUS or Superfrost R (Langenbrinck GmbH, art.-no.03- 0060) slides. Using the same exposure and intensity for each sample, H&E and immunohistochemical images were acquired with 3D HISTECK, panoramic scanner 2.1.1.

Protocols:

Hematoxylin-Eosin staining (H&E):

After the deparaffinizing and dehydrating steps using 100 % xylene (isomeric mixture, ACROS ORGANICS), increasing ethanol (VWR Chemicals) dilutions and water on liver, brain and spinal cord slides (5 µm cut), Eosin Y (1 % aqueous solution, Bio-Optica) was used to stain cytoplasm while Mayer's Hematoxylin (Bio-Optica) was used to stain nuclei.

MBP immunostaining:

After the deparaffinizing and dehydrating steps using 100 % xylene (isomeric mixture, ACROS ORGANICS), increasing ethanol (VWR Chemicals) dilutions and water, antigen (epitope) retrieval was performed using citrate buffer (45 min at 90 °C). After the washing steps (3 x 5 min in PBS), blocking was performed for 60 min at room temperature with 5 % Normal serum Blocking solution (BioLegend) in 0.3 % Triton X-100 in PBS. Incubation with the Myelin base protein (MBP) primary antibody was done overnight at 4 °C. After washing steps (3 x 5 min in PBS), incubation with the secondary antibody was done for 45 min at room temperature (1:400 sheep anti-rabbit lgG, Alkaline Phosphatase, antibodies-online, product n. ABIN102021). Dako kit (liquid permanent red) was used as a substrate reaction.

Statistics:

Statistical analysis and preparation of graphs were done using GraphPad Prism 9.3.1. All experimental results were tested for normal distribution using the Shapiro-Wilk test. Before conducting further statistical analysis, the Brown-Forsythe test was used to test data for homoscedasticity while ordinary one-way ANOVA was used for multiple comparisons (Bonferroni correction). Incidence was compared using the Chi^2 test and p-values were corrected with the Bonferroni method for multiple comparisons. EAE-scores were compared using multiple Mann-Whitney tests with two-stage step-up (Benjamini, Krieger, and Yekutieli), p-values were corrected with the Bonferroni method for multiple comparisons. Significance levels are indicated by * $p < 0.05$; ** $p \leq 0.01$; *** $p \leq 0.001$; **** $p \leq 0.0001$.

3.3 Results

The peripherally *active compound showed increased survival and a less severe EAE scoring*

In order to evaluate a possible therapeutical effect of the selected compounds, a study with 28 female C57BL/6 mice was performed (**Table 39**) where 24 animals were EAE induced after 6 weeks pre-feeding with the AIN 93M diet and 300 µg/mice MOG_{35-55}/CFA sonicated emulsion s.c. and 240 ng/mice PTX i.p. injection. Two p38α MAP Kinase inhibitors (Skepinone derivative number **11** and **13**, **Chapter 1**) showed high potency *in vitro* and *ex vivo* (TNFα IC_{50} = 1.3 ± 0.1 and 5.3 ± 0.6, respectively) but different organ affinity: compound **11** was found in the periphery (liver and spleen) while compound **13** was present in the CNS (brain and spinal cord). Control mice (group 1, n=4) did not receive any MOG/CFA emulsion injection (**Table 35**). Analytic results were analyzed in order to evaluate the kinetics and the metabolism of the selected compounds after eight days of daily p.o. application while the last injection was done 2 h before termination/organ collection. As shown in **Figure 24a**, compound **11** has a faster clearance from tail plasma compared with compound **13**.

As already discussed in **Chapter 1** of the thesis, also in this *in vivo* experiment, after daily p.o. treatment from day 9 to day 17 (12 µmol/kg), compound **11** was not BBB penetrant while compound **13** was found in the brain and spinal cord (60 ± 25.7 nM and 112 ± 28.2 nM, respectively). Both compounds were detected by LC-MS in the periphery in liver and spleen: compound **11** with an average concentration of 364 nM and 250 nM respectively, while compound **13** with an average of 39 nM and 125 nM respectively (**Figure 24b**).

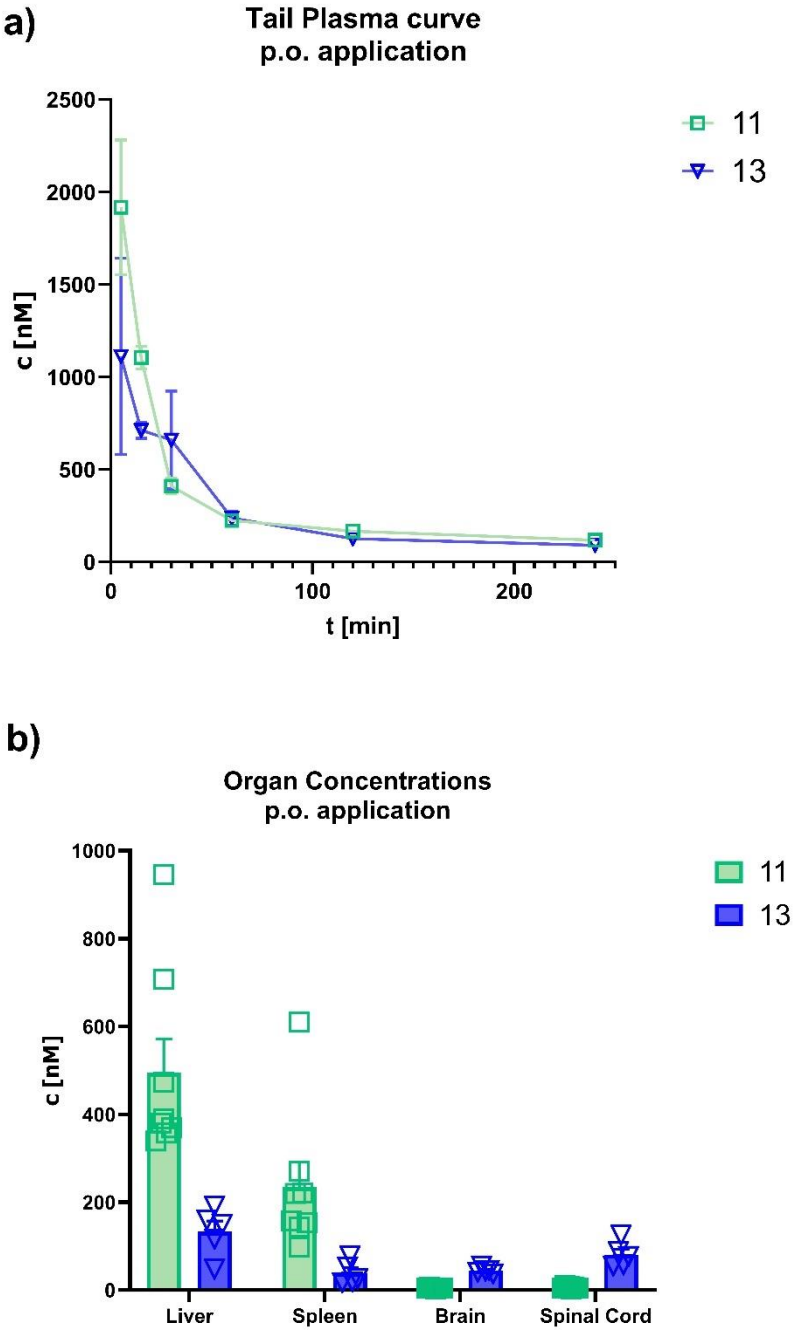

Figure 24. Analytic results. **a)** Tail plasma curve after p.o. application of 12 µmol/kg of compounds **11** and **13** at day 17 post induction. Tail blood was taken after 5 min, 15 min, 30 min, 60 min, 120 min and 240 min. **b)** Concentrations of compounds **11** and **13** in liver, spleen, brain and spinal cord after p.o. administration of 12 µmol/kg at 240 min. Values are displayed as mean ± SD. Compound **11** results are displayed in light green (square shape) and **13** results are displayed in violet (triangle shape).

Body weight did not differ between groups until the end study (**Figure 25a**). All groups showed a loss of body weight at day 17 of ~ 15 % while, on the other hand, in the first half of the study (day 8), representing the latent symptom free phase of EAE, all groups reach 10 % body weight gain.

Average disease score over time (calculated by the AUC of the score time curve) differed significantly between vehicle animals' versus compound **11** treated animals ($p \leq 0.01$) while, on the other hand, compound **13** treated animals did not show less severe signs when compared to vehicle group mice (**Figure 25b**). Also, compound **11** treated mice showed 88 % survival (only one animal was terminated due to the severity of the signs developed), while numerous vehicle mice and compound **13** treated mice needed to be terminated before day 17 after reaching scoring ≥ 4.5, resulting in only 25 % and 30 % survival, respectively on study day 17 (**Figure 25c**).

These results are interesting at several levels. First, that although **11** and **13** are similar in cell-based assays, and plasma exposure, they differ in overall effect in EAE. Secondly, that a more peripheral inhibition of the immune response is more effective in EAE in terms of severity and survival, even when given after the onset of signs. This probably reflects the situation that EAE is induced in the periphery with central signs being a later manifestation. However, in this study, compound **11** was given first on day 9-11 when the animals had reached at least score 0.5. This indicates that even when immune cells have just entered the CNS and spinal cord, compound **11** is still able to exert an effect that restricts their action in the nervous system. The effect was observed after a delay of 4-5 days. This may reflect the time required for the substance to reverse the phenotype of cells in the CNS or inhibit the maturation of peripheral cells that would normally migrate to the CNS.

In contrast to the therapeutic effects shown here, most studies with agents like p38 inhibitors tend to focus on early or prophylactic dosing to disrupt antigen presentation and inflammatory responses to the antigen after inoculation.

That compound **11** is active at such a late stage is a positive sign for its general activity and clinical potential.

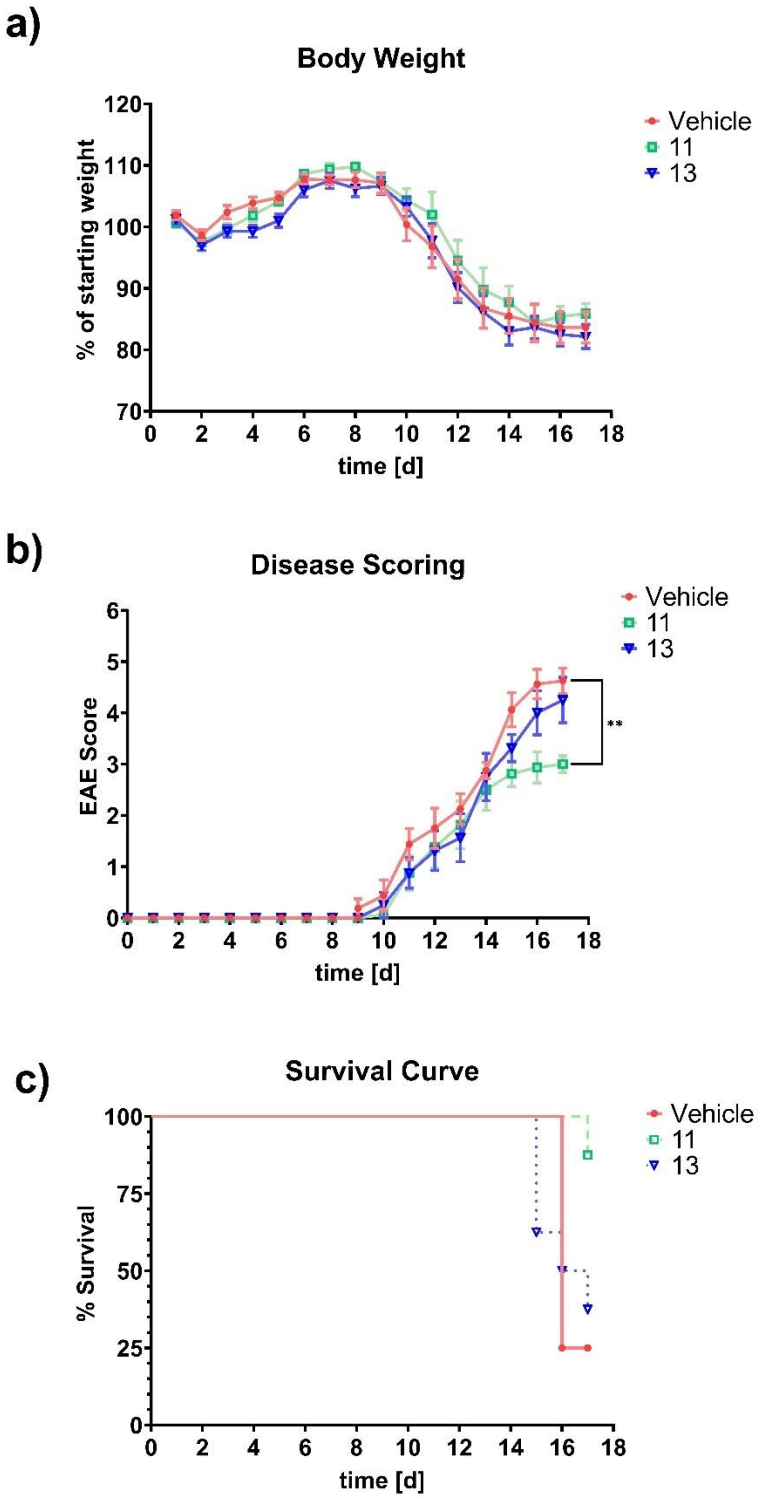

Figure 25. In vivo parameters after EAE induction. P.o. administration of 12 µmol/kg was daily after first signs occurred in individual mice (Scoring ≥ 0.5, e.g. day 9 or 10). Body weight (**a**) and symptom scores (**b**) were assessed daily and survival of EAE animals was recorded until day 17 of the study (**c**). Values are displayed as mean ± standard error of the mean. * $p < 0.05$; ** $p \leq 0.01$;

*** $p \leq 0.001$; **** $p \leq 0.0001$. Vehicle results are displayed in red (circle shape), compound **11** results are displayed in light green (square shape) and compound **13** results are displayed in violet (triangle shape).

The peripherally active compound showed reduction of apoptosis marker and increased myelin preservation in brain by qPCR and histology

To investigate mechanism conferring the effect of the two compounds on EAE, qPCR and histological analysis were performed on brains. Whereas, mRNA expression of pro-inflammatory markers were not regulated by compound treatment, the apoptosis marker Casp3 was downregulated in the brains of compound **11** treated mice (** $p \leq 0.01$), indicating protection against neuronal loss in the brain (**Figure 26**). In order to evaluate myelin loss in the brain, MBP IHC assay was performed in coronal sections of each brain. Myelin is found to be disrupted in the vehicle group in different regions of the brain, while compound **11** treatment preserved myelin. Compound **13** decreased the loss of myelin versus vehicle, but less so than **11** (**Figure 27**). In contrast, the oligodendrocyte marker, *Olig2*, mRNA was downregulated in the brains of compound **11** treated mice (* $p \leq 0.1$) (**Figure 26**).

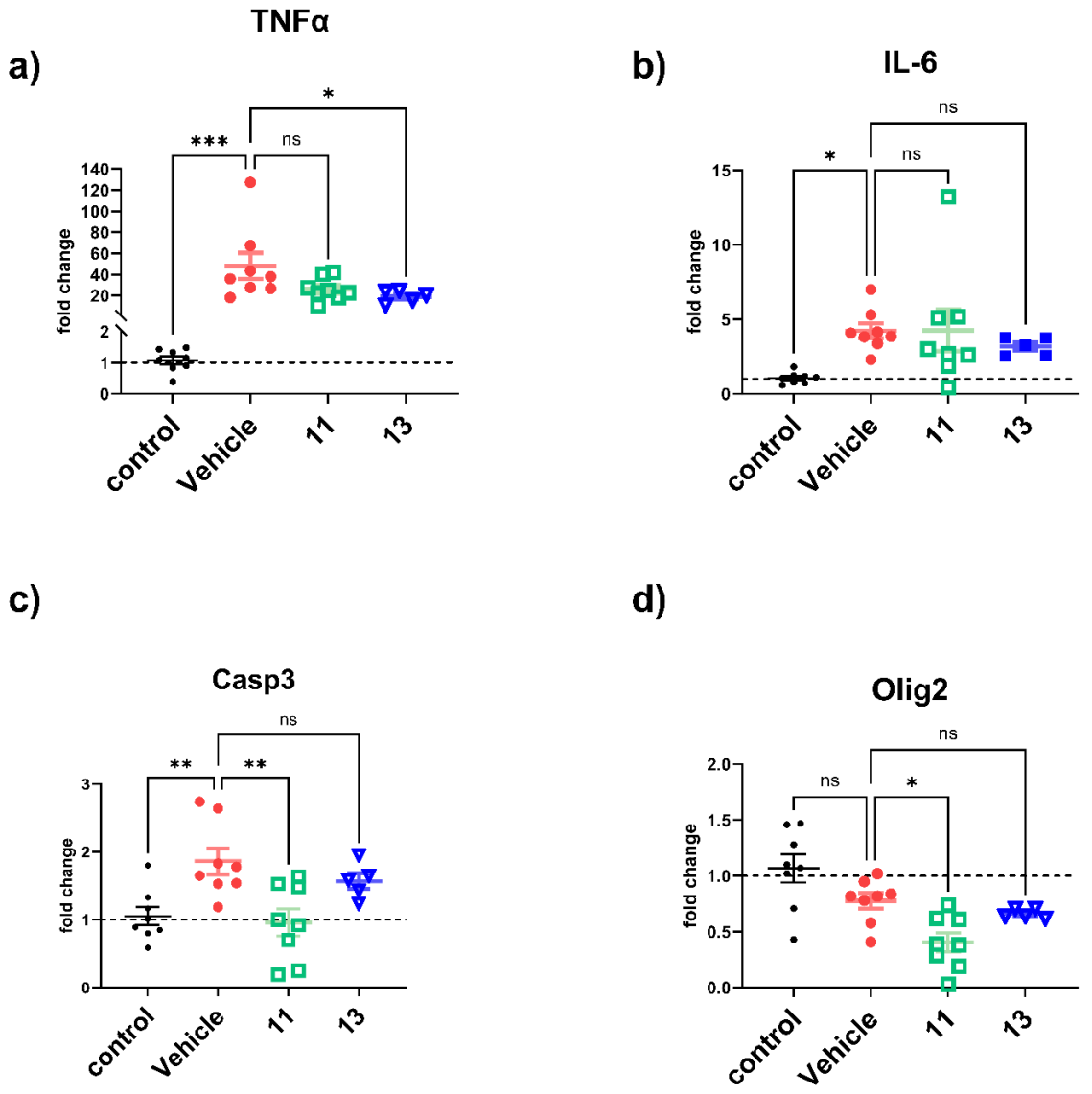

Figure 26. Gene expression analysis of EAE- relevant inflammatory (TNFα and IL-6) (**a-b**), apoptosis (Casp3) (**c**) and oligodendrocytes (Olig2) (**d**) markers in the brain of 14-week-old mice. Plotted are the normalized expression levels as fold change relative to the not-induced control group (circle black shape). * $p < 0.05$; ** $p \leq 0.01$; *** $p \leq 0.001$; **** $p \leq 0.0001$. Data are displayed as mean ± SD of the mean, n = 8. Vehicle results are displayed in red (red circles), compound **11** results are displayed in light green (squares) and compound **13** results are displayed in violet (triangles).

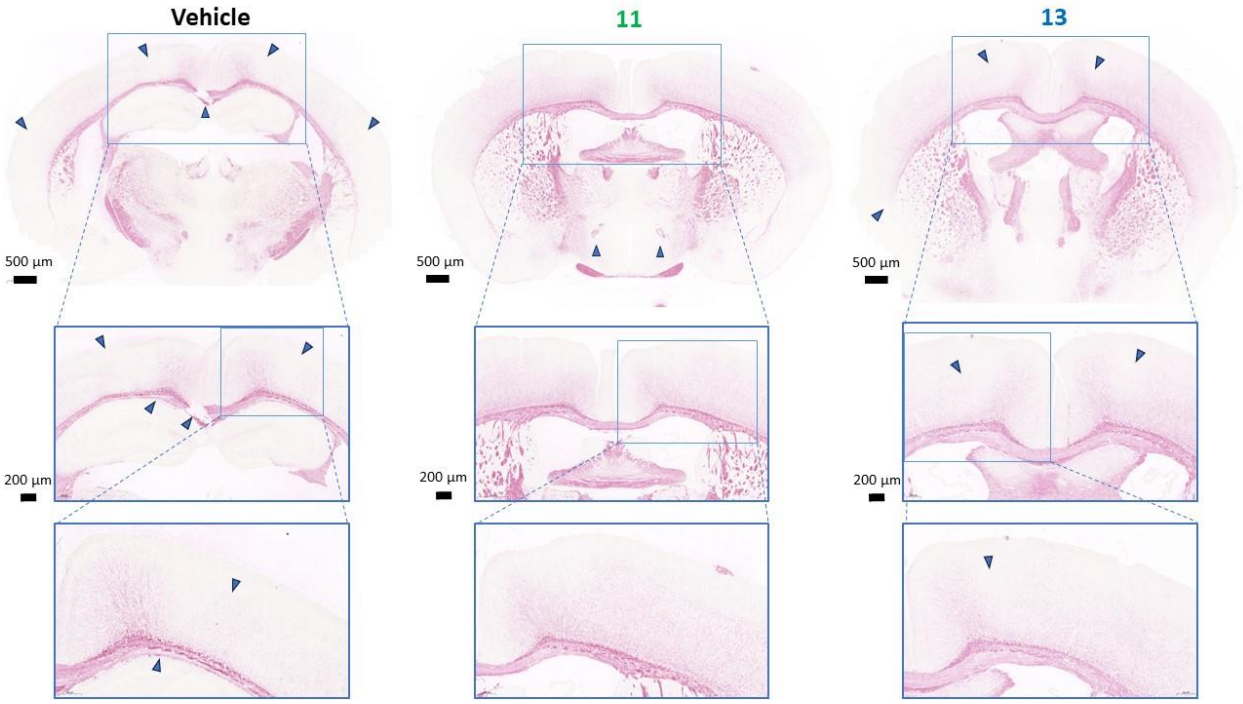

Figure 27. MBP IHC staining of brain coronal sections from EAE MOG_{35-55} induced mice. Myelin fibers (pink stained) loss is indicated by blue arrows in cortex, corpus callosum and anterior commissure, anterior part (aca). Compounds **11** and **13** are compared to the vehicle group.

Both compounds showed up-regulation of myelin marker and down-regulation of apoptosis marker in spinal cord by qPCR and histology

Furthermore, gene expression and histological analysis were performed in spinal cord samples. In the spinal cord, mRNA levels of pro-inflammatory cytokines were not regulated by compound treatment, while the apoptotic marker (*Casp3*) displayed significant down-regulation in treated groups (** $p \leq 0.01$). In addition, the oligodendrocyte marker *Olig2* (oligodendrocytes) was significantly up-regulated in treated mice (** $p \leq 0.01$ and **** $p \leq 0.0001$ respectively for compounds **11** and **13**) (**Figure 28**). These results together indicate that both p38 MAP Kinase inhibitors have neuroprotective activity in the spinal cord. As already done for the brain samples, in order to evaluate myelin loss in the spinal cord, an MBP IHC assay was performed. Stained in pink, myelin is severely disrupted in vehicle mice compared to compound **11** treated mice, which instead showed myelin protection. Also in this analysis, as already shown in the brain, compound **13** protected against the loss of the myelin versus vehicle, but was less effective than compound **11** (**Figure 29**).

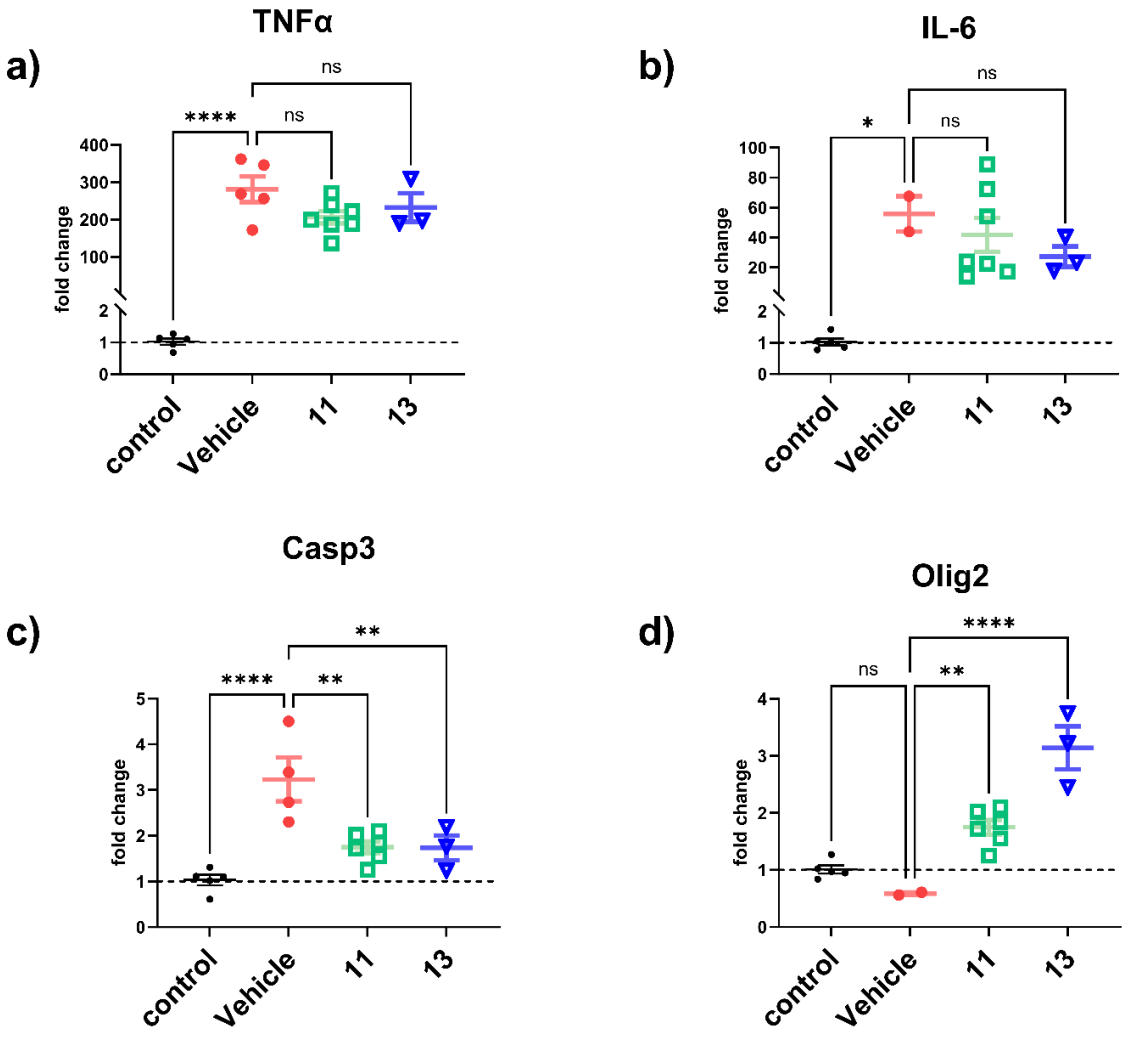

Figure 28. Gene expression analysis of EAE- relevant inflammatory (TNFα and IL-6) (**a-b**), apoptosis (Casp3) (**c**) and oligodendrocytes (Olig2) (**d**) markers in the spinal cord of 14-week-old mice. Plotted are the normalized expression levels as fold change relative to the not-induced control group (black circles). * $p \leq 0.05$; ** $p \leq 0.01$; *** $p \leq 0.001$; **** $p \leq 0.0001$. Data are displayed as mean ± SD of the mean, n = 8. Vehicle results are displayed in red (circles), compound **11** results are displayed in light green (squares) and compound **13** results are displayed in violet (triangles).

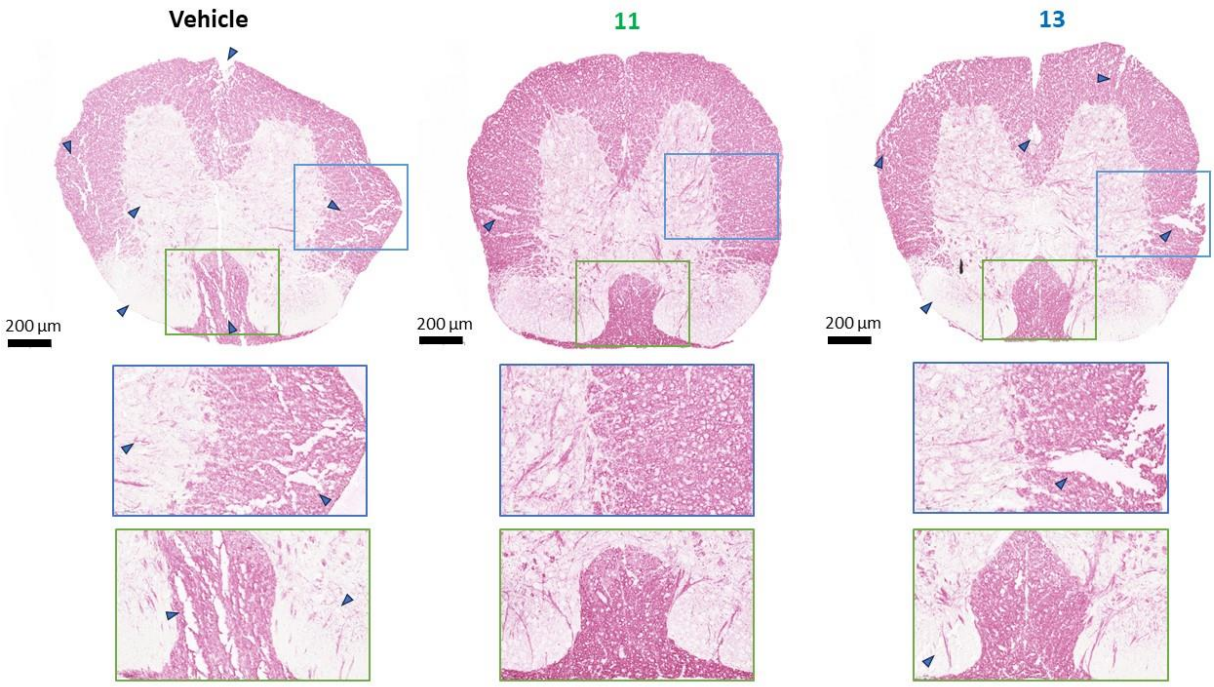

Figure 29. MBP IHC staining of spinal cord sections from EAE MOG_{35-55} induced mice. Myelin fibers (pink stained) loss is indicated by blue arrows in gray matter (blue rectangle), white matter (blue rectangle) and dorsal funiculus (green rectangle). Compounds **11** and **13** are compared with the vehicle group.

Both compounds showed liver necrosis protection and reduction of inflammation by qPCR and histology

Gene expression analysis in liver samples revealed no compound effect on mRNA levels of the inflammation markers IL17A and IL-6, while TGF-β1 was significantly downregulated in vehicle mice. Dysregulation of TGF-β1 can lead to the development of hepatic fibrosis. [78,79] Due to compound treatment, TGF-β1 expression levels were restored to similar levels to those in healthy mice. Furthermore, expression levels of the anti-inflammatory and liver protective cytokine IL-10 were analyzed. A significant downregulation of IL-10 was observed in EAE mice and in compound **13** treated mice, whereas compound **11** treated mice displayed no significant changes in liver IL-10 levels compared to healthy mice (**Figure 30e**). It has been shown that IL-10 attenuates liver fibrosis and possesses liver protective properties.[80] Upregulation of the fructose transporter Glut5 and increased dietary fructose intake is associated with non-alcoholic fatty liver disease (NAFLD).[81] Significantly upregulated Glut5 expression levels were detected in vehicle treated EAE mice. Both compounds **11** and **13** restored Glut5 expression to the levels in healthy mice (**Figure 30e**).

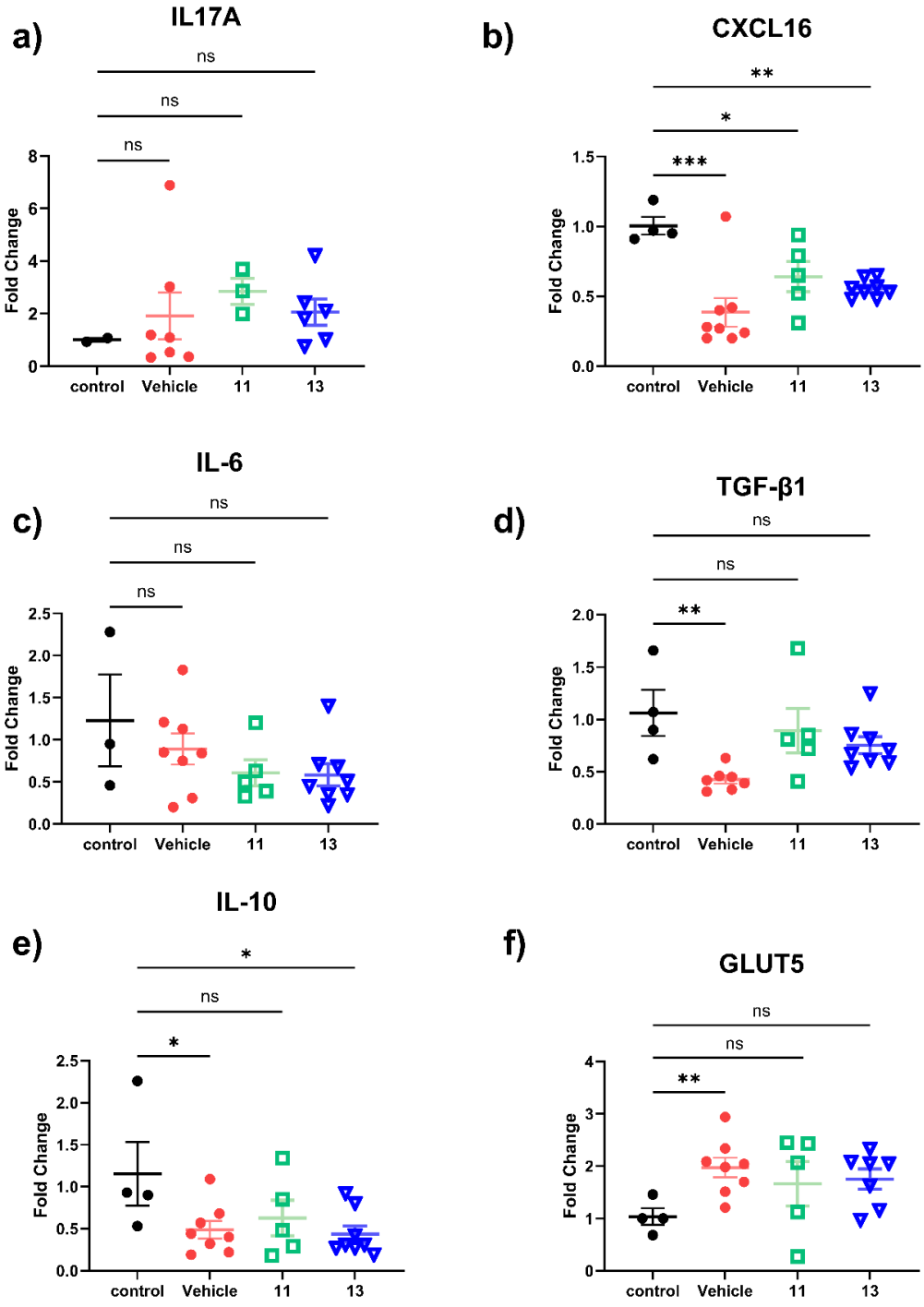

Figure 30. Gene expression analysis of EAE-relevant fibrosis/necrosis (IL17A, CXCL16) (**a** and **b**), inflammatory (IL-6, TGF-β1 and IL-10) (**c, d** and **e**) and metabolic (GLUT5) (**f**) markers in the liver of 14-week-old mice. Plotted are the normalized expression levels as fold change relative to not-induced control group (black circles). * $p < 0.05$; ** $p \leq 0.01$; *** $p \leq 0.001$; **** $p \leq 0.0001$. Data are displayed as mean ± SD of the mean, n = 8. Vehicle results are displayed in red (circles),

compound **11** results are displayed in light green (squares) and compound **13** results are displayed in violet (triangles).

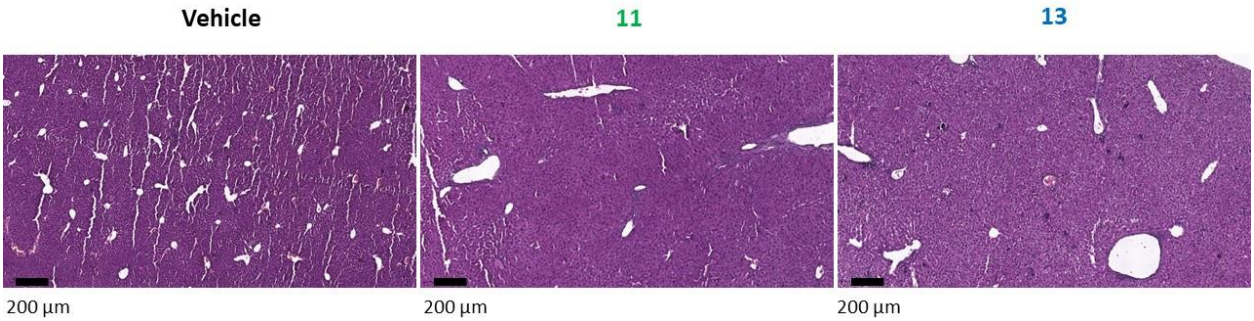

Figure 31. Representative H&E-stained liver tissues from 14-week-old EAE MOG_{35-55} induced mice. Vehicle treated liver shows severe inflammation and macroscopic morphological damage, scale bar 200 µm. Both compounds **11** and **13** treated livers appear to have less liver damage and preservation of normal hepatic histology, scale bar 200 µm.

3.4 Discussion

The p38 MAP Kinase signaling pathway has been identified as a central regulator in the pathophysiology of MS and its most commonly used murine model, EAE.[13,82] MS progression, characterized by demyelination, immune dysregulation, and neuroinflammation, is linked to oligodendrocyte destruction and glial overactivation. It has already been demonstrated that inhibition of p38 MAP Kinase signaling pathways can promote neuroprotection and neurotrophic effects against the clinical-pathological presentation of MS and influence other neurological disorders such as AD.[83]

Given this rationale, in the first chapter of this thesis, out of the 13 Skepinone-like p38 MAP Kinase inhibitors tested, the two most potent *in vitro* and *in vivo* compounds were selected: compound **11** that showed no BBB penetrating ability, and compound **13** which distributes in both the brain and spinal cord of C57/BL6 mice after p.o. and i.v. administration. In order to test the compound potential therapeutic effect on MOG/CFA induced mice, in the second chapter of this thesis the already existing EAE murine model was modified aiming to establish a more stable and reproducible model, with high incidence and low group variability. This murine model allowed me to test compounds **11** and **13**, underlying the potential of targeting p38 MAP Kinase pathway as a disease-modifying therapy in MS. p38 MAP Kinase inhibitors have already shown potential in preclinical studies using EAE models by modulating the immune response, reducing inflammation, and protecting against demyelination in the CNS, but their failure in clinical trials for MS patients has been attributed to several factors such as lack of efficacy and side effects in the liver.[82]

Here I have tested two p38α MAP Kinase inhibitors with different profiles and organ affinity in order to evaluate their therapeutical potential in treating EAE induced mice. My hypothesis was that by inhibiting the two concomitant inflammatory events occurring in CNS and in the periphery representing the crucial elements sustaining MS and EAE, it would be able to attenuate the severity of the symptoms occurring in the disease. To test this hypothesis, 24 C57/BL6 female mice (pre-fed with AIN 93M diet for 6 weeks) were induced with MOG/CFA sonicated emulsion and therapeutically treated only after the first symptoms were scored. In this project, the effects of compound **11** and **13** versus vehicle treated animals was compared, while all groups were later compared to the not-induced mice. Furthermore, with the aim to investigate probable side effects that other p38 MAP Kinase inhibitors showed during clinical trial tests, were also examined possible hepatic toxicity.

The *in vivo* results confirmed the analytic data were showed in **Chapter 1** of this thesis: compound **11** resulted in being not BBB penetrant, while compound **13** was found in the brain and spinal cord (60 ± 25.7 nM and 112 ± 28.2 nM, respectively). Both compounds were detected by LC-MS in the periphery in liver and spleen: while compound **11** was detected at an average concentration of 364 nM and 250 nM respectively, compound **13** had a poor affinity for these two organs (**Figure 24b**). Furthermore, while body weight did not differ between groups until the end of the study (**Figure 25a**), compound **11** displayed survival protection (87.5 % survival) versus vehicle animals' (25 % survival) and decreased symptom severity (from extremely severe in the vehicle group to mild-moderate severity with compound **11** treatment) (**Figures 25b** and **c**). These results indicate that a peripheral inhibition of the immune response leads to a therapeutical effect in terms of both severity and survival and that, by inhibiting p38 MAP Kinase activity, the disease signs appeared less severe due to the reduction of the production of pro-inflammatory cytokines and a consequent damp of the immune response. Histology and qPCR analysis on brain and spinal cord demonstrate that both compounds have a beneficial effect on the CNS, with myelin preservation and downregulation of apoptosis markers (**Figures 26** – **29**). This result is reflecting what has already been published by Noubade *et. al*. showing that by the regulation of p38 MAP Kinase activity specifically in T cells is sufficient to modulate EAE severity.[84] Furthermore, *Casp3* (apoptosis marker) was found significantly downregulated in both brain and spinal cord of treated animals in comparison with vehicle group. This data indicates that, as already demonstrated by Xing *et. al*., p38α MAP Kinase inhibition provides neuroprotection by reducing inflammation and preventing damage to the myelin sheath and neurons.[85]

Moreover, my investigations on liver toxicity displayed by histological findings, that the macroscopic structure of livers treated with both compounds is maintained healthy, while vehicle animals displayed severe liver damage (**Figure 31**). Furthermore, analysis on liver by qPCR confirmed that compound **11** might be protective against liver fibrosis (**Figure 30**). These findings suggest that, while old generation of p38 MAP Kinase inhibitors have

been poorly tolerated in the clinic, eliciting side effects such as liver toxicity,[86] the selected high potent and selective p38α MAP Kinase inhibitors are not hepatotoxic and may even be beneficial to overall liver performance in MS patient.

In this study it was demonstrate that peripheral inhibition of p38 MAP Kinase slows the development of EAE, and can increase survival and lower the severity of the signs. Taken together, these results show that p38α MAP Kinase inhibition treatment with the peripherally active selected compound leads to neuronal and liver protection ameliorating EAE disease symptoms and increasing animal survival.

3.5 Conclusions

Compound **11**, the peripherally active p38α MAP Kinase inhibitor, increased *in vivo* survival by over 50 % in EAE CFA/MOG induced mouse models versus vehicle treated animals, resulting also in a decrease of the severity of the symptoms recorded. In addition, histological and qPCR analysis results showed that spinal cords and brains benefited from the anti-inflammatory effect of the drugs, displaying neuroprotection by myelin fiber preservation and a decrease of apoptotic factors.

In contrast to the failure of others p38 MAP Kinase inhibitors in clinical trials for MS patients attributed to side effects in the liver, both compounds **11** and **13** showed liver toxicity protection by histopathological and qPCR analysis indicating great potential beneficial therapeutic effects as drugs against MS.

Chapter 4

P38α MAP Kinase inhibitors restore memory in 12-months-old APP/PS1 mice

Abbreviations:

%, Percentage;

°C, Celsius degree;

AD, Alzheimer's disease;

APOE4, apolipoprotein E;

APP, amyloid precursor protein;

Aβ, beta amyloid;

BBB, Blood-brain-barrier;

CNS, Central nervous system;

CO_2, Carbon dioxide;

DAM, Disease Associated microglia;

FDA, U.S. Food and Drug Administration;

HFD, High fat diet;

i.p., Intra Peritoneal;

IF, immunofluorescence;

Il-18, interleukin 18;

IL1a, interleukin 1a;

IL1β, interleukin 1 beta;

IL-6, Interleukin 6;

LOAD, Late Onset of Alzheimer Disease;

M1, Microglia type 1

M2, Microglia type 2;

MAP Kinase, mitogen-activated protein kinase

MAP, Mitogen-activated protein;

MoA, Mode of Action;

NFTs, neurofibrillary tangles

NOR, Novel Object Recognition;

OF, Open Field,

p.o., Per oral;

PFA, paraformaldehyde

pg, Picogram;

PS-1, presenilin-1;

Rab5, Ras-related Rab protein 5;

RT, room temperature;

sTREM2, soluble TREM2;

TLR-4, Toll like receptor 4;

TNFα, Tumor necrosis factor α;

TREM2, triggering receptor expressed on myeloid cells 2;

WT, Wild type.

4.1 Introduction

Alzheimer's Disease (AD) is an insidious, neurodegenerative disorder of the central nervous system and a major cause of dementia. 50 Mio people worldwide are affected by dementia with an additional 10 Mio new cases reported every year. By 2050, the dementia patient number is projected to rise to 152 Mio, with AD accounting for 60-70 % of dementia cases. The first description of this disease was carried out by Alois Alzheimer at the beginning of the 20th century, defining AD pathogenesis as an extracellular accumulation of amyloid-β (Aβ) peptides generated by the cleavage of amyloid precursor protein (APP), and hyperphosphorylated tau proteins accumulating inside neurons known as neurofibrillary tangles (NFTs) causing neuronal death. In general, the aggregation of Aβ is considered to be an essential trigger in AD pathogenesis that gives rise to NFTs, neuronal dysfunction and dementia.[87]

The FDA has approved five drugs for symptomatic AD-treatment, four acetylcholine esterase inhibitors and one NMDAR-antagonist, however, all of them share limited efficacy and only short-term beneficial treatment effects in AD patients that vary from person to person. So far, all anti-amyloid small molecule drugs in clinical trials have failed, including beta- and gamma-secretase inhibitors. Most anti-amyloid antibodies also failed initially. The exceptions have been Aduhelm (aducanumab), which was only recently very controversially approved by the FDA, and Lecanemab only recently in Phase II.[88,89] Despite historic failure of anti-inflammatory drugs (e.g., NSAIDs) targeting peripheral and neuroinflammation, this kind of investigation is still of prime interest and could support anti-amyloid therapies and other inflammatory-driven pathologies of the CNS.

The interest in central anti-inflammatory drugs is the evidence that pro-inflammatory cytokine levels are increased in both autopsied brains and the peripheral blood of AD patients, with TNFα e.g., correlated to cognitive decline.[90,91] These findings were also reported by Kim *et al.,* 2018, who found elevated plasma cytokine levels of TNFα, IL1α and IL-1β in dementia patients.[92]

Recent advances in immunology revealed that the immune-privilege hypothesis of the CNS is no longer fully valid in that peripheral cells can enter the CNS. In fact, the lymph system is draining cerebrospinal fluid and brain, connecting CNS and periphery and provides constant cross-talk between peripheral and CNS immune systems (**Figure 32**).[93,94] Pro-inflammatory immune cells and cytokines are major players in the progression to chronic inflammation in both the periphery and CNS and are decisive mediators between these inflammatory compartments that are influenced by factors like diet, infection and stress.[95] Master regulators of inflammation, including p38α MAP Kinase, are correlated to both peripheral and CNS inflammation. Thereby, peripheral and central inflammatory events have the potential to interact and self-propel into a vicious cycle, resulting in chronic inflammation. This new insight into the pathogenesis of AD opens discussions about the link to other chronic inflammatory diseases such as diabetes. Among the aging population, diabetes and AD are two highly prevalent diseases and it

has been shown in several studies that they are linked with a significant risk to each other.[96,97,98] Multiple factors which are involved in diabetes pathogenesis and complications are found to also play a role in the development of neurodegeneration in AD patients. The problem of insulin resistance and deficiency is well described and known in diabetes, but there are many studies which suggest dysregulation of insulin levels as a reason behind the development of AD contributing to vessel leakage and BBB disruption.[97,99] Moreover, it has been shown that defects in insulin signaling may lead to the acceleration of AD progression and severity by inhibiting microglia phagocytosis activity against Aβ plaques.[100,101]

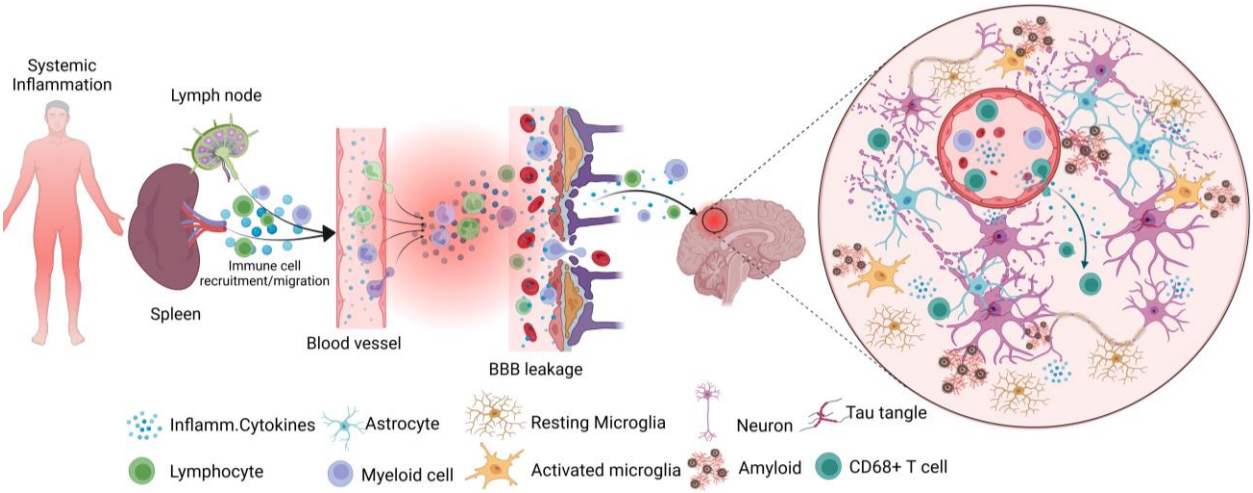

Figure 32. Systemic inflammation, neuroinflammation, and AD-specific pathways. On the left, the systemic inflammation (caused by events such as infection, chronic illness, and sepsis) is marked by increased circulating pro-inflammatory cytokines (e.g., IL-1β, IL-6, TNFα, and IL-18) produced by lymph nodes or the spleen, for example. These cytokines can bind to receptors on endothelial cells and cause a signaling cascade in three ways: **a**) cytokine release into the bloodstream, **b**) opening of tight-junctions between endothelial cells, **c**) and cytokine release into the CNS. Proinflammatory cytokines in the CNS can also activate M0 resting microglia and astrocytes to release more pro-inflammatory cytokines. Prolonged inflammatory activation of M0 microglia and astrocytes is believed to promote neurodegeneration and AD-related pathologies by upregulation of kinases that contribute to tau hyperphosphorylation, β-amyloid oligomerization, the M1 phenotype switch of microglia and p38 MAP Kinase pathway activation[102]. This figure was created with BioRender.

Recent studies demonstrate the potential benefits of novel Skepinone-based p38 MAP Kinase inhibitors. Activity of the p38 MAP Kinase signaling pathway leads to increased pro-inflammatory cytokine levels associated with neuroinflammation and neurodegeneration; this has been documented in both, brains from AD patients and transgenic AD mice.[2,27] The p38 MAP Kinase family consists of 4 different isoforms: MAP Kinase 14 (p38α), MAP Kinase 11 (p38β), MAP Kinase 12 (P38γ) and MAP Kinase 13 (P38δ). The isoforms have different functions and are expressed in different tissues. Peculiarly,

p38α is mostly expressed in immune cells, glia cells and neurons, making it a relevant and valid target for CNS disorders associated with an inflammatory response.[103] Several studies demonstrated how a variety of genes involved in inflammation, such as those coding for TNFα, IL-1β, IL-6, cyclooxygenase-2, and collagenase-1 and -3, are positively regulated by p38α MAP Kinase activation, making p38α MAP Kinase a potential target as a novel therapeutic strategy for chronic inflammatory diseases.

The α and β isoforms of p38 MAP Kinase share 75 % homology. Early generation p38α MAP Kinase inhibitors were active on both α and β isoforms and also were not selective enough with respect to off-targets.[104,105] In addition, the effect of non-selective p38 MAP Kinase inhibition showed in *in vivo* models of inflammation equivocal results. Furthermore, even if early generation p38α MAP Kinase inhibitors had been found to reduce TNFα levels in LPS-induced animal models of inflammation, these effects were not reproducible, even with a potent inhibitor (SB203580).[106]

The more recently described p38 MAP Kinase inhibitor Neflamapimod (**VX 745**), being BBB-penetrant, but with a low brain to plasma ratio and inferior selectivity amongst p38 isoforms, completed Phase II trials for the treatment of AD (NCT02423200, NCT02423122 & NCT03402659). Originally, Neflamapimod was developed for the treatment of Rheumatoid Arthritis, however was discontinued due to side-effects in clinical studies.[18]

Neflamapimod also failed in the improvement of episodic memory in the REVERSE-SD trial, a Phase II trial including 161 mild AD patients.[17,18] Reported adverse-effects included, but were not limited to nausea, headache, diarrhea, and upper respiratory tract infection. On the other hand, it provided positive data in Lewey body dementia. Very little data were published on the dose/PD relationships of the substance. Nor were there descriptions of its effects on microglia in either AD patient brains or in mouse models.

Activated glia cells in the CNS are among the most important contributors to the pathophysiology and progression in AD linked to an excessive or prolonged increase in proinflammatory cytokine production. Microglia contribute to neurodegeneration in AD through the release of toxic substances like cytokines and regulation of synaptic function.[107] Understanding the role of microglia in AD is crucial for developing effective treatments. Microglia can be categorized into two opposite types: pro-inflammatory (M1) or anti-inflammatory (M2) that, in healthy brains, are balanced (**Figure 33a**).[108] While M1 microglia induce inflammation they also have diminished ability to phagocytose amyloid leading to neurotoxicity as Amyloid over saturates receptors like TLR4. M2 microglia are considered anti-inflammatory and neuroprotective due to their anti-inflammatory activity and efficacy in phagocytosing amyloid, resulting in clearance (**Figures 34a** and **b**).[109]

Within AD, the formation of Aβ aggregates and NFTs leads to the chronic activation of microglia into the pro-inflammatory M1 phenotype, causing a misbalance between the

M1 and M2 phenotypes that normally occur in the brains of healthy patients. When Aβ peptides are continuously produced, as in AD, pro-inflammatory cytokines produced by activated astrocytes and M1 chronically activated microglia leads to further aggregation of Aβ peptides and a consequent failure in Aβ clearance (**Figure 34**, red rectangle). Ultimately, this chronic activation leads to neurodegeneration and AD pathology.[110] During the progression of AD, the anti-inflammatory M2 microglia, which is functional in its phagocytosis role inducing tissue repair and healing, become over-stimulated and dysfunctional, leading to a loss of the balance in favor of the pro-inflammatory M1 microglia (**Figure 33b**), creating further damage accompanied by cognitive impairment.[111] Previous studies showed that balancing the M1/M2 polarization had a promising therapeutic prospect in neurodegenerative diseases. It has also been demonstrated that shifting microglia from M1 to M2 may be the key to possible therapies for neurodegenerative diseases (**Figure 33b** and **Figure 34**, green rectangle).[108]

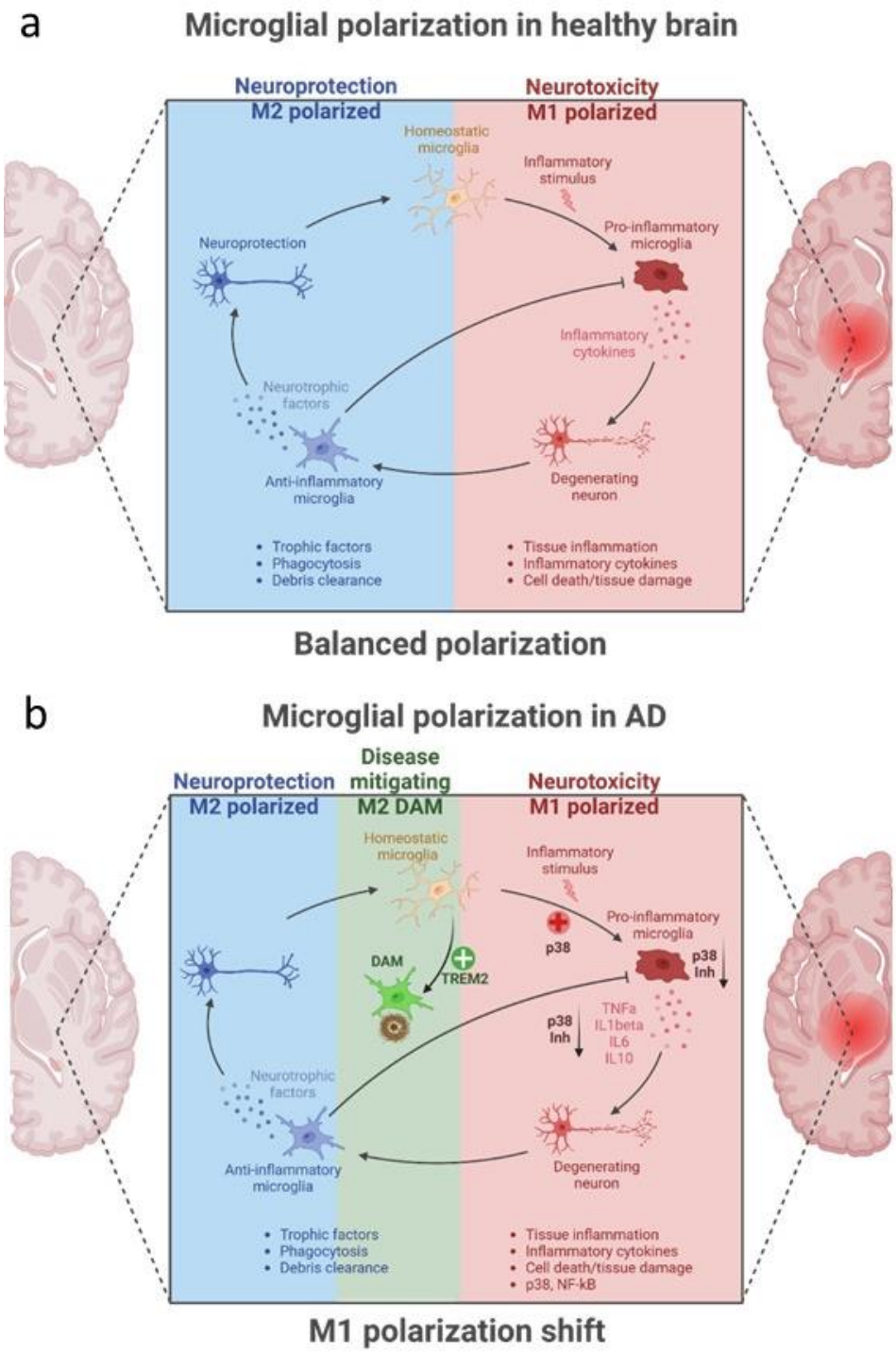

Figure 33. Diagram of the dual role of microglia in neuronal health and disease, underlining the critical balance between the M1 and M2 states. **a**) Balanced microglia polarization in the healthy brain. The diagram shows the dual functions of microglia through M1 and M2 phenotypes. The M1 microglial phenotype promotes neuroinflammation through the secretion of pro-inflammatory factors, leading to neuronal damage. The related pathways involved in this process encompass Toll-like Receptors (TLRs), Nuclear Factor-kappa B (NF-κB), and the p38 MAP Kinase activation pathway. In contrast, the M2 phenotype of microglia secretes anti-inflammatory

factors, thereby providing neuroprotective effects.[109] **b**) Microglial activation in neurodegeneration. The chronic inflammation in the CNS occurring in AD patients leads to a M1 polarization shift. M2 Disease-Associated Microglia (DAM) are found near amyloid plaques trying to compensate for the loss of the balance by mitigating disease progression through phagocytosis of misfolded and aggregated proteins. The switch to DAM is triggered by phagocytosis of apoptotic neurons and depends on the activation of TREM2-APOE signaling.[112] This figure was created with BioRender and adapted from Miao *et. al*.[109]

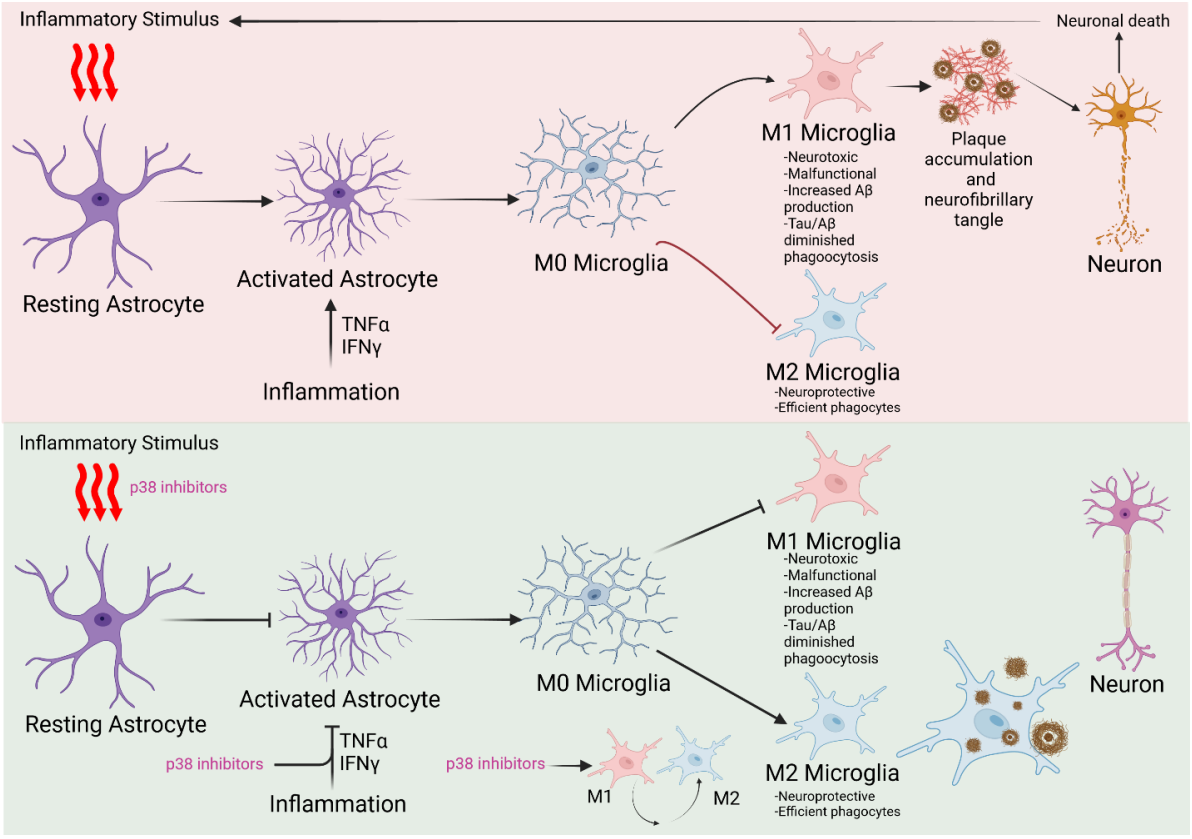

Figure 34. Effect of p38α MAP Kinase inhibition on the chronically inflamed AD brain. On the upper part of the diagram, highlighted in red, the microglia-mediated neuroinflammation, common features in neurodegenerative disease such as AD. The production of pro-inflammatory cytokines (e.g., INFγ and TNFα) leads to a chronic activation of the neurotoxic M1 phenotype of microglia. Below, on the green highlighted diagram, is shown the two different impacts of p38 MAP Kinase inhibitor compounds on the chronic inflammation occurring in the AD brain: **a**) direct inhibition of activated astrocytes inhibiting pro-inflammatory production, **b**) M1 phenotype switches into the M2 neuroprotective phenotype by treatment of p38α MAP Kinase inhibitors. This figure was created with BioRender.

A recently identified subset of CNS resident macrophages found at sites of neurodegeneration, might play such a protective role: the Disease-Associated Microglia (DAM).[113] The microglia phenotype switch to DAM in order to compensate for the loss of

the balance of M1/M2, was found to be triggered by phagocytosis of apoptotic neurons and depends on the activation of TREM2-APOE signaling.[114]

TREM2 is a transmembrane receptor that is predominantly expressed in myeloid cells, including microglia in the brain. Mutations in TREM2 have been associated with an increased risk of developing Late Onset Alzheimer Disease (LOAD) in both the homozygous and heterozygous states.[115,116] TREM2 is a receptor for a range of aggregates and particles including AB, but also ApoE and in both the healthy state and in AD, TREM2 plays a crucial role in regulating microglial activation. Increasing TREM2 expression through overexpression of human TREM2 reduces Aβ deposition, presumably through increased clearance.[117] Agonistic antibodies against TREM2 also reduce Aβ accumulation and improve *in vivo* behavioral performance in AD models.[118,119]

The soluble form of TREM2, sTREM2, has been found to be elevated in the cerebrospinal fluid (CSF) of AD patients making it a useful marker of AD pathology and cognitive decline.[120,121,122,123,124] sTREM2 influences Aβ pathology by blocking and reversing Aβ oligomerization and fibrillization, and preventing Aβ-induced neuronal loss *in vitro*.[125] While this effect appears useful *in vitro*, *in vivo*, the signaling function is probably more important than the engagement amyloid by the soluble receptor binding subunit. This is because although binding may neutralize one particle, the membrane bound signaling form is able to mediate more extensive cellular functions. The origin of the cleaved form of the receptor is likely local proteolysis induced by amyloid driven TLR4 activation.

Several studies showed that Aβ deposition in the brain can activate toll-like receptor 4 (TLR4), normally expressed in microglial membranes. Once triggered, TLR4 activation leads to an intracellular cascade inhibiting the expression of TREM2 and causing its removal from microglial outer membranes via cleavage by the protease ADAM10 and to consequent release of its soluble form sTREM2. While sTREM2 is still able to bind amyloid, it is incapable of signaling an increased clearance reaction. Thus, increased activation of TLR4, further signals via MyD88, p38 MAP Kinase and ADAM10 mediated processes (**Figure 35**) to cause increasing suppression of TREM2 expression and TREM2 function. This is, in turn, a downward spiral of loss of clearance function and anti-inflammatory effects of TREM2.[126,127,128]

These observations suggest that investigating the role of TREM2 in microglial cells is crucial to better understand the molecular mechanisms underlying AD pathogenesis and to developing new therapies that target microglia and TREM2.[129]

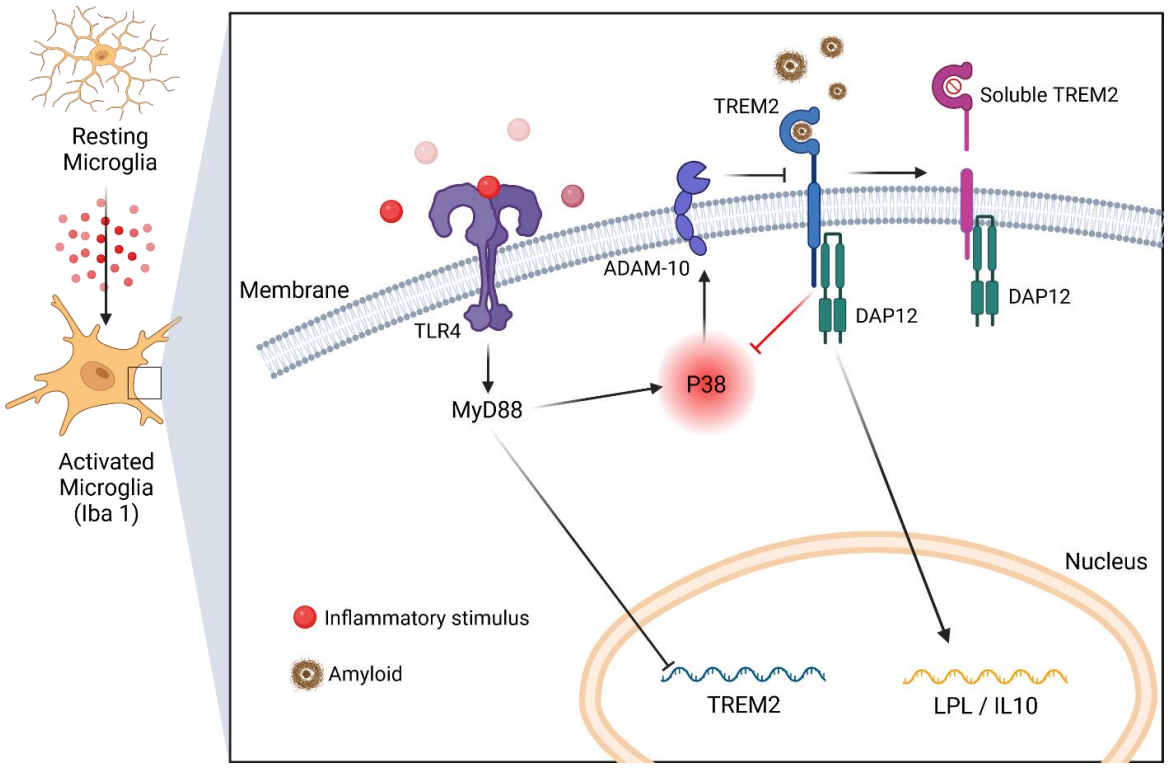

Figure 35. Schematic model of the interplay between triggering receptor expressed on myeloid cells 2 (*TREM2*) and Toll-like receptor 4 (*TLR4*)-induced activation after chronic inflammation typically occurring in the AD brain. This diagram shows my hypothesis on p38α MAP Kinase inhibitors possible MoA. The *TLR4*-induced inflammation suppresses the *TREM2* signaling pathway to exacerbate the Aβ-triggered inflammatory response in microglia. After Aβ exposure, the activated *TLR4* pathway can interfere with *TREM2* by inhibiting the increment of *TREM2* expression and cleaving TREM2 into its soluble form (sTREM2) known to reduce amyloid plaque load and to positively impact amyloid-related pathology. This figure was created with BioRender and adapted from Hu *et. al*.[130]

Also, the dysfunction of endo-lysosomal and autophagic processes play a crucial role in the pathogenesis of AD. After endocytosis, APP-containing vesicles are delivered to early endosomes, marked by Rab5. This general mechanism has been found to occur in microglia, neurons and astrocytes.[131,132,133] Early endosomes serve as a sorting apparatus, regulating the destiny of cargo proteins by the transport to various organelles. The transition from early to late endosomes, marked by the replacement of Rab5 by Rab7 and followed by the fusion with lysosomes, is essential for lysosomal degradation of proteins.[134] The level of extracellular and intracellular APP is believed to induce overactivation of Rab5, which leads to enlarged early endosomes and blocks the conversion of early endosomes to Rab7 positive late endosomes. Consequently, the dysregulation of the endocytic pathway leads to inhibition of the lysosomal degradation of APP, and its unprocessed form is released from the cell via the recycling endosomal pathway, marked by Rab11 (**Figure 36a**, **b** and **c**).[134] Due to its prominent role as a

pathogenic driver in AD, Rab5 has emerged as a major therapeutic target for neurodegenerative disease. The p38α MAP Kinase pathway is the major regulator of Rab5 activity.[7]

For this reason, my hypothesis is that selective p38α kinase inhibitors could reverse the overactivation of Rab5 and restore the transition from early to late endosomes with the subsequent lysosomal degradation of APP (**Figure 36d**).

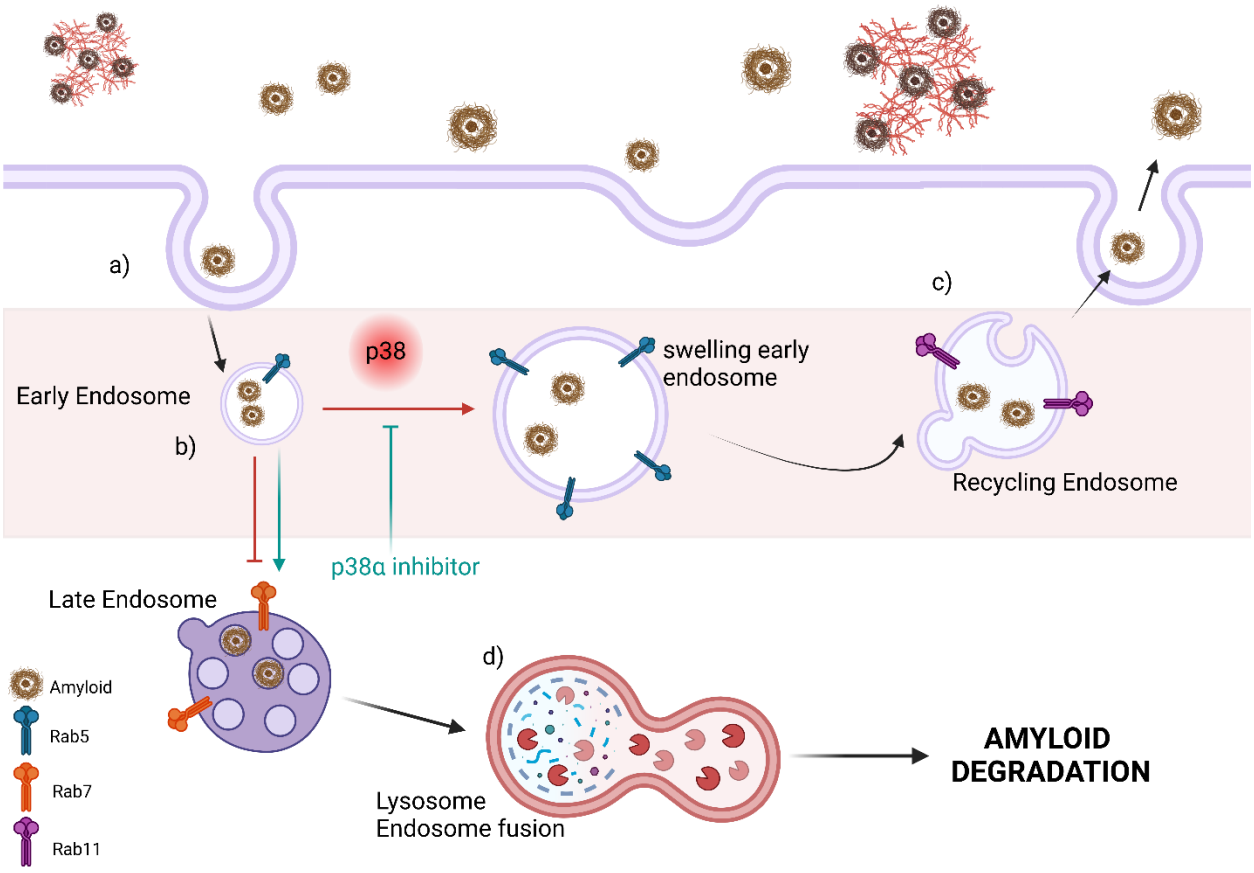

Figure 36. Dysfunction of endosomal-lysosomal protein degradation in AD. **a**) APP endocytosis; **b**) APP induced overactivation of Rab5 leads to swelling of early endosome and inhibits the Rab5 to Rab7 conversion and consequently the transition from early to late endosomes. **c**) unprocessed APP is released from the cell via Rab11 positive endosomes. The Inhibition of p38 downregulates the overactivation of Rab5 and restores the transition from early to late endosomes (**d**) followed by APP degradation in lysosomes. This figure was created with BioRender.

For these investigations I used the well-known and characterized APP/PS1 AD mouse model. The APP/PS1 mouse model is an important research tool used in the study of AD. This mouse model is engineered to express mutant human APP with two familial AD mutations: the human Swedish mutation of APP and the L166P mutation of human presenilin-1 (PS-1) under the murine Thy1 promotor. These mutations lead to increased production and accumulation of Aβ peptides at six weeks of age in the cortex and at 6

months of age in the hippocampus, which are the main sites of amyloid plaques observed in the brains of AD patients.[135]

Researchers use the APP/PS1 mouse strain to study the pathological processes and mechanisms involved in AD and to test potential therapeutic interventions. The presence of amyloid plaques[136] and other Alzheimer's disease-like features in these mice such as gliosis and cognitive impairment (six weeks and seven months respectively),[137] allows scientists to investigate disease progression and evaluate candidate drugs for their efficacy in preventing or reducing/clearing amyloid accumulation.

Aim

My interest in testing p38α MAP Kinase inhibitors was based on the following observations:

- TNFα is proposed to mediate both inflammatory and depressive effects in AD patients and p38α MAP Kinase inhibitors could reduce systemic and CNS TNFα;
- Microglial activation to an anti-inflammatory phenotype could increase clearance of amyloid and p38 is implicated in the inflammatory signaling cascade;
- p38 kinase upregulation is observed in AD brains post-mortem suggesting it is involved in pathology;
- Based on earlier studies in cancer, it is known that p38α inhibition could impact the M1-M2 transition which is also relevant to microglia;
- Finally, **VX 745**, a first generation p38 MAP Kinase inhibitor was reported to be active in amyloidosis.

To be effective, I proposed that the substances should be:

- Highly potent – TNFα IC_{50} in the single digit nanomolar range;
- Unlikely to abrogate anti-inflammatory IL-10 function;
- CNS penetrant;
- Stable *in vivo*;
- Orally available and with no adverse effects on metabolism or liver function;
- Compatible with use in old age, notably, unlikely to worsen common co-morbidities (affective, metabolic, neoplastic);

Compounds **11** (peripherally active) and **13** (BBB-penetrant) fulfilled these requirements as indicated by the data reported earlier. In particular, comparing compounds **11** and **13** allowed me to ask the question; “to what extent is CNS exposure relevant to this mode of action?”

The compounds were tested in two different studies (long and short-term) with APP/PS1 mice, evaluating behavioral tests and histological findings. According to my hypotheses the compounds could act in three different ways:

a) a direct inhibitory effect on the M1 polarized microglia could lead to a polarization-shift towards the M2-TREM2 positive phenotype;

b) the extracellular inhibition of TLR4 could prevent microglial activation of MyD88, leading to intracellular inhibition of p38 MAP Kinase and consequent expression of TREM2 (**Figures 33, 34** green rectangle and **35**);

c) inhibition of Rab5 overactivation by exposure to p38α MAP Kinase inhibitors, could lead to late endosome/lysosome fusion and Aβ degradation by inhibition of the early/swelling endosomal dysfunction and recycling of unprocessed Aβ (**Figure 36**).

In the first long-term study, I focused on prophylactic treatment and preservation of cognitive function over 10.5 months. This also provided information on overall safety and maintenance of effect under long-term treatment (there is potential for counter regulation in p38 mediated signaling). In the second study, I also investigated the efficacy of the compounds with short-term treatment (2 weeks, 12 µmol/kg daily p.o. gavage) in 12-month-old APP/PS1 mice made pre-diabetic with a high-fat diet (DIO-HFD D12492 (I) 60 kJ% fat (Ssniff)) for 4 weeks (a diet in some ways analogous to that used in EAE – fiber). It was also compared the effects of both p38α MAP Kinase compounds against **VX 745** (Neflamapimod), the direct competitor in p38-related AD-therapy.

4.2 Material and Methods

Animals:

Generation and characterization of APP_{751SL}/$PS1_{M146L}$ (APP/PS1) mice has been extensively described.[138,139,140,141,142,143,144,145,146] For both studies, 71 transgenic female and male mice were obtained by crossing heterozygotic Thy1-APP_{751SL} [Swedish (KM670/671NL)] with homozygous $PS1_{M146L}$ mice (originally obtained from Mathias Jucker). Both lines were maintained on a C57BL/6J background. All the mice were housed under constant conditions (12 h light/dark cycle, room temperature 21 ± 1 °C) with water and food available ad libitum.

In the first study, 11 age-matched wild-type (WT) female and male mice of the same genetic background were used in the study as controls (**Table 39**, groups 1 and 2) versus 39 female and male transgenic mice. 1.5-months-old mice were, after being genotyped, included in the project. Soon after, all the mice were fed with maintenance normal chow (**Table 28** of **Chapter 2** of this thesis) mixed with Vehicle (**Table 39**, groups 3 and 4) or

respective compound (**Table 39**, groups 5-8) (see *Food – p.o. Treatment Formulation* subchapter) (**Figure 37**). At 12 months, all the animals were terminated and brains were collected for histological analysis

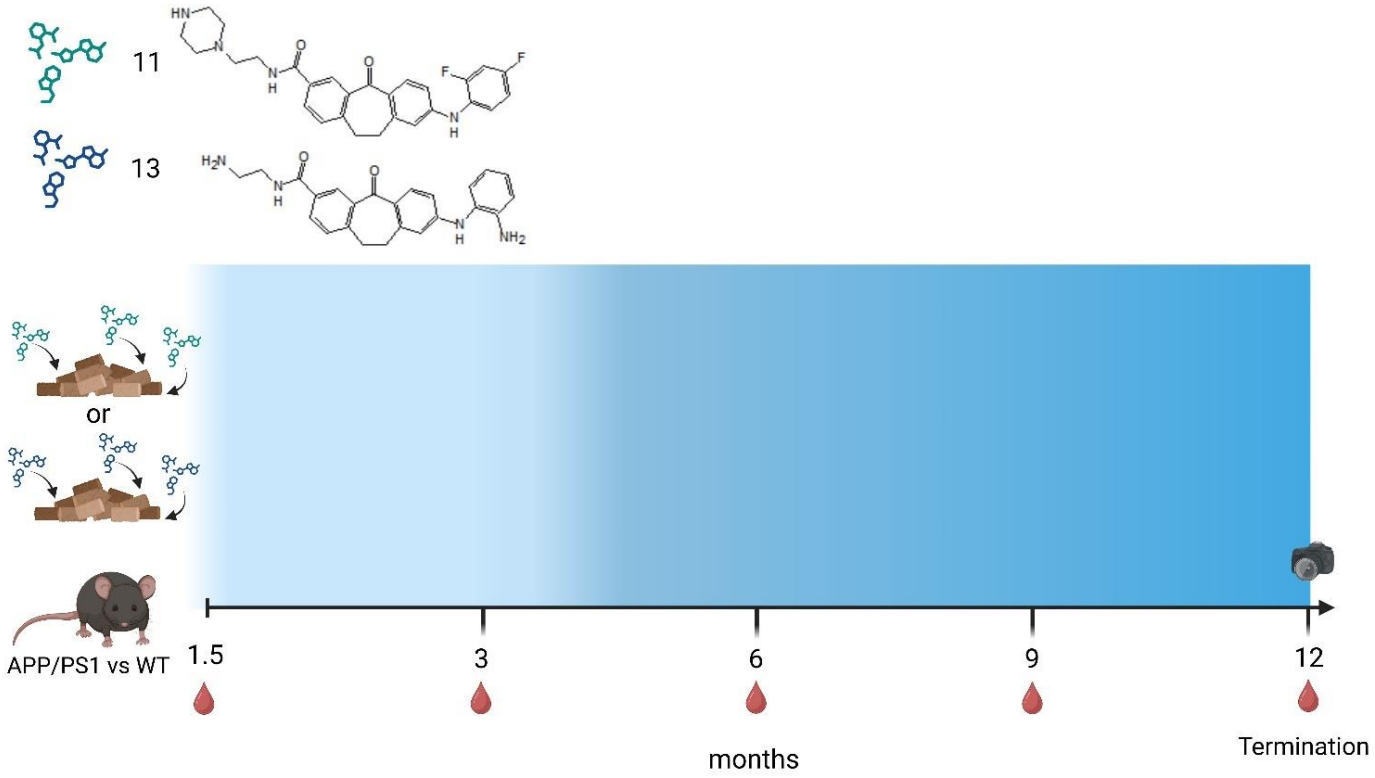

Figure 37. Overview of the first study – long term. 39 1.5-month-old APP/PS1 and 11 WT mice were switched to a chow-p.o. treatment. Baseline of tail blood samples were taken before the first day of treatment (1.5 months), then at 3, 6, 9 and 12 months. Behavioral tests were performed at 12 months (after 10.5 months food – p.o. treatment) (**Figure 35**). This figure was created with BioRender.

Table 39. Experimental groups of study 1 – long term.

Group No.	N	Sex	Genotype	Chow	Treatment	Route	Dose
1	5	Female	WT	Control diet	Vehicle	-	-
2	6	Male	WT	Control diet	Vehicle	-	-
3	5	Female	APP/PS1	Control diet	Vehicle	-	-
4	6	Male	APP/PS1	Control diet	Vehicle	-	-
5	7	Female	APP/PS1	Control diet	11	Food-p.o.	0.3 mg/d/mouse
6	8	Male	APP/PS1	Control diet	11	Food-p.o.	0.3 mg/d/ mouse
7	7	Female	APP/PS1	Control diet	13	Food-p.o.	0.3 mg/d/ mouse
8	8	Male	APP/PS1	Control diet	13	Food-p.o.	0.3 mg/d/ mouse

In the second study, 32 12-months-old APP/PS1 female and male mice, were pre-fed with high-fat diabetic chow (DIO-HFD D12492 (I) 60 kJ% fat (Sniff)) for 4 weeks. Afterwards, mice were daily p.o. treated with 12 µmol/kg of compound **11** (in 10 % DMSO in 10 % PEG/Tween (4:1) mix in water, 5 mL/kg, group 2 **Table 40**), **13** (in 10 % DMSO in 10 % PEG/Tween (4:1) mix in water, 5 mL/kg, group 3 **Table 40**) or **VX 745** (in 10 % DMSO in 10 % PEG/Tween (4:1) mix in water, 5 mL/kg, group 4 **Table 40**) while control animals were treated with Vehicle (10 % DMSO in 10 % PEG/Tween (4:1) mix in water, 5 mL/kg, group 1 **Table 40**) (**Figure 38**). All animals were terminated at week 6 of the study, brains and livers were collected in order to investigate histological results (**Figure 38**).

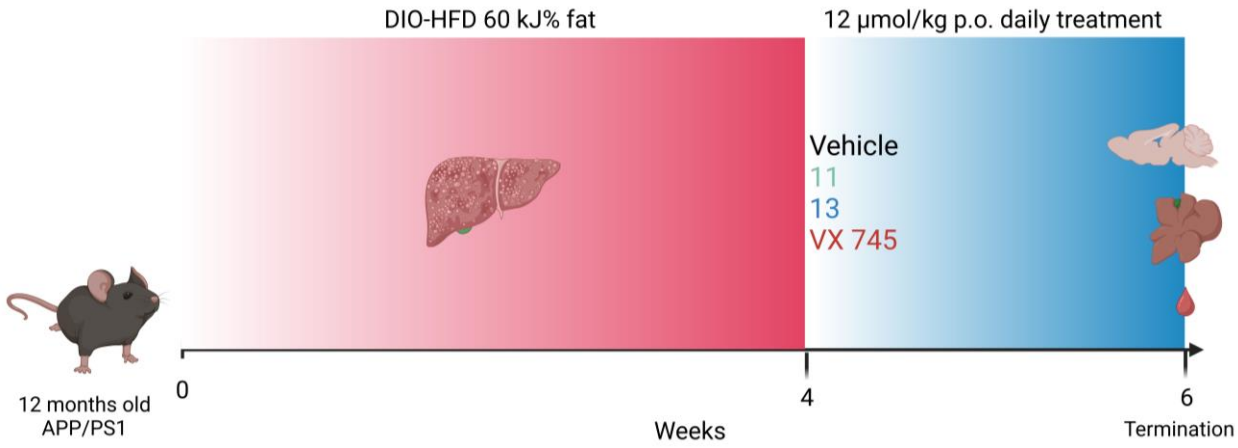

Figure 38. Overview of the second study – short term. 32 12-month-old APP/PS1 mice were pre-fed for four weeks with a HFD treatment to mimic features of diabetes. From four weeks on and for two weeks, mice were treated daily with 12 µmol/kg p.o. (in 0.5 % citric acid, 5 mL/kg) injections with the selected compounds (**11** and **13**), competitor compound (**VX 745** in 10 % DMSO in 10 % PEG/Tween (4:1) mix in water, 5 mL/kg) versus control group (Vehicle, in 0.5 % citric acid, 5 mL/kg). At 6 weeks after the start of this project all the animals were sacrificed in order to evaluate AD pathology. This figure was created with BioRender.

Table 40. Experimental groups of study 2 – short term.

Group No.	N	Sex	Genotype	Chow	Treatment	Route	Dose
1	8	Female	APP/PS1	HFD	Vehicle	p.o.	12 µmol/kg
2	8	Female	APP/PS1	HDF	11	p.o.	12 µmol/kg
3	8	Female	APP/PS1	HFD	13	p.o.	12 µmol/kg
4	8	Female	APP/PS1	HFD	VX 745	p.o.	12 µmol/kg

All animal experiments were performed with the ethical approval from local authorities (Regierungspräsidium Tübingen, approval number SYN 09/20).

Food – p.o. Treatment Formulation:

In the long-term study (first study), mice were daily treated for 10.5 months by food – p.o. chow intake. 100 mg of the respective compounds were mixed with 1 kg maintenance diet after being dissolved in 10 mL volume of tap water (circa 0.3 mg/mice/daily intake). Food powder was placed in a mixer (MUM 4405 Profimixx 44 Kitchenmachine, BOSCH)

and 50 mL tap water was added and the mixer was turned on at speed 2. After the food reached a homogeneous consistency, the respective compounds were added drop by drop while the mixer was running at the same speed. The mixer was left to run for 2 h, until compound and food were homogenously mixed. In the Vehicle groups, only tap water was added, matching the final volume of compound treatment. The food was processed manually and transformed into small pellets before being distributed into the respective cages. This procedure was repeated once every two weeks.

Histology instruments:

Histological preparation of samples was performed using a paraffin dispenser fitted with an MPS/S dispensing module (SLEE Medical), Paraplast Plus (Leica BioSystem, art.-no. X881.1 REF 39602004). An HM325 Manual Microtome (Leica BioSystem) was used to perform 5 µM cuts. Cuts were mounted on glass Superfrost PLUS or Superfrost R (Langenbrinck GmbH, art.-no.03- 0060) slides. Using the same exposure and intensity for each sample, H&E and immunohistochemical images were acquired with 3D HISTECK, panoramic scanner 2.1.1. while immunofluorescent images were acquired with a Keyence BZ-810 fluorescence microscope (Keyence, Tokyo, Japan) using a 20X, 40X and/or 100X/1.45 oil-immersion objective lens. Quantification analysis of the different IHC or IF staining was done with ImageJ software.

Iba1 IHC staining:

This staining was performed on formalin fixed paraffin embedded brain tissue section using a standard protocol. The sections were pre-treated using heat mediated antigen retrieval with sodium citrate buffer (pH6, epitope retrieval) for 45 mins. The sections were then incubated with rat anti-Iba1 primary antibody (ab283346, 1/100 dilution, Iba1 ionized calcium-binding adapter molecule 1, microglial marker) for 2 h at room temperature (RT). The day after, sections were incubated with rabbit anti-rat secondary antibody (Vector Laboratories, BA-4000, 1:400) for 2 h at RT. Subsequently, sections were incubated with the ABC kit solution (ABC Vectastain, Vector Laboratories, Burlingame, CA, USA), and the reaction product was visualized with a blue chromogen (SK-4700, Vector Laboratories). After washing step, sections were mount with Bio Mount HM (BIO-OPTICA Milano).

Amyloid, TREM2 and Iba1 IF staining:

After the deparaffinizing and dehydrating steps using xylene (isomeric mixture, ACROS ORGANICS) and ethanol (VWR Chemicals) dilutions, and water, antigen (epitope) retrieval was carried out in citrate buffer (45 min at 90 C). After washing steps (3 x 5 min in PBS),

blocking was performed with 5 % Normal serum Blocking solution (BioLegend) in 0.3 % Triton X-100 in PBS for 60 min at ambient temperature. Incubation with the primary antibodies was done overnight at 4 °C (Amyloid, TREM2, Iba1). After washing steps (3 x 5 min in PBS), incubation with the secondary antibodies was done for 45 min at ambient temperature (1:400 dilution, dylight-488 horse anti rabbit IgG, Vector Lab, Cat.No. DI-1088-1.5; AlexaFluor-647 donkey anti goat IgG, abcam, Cat.No. ab150135; Cyr3 horse anti mouse IgG, Vector Lab, Cat.No. CY-2300-1). After washing steps (3 x 5 min in PBS), BioMount aqueous mounting glue with DAPI (BIO-OPTICA, 05-1740) was used as counterstain for nuclei. Negative controls were performed using only the secondary antibody incubation step.

Open Field activity:

The open field (OF) task is a means for assessing depression/anxiety-like behavior in response to a novel environment. Distance traveled is a measure of ambulatory movement, while time immobile detected is a measure of depression. Also, the amount of time spent in the center zone versus the peripheral zone is used as a measure of anxiety levels due to the rodent's natural thigmotaxis behavior when frightened (i.e. avoiding open areas where a predator may be present).[147] In this study, 12-months-old WT and APP/PS1 mice were placed in an empty cage (60 cm long × 30 cm wide) and their activity was recorded using ANY-maze 7.2 video tracking software (Stoelting Europe, Dublin D14 A6P3- Ireland). The four central quadrants (highlighted in blue) are collectively referred to as the center zone and the 12 peripheral quadrants (highlighted in green) are collectively referred to as the peripheral zone (**Figure 39**). Data were collected continually for 10 minutes: the distance traveled (m), time spent in the peripheral zone versus the center zone were all automatically recorded by the software. 5 % acetic acid was used to clean the cage between each trial.

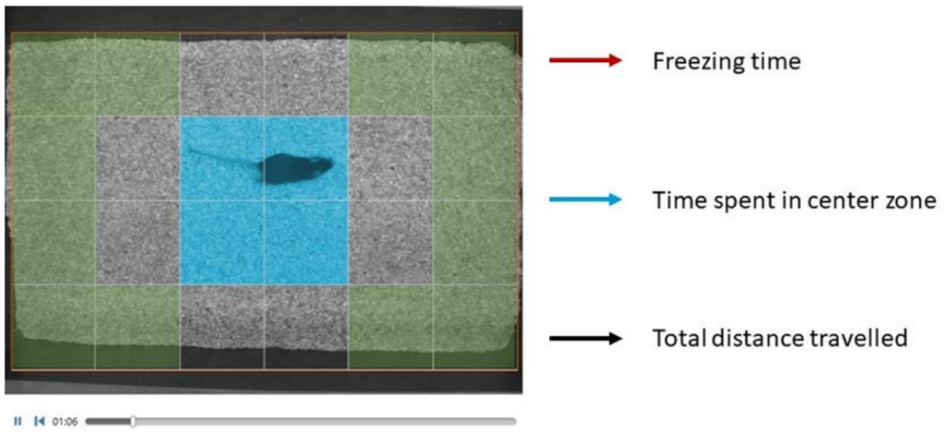

Figure 39. OF behavioral test. The mice are placed in an empty cage and their activity is reordered with a camara by the ANY-maze software. Parameters detected are: freezing time, time spent in center zone and total distance travelled.

Novel object recognition behavioral test (NOR):

Recognition memory and the tendency of mice to explore new objects were evaluated with NOR. NOR is a simple, straightforward test that can be easily used as a behavioral test in order to evaluate the therapeutic effects of drugs in the APP/PS1 transgenic AD mouse model.[148] At day 1, habituation phase, each animal was habituated to the testing cage (60 cm x 38 cm x 20 cm) for 10 min (**Figures 39** and **40**). At day 2, training phase, each animal was allowed to explore two identical objects (identical in shape, color and material) placed symmetrically from the arena center for 10 min. At day 3, test phase, one of the familiar objects was replaced with a novel object and again each animal was allowed to explore the two objects (the sample and the novel objects) for 10 min (**Figure 40**).[149] 5 % acetic acid was used to clean the cage between each trial. All experimental data was analyzed using the ANY-maze 7.2 video tracking system (Stoelting Europe, Dublin D14 A6P3- Ireland).

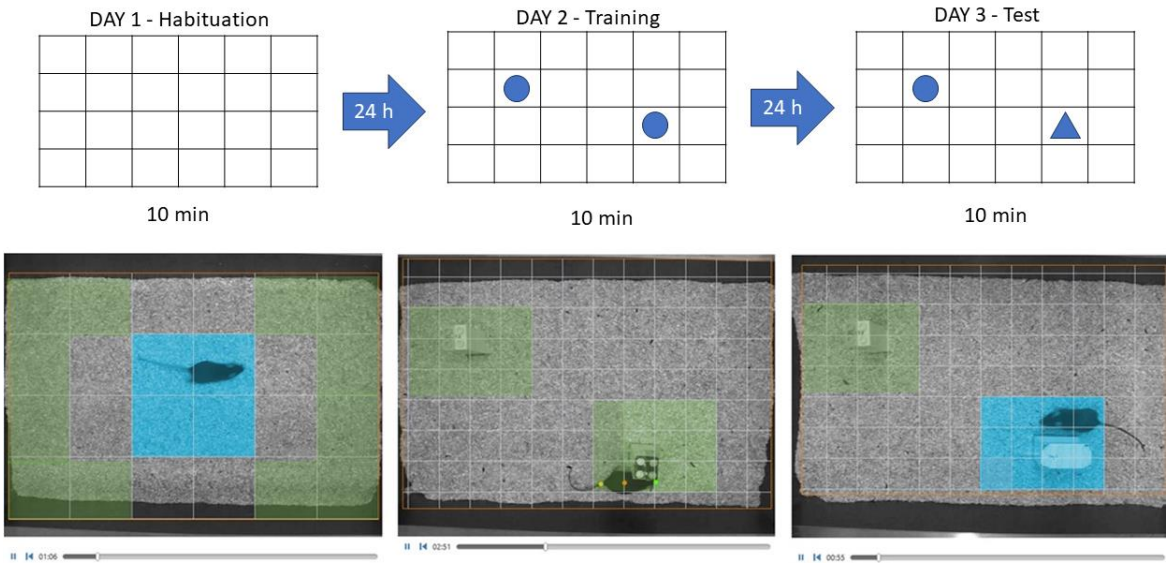

Figure 40. NOR behavioral test. Day 1, habituation phase, is identical to the OF test. At Day 2, training phase, the same mice are introduced to two identical objects (same shape, color and material) and the time spent on the two objects is detected by camera with ANY-MAZE software. At day 3, test phase, the same mice are placed in the cage where one of the two objects differs from the object of the previous day by having a different shape (novel object). The time spent on object 1 versus object 2 is detected by camera with ANY-MAZE software.

Statistics:

Statistical analysis and preparation of graphs were done using GraphPad Prism 9.3.1. All experimental results were tested for normal distribution using the Shapiro-Wilk test. Before conducting further statistical analysis, the Brown-Forsythe test was used to test data for homoscedasticity while ordinary one-way ANOVA was used for multiple comparisons (Bonferroni correction). Two-way ANOVA was used to test differences in behavioral and histological data, p-values were corrected with the Bonferroni method for multiple comparisons. Significance levels are indicated by * $p < 0.05$; ** $p \leq 0.01$; *** $p \leq 0.001$; **** $p \leq 0.0001$.

4.3 Results

Both compounds showed an anti-anxiolytic and anti-depressive effect on 12-months-old APP/PS1 mice

Anxiety signs are observed in dementia patients and the same pathological symptoms were observed in the APP/PS1 mouse model.[150] In the long-term study, the Open Field (OF) behavioral test was performed after 10.5 months daily food – p.o. treatment, on 12-month-old APP/PS1 mice treated and non-treated versus non-treated WT age-matched mice with the same genetic background. The OF test can assess movement and anxiety/depression-like behavior. Activity results were taken on animals that, at the end of study, showed from 35 to 45 % increase on weight. No real difference was detected between the different groups. The amount of time spent in the center zone is a reflection of anxiety while the distance travelled and time immobile are indicators for depression, toxic effects or general animal activity and performance. Each mouse was placed in an empty cage (60 cm x 38 cm x 20 cm) and allowed to freely explore it for 10 min. The mouse behavior was recorded with a video camera and different parameters were analyzed with ANY-maze software: distance travelled, total time immobile and time spent in the center zone. Both treatments led to increased movement and a decrease of total immobile time, if compared to APP/PS1 vehicle group animals (**Figure 41)** (* $p < 0.05$). This suggests that they contribute to the maintenance of a normal degree of activity and potentially ameliorate depressive aspects of amyloidosis. Both compounds also increased the time spent in the center zone in comparison to the control APP/PS1 group (**Figure 42**, * $p < 0.05$ for compound **11** and *** $p \leq 0.001$ for compound **13**) suggesting alleviation of the anxiety. The animals could have focused their mobility on the edges of their cage environment, however, by being more mobile and present in the central zone, they appear to be also less anxious. Time in the central zone is not necessarily a simple correlate of increased mobility and this is reflected in the differences in the compounds and the fact that some animals were notably more present in the central zone.

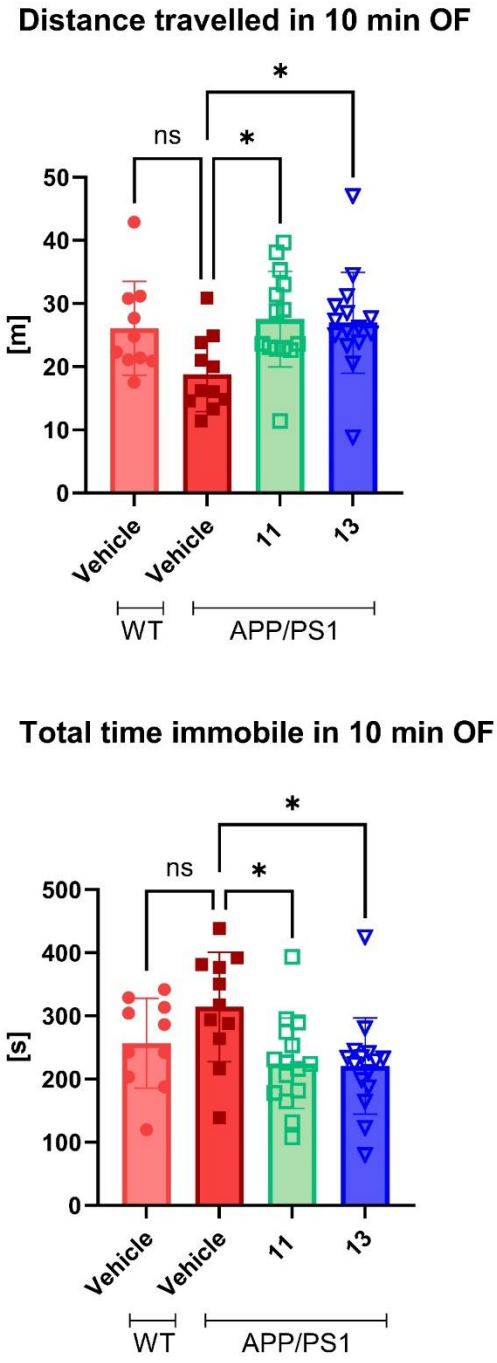

Figure 41. Distance travelled (m) and total time immobile (s) detected per each 12-month-old mouse by ANY-maze software. In comparison: WT Vehicle group (n=10, light red, full circle shape), APP/PS1 Vehicle group (n=11, dark red, full square shape), APP/PS1 compound **11** treated mice (n=15, green, empty square shape) and APP/PS1 compound **13** treated mice (n=15, blue, empty triangle shape). Values are displayed as mean ± SD. * $p < 0.05$; ** $p \leq 0.01$; *** $p \leq 0.001$; **** $p \leq 0.0001$.

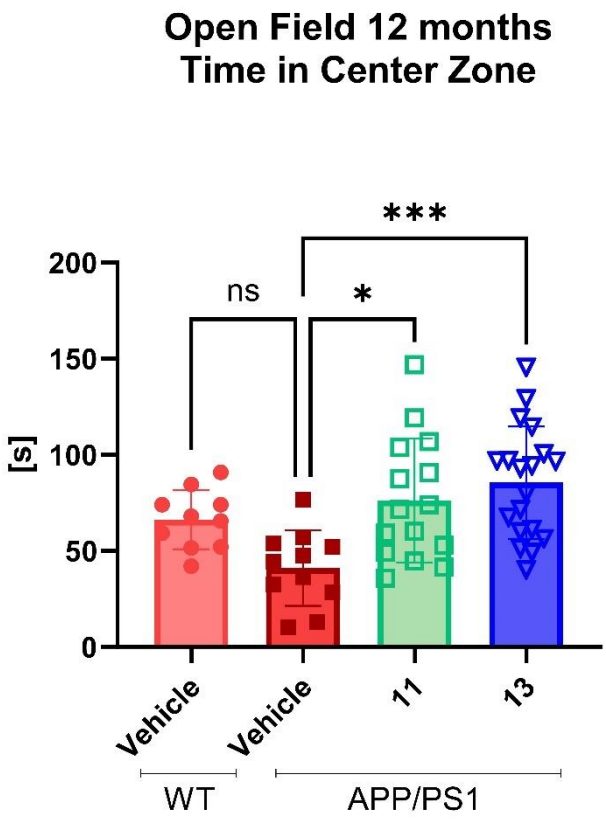

Figure 42. Time in the center zone (s) detected per each 12-month-old mouse by ANY-maze software. In comparison: WT Vehicle group (n=10, light red, full circle shape), APP/PS1 Vehicle group (n=11, dark red, full square shape), APP/PS1 compound **11** treated mice (n=15, green, empty square shape) and APP/PS1 compound **13** treated mice (n=15, green, empty triangle shape). Values are displayed as mean ± SD. * $p < 0.05$; ** $p \leq 0.01$; *** $p \leq 0.001$; **** $p \leq 0.0001$.

Both compounds showed memory restoration in 12-month-old APP/PS1 mice

In the long-term study, the inhibitory effects of p38α MAP Kinase on Aβ-induced neuronal damage, including memory impairment, have been further examined the Novel Object Recognition (NOR) behavioral test. Raw data (time each animal spent next to the single objects) were recorded over 10 min by a video camara and analyzed by ANY-maze software (**Figure 43a** and **b**). The ratio is defined by the time the animal spent exploring the novel object (day 3, test phase) versus the same object presented to it the day before (day 2, training phase) (**Figure 43c**). While the APP/PS1 vehicle mice showed a significant decline in recognition memory, both treatment groups displayed restoration of memory to the level of WT non-treated animals (**Figure 43c**, * $p \leq 0.05$).

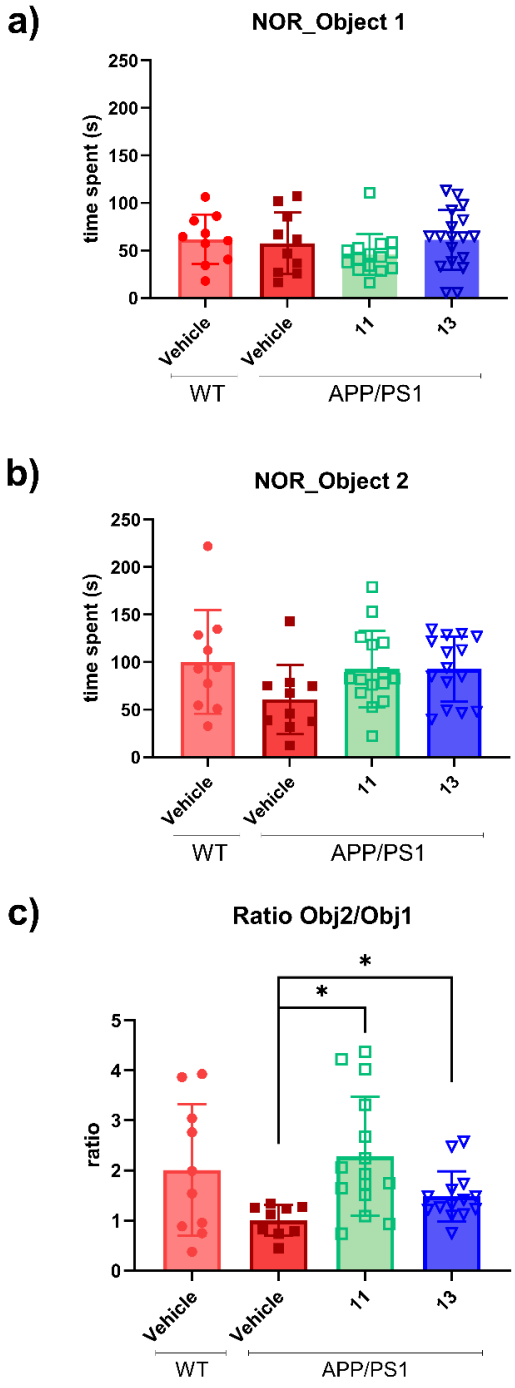

Figure 43. NOR test shows short-term memory maintenance in 12-month-old APP/PS1 mice treatment groups. **a**) raw data day 2 (training phase) showing time spent by each animal investigating the two identical objects in the cage. **b**) raw data day 3 (test phase) showing time spent by each animal investigating the novel object in the cage. **c**) Ratio defined by the formula: *the novel object/the known object exploration*. In comparison: WT Vehicle group (n=10, light red, full circle shape), APP/PS1 Vehicle group (n=11, dark red, full square shape), APP/PS1 compound **11** treated mice (n=15, green, empty square shape) and APP/PS1 compound **13** treated mice (n=15, blue, empty triangle shape). Values are displayed as mean ± SD. * $p < 0.05$; ** $p \leq 0.01$; *** $p \leq 0.001$; **** $p \leq 0.0001$.

Both compounds mediated amyloid plaque disaggregation

The observation that treatment with compounds **11** and **13** could reverse learning and memory deficits led me to further examine possible correlations with the Aβ plaque deposition. As a next step, it was investigated whether Aβ deposits, one of the hallmarks of AD, were altered with the p38 MAP Kinase inhibitor compound treatments in the long-term study with 12-month-old APP/PS1 mice. In **Figure 44a** a representative image of IF-amyloid-staining is shown for each animal group (in blue are stained nuclei (DAPI), in green are stained Aβ plaques). Notably, the Aβ deposit positive area was decreased in the cortex of p38α MAP Kinase inhibitor-treated APP/PS1 mice (**Figure 44a**). KEYENCE inverted fluorescence microscope BX-Z810 was used to digitalize the stained sections. 20X magnification images (**Figure 44a**) and brain sagittal sections were used for all quantitative analysis. Amyloid positive fraction stained with antibody (green channel) were quantified by ImageJ software (**Figure 44b**). Folded organ sections were excluded from analysis because they led to false positive results. As shown in the quantitative analysis, both compounds **11** and **13** statistically significantly decreased the amount of Aβ deposits if compared to the 12 months APP/PS1 vehicle group animals (~ 65 and 75 % respectively, **** $p \leq 0.0001$).

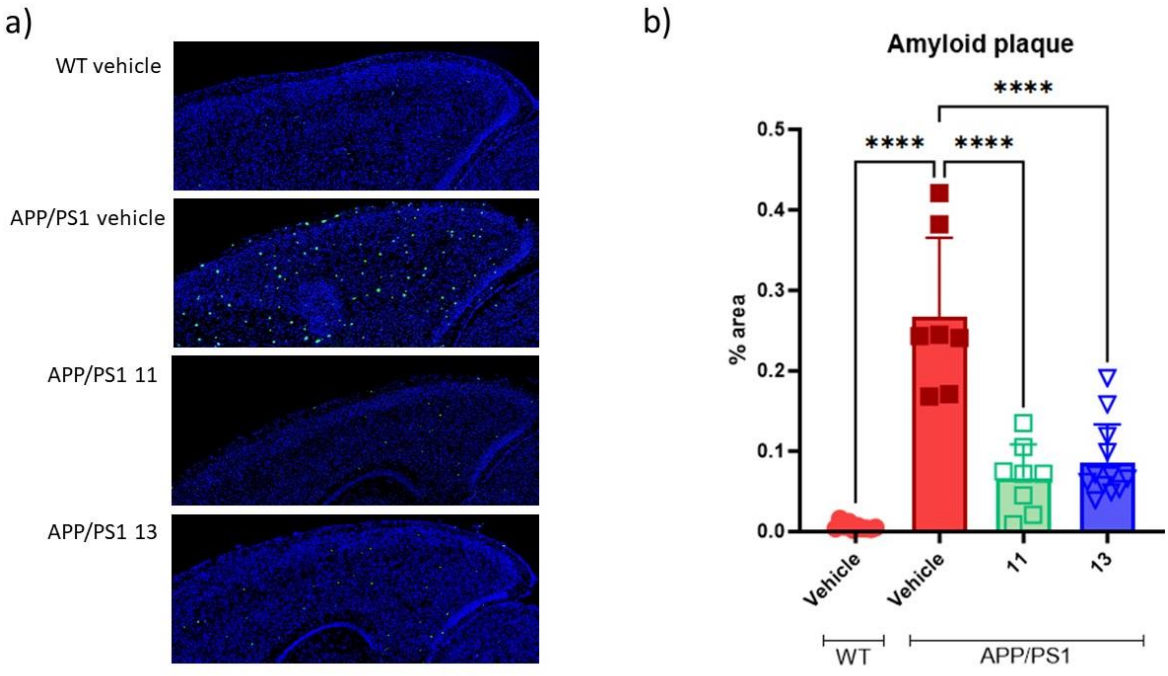

Figure 44. Amyloid-β plaque reduction in 12-month-old APP/PS1 p38 MAP Kinase inhibitor-treated mice (long-term study, 10.5 months p.o. daily treatment). **a**) Representative IF microscope images of mouse cortex sagittal brain sections (one section per mouse) stained with Amyloid-β

antibody. **b**) Aβ-positive areas were quantified by ImageJ software. In comparison: WT Vehicle group (n=10, light red, full circle shape), APP/PS1 Vehicle group (n=7, dark red, full square shape), APP/PS1 compound **11** treated mice (n=8, green, empty square shape) and APP/PS1 compound **13** treated mice (n=14, blue, empty triangle shape). Values are displayed as mean ± SD. * $p < 0.05$; ** $p \leq 0.01$; *** $p \leq 0.001$; **** $p \leq 0.0001$.

Both compounds showed microglial activation

In the long-term study, in order to investigate the inhibitory effects of p38α MAP Kinase on microglia activation and consequently on Aβ clearance/phagocytosis, sagittal sections of 12 APP/PS1 non-treated and treated mice versus non-treated WT age-matched mice were stained with IHC for Iba1. Immunohistochemical images were acquired with 3D HISTECK, panoramic scanner 2.1.1. at 40X and 100X magnification (**Figure 45a**). Brains were used for quantitative analysis and the microglia positive fraction stained with Iba1 antibody (black) were analyzed by ImageJ software (**Figure 45b**). Folded organ sections were excluded from analysis because they led to false positive results. The quantification showed that both compounds had a regulatory effect on microglial activation. While the APP/PS1 vehicle group mice results were not statistically different versus WT non-treated group, compounds **11** and **13** displayed a statistically relevant difference in the activation of the microglial brain population (**Figure 44b**, *** $p \leq 0.001$ and ** $p \leq 0.01$, respectively).

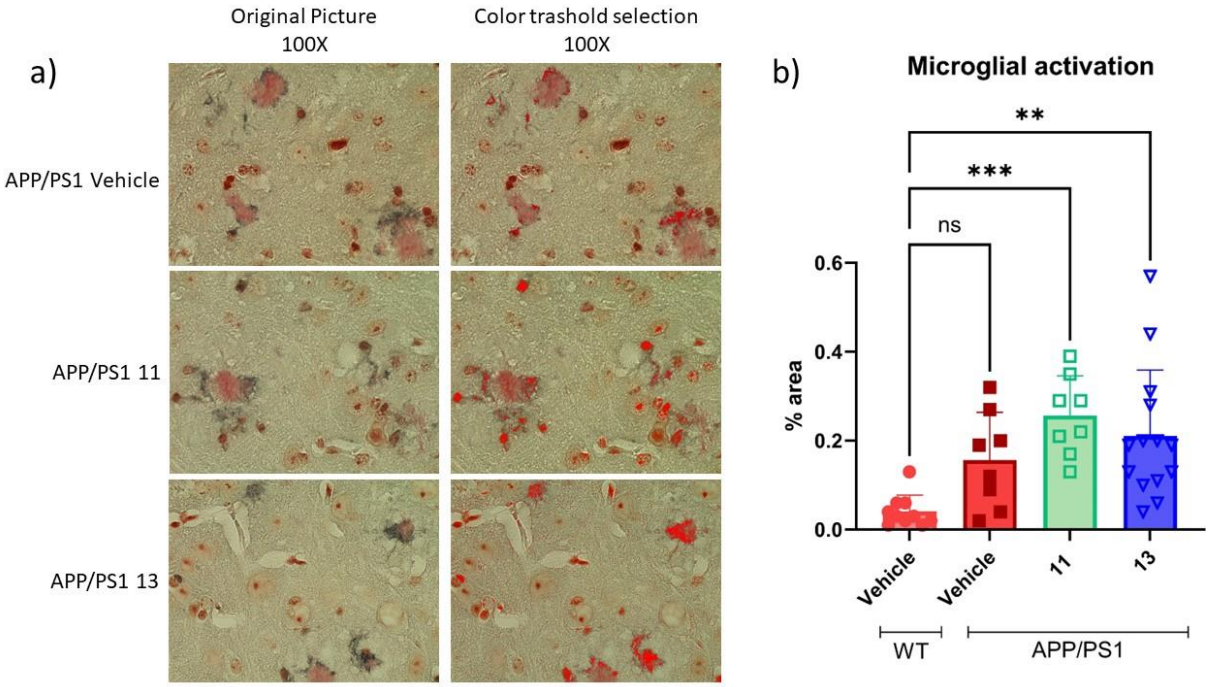

Figure 45. Activation of microglia in APP/PS1 12-month-old brain. **a**) Immunohistochemical staining of sagittal mouse brain sections showed prominent microgliosis as assessed by the microglial marker Iba1 versus Congo Red contra-staining showing Aβ plaques. On the left are the original pictures, and shown on the right is after a threshold was selected to underline in red the black Iba1 positive staining. 100X magnification. **b**) Percentage of Iba1 positive area on sagittal mouse brain sections indicating microglia activation. In comparison: WT Vehicle group (n=10, light red, full circle shape), APP/PS1 Vehicle group (n=9, dark red, full square shape), APP/PS1 compound **11** treated mice (n=8, green, empty square shape) and APP/PS1 compound **13** treated mice (n=14, blue, empty triangle shape). Values are displayed as mean ± SD. * $p < 0.05$; ** $p \leq 0.01$; *** $p \leq 0.001$; **** $p \leq 0.0001$.

Both compounds showed TREM2 up-regulation

The loss-of-function or mutant variants of TREM2 increase the risk of developing AD, while TREM2 activation also showed a significant negative correlation with disease progression.[151] In the long-term study, triple immunofluorescence staining was performed to determine the cellular expression and localization of TREM2 after 10.5 months treatment with p38α MAP Kinase inhibitors (**Figure 46**). The results showed that TREM2 positive cells (red channel) were more abundant and apparent cell associated TREM2 was up-regulated after p38α MAP Kinase inhibitor exposure. Also, Iba1/TREM2 double positive microglia cells (yellow and red channel) surrounded Amyloid plaques (green) disaggregating the dense core.

No clear Iba1/TREM2 action was detected in the APP/PS1 vehicle group (**Figure 46b**-**e**). The disaggregating effect also reduced the amyloid plaque size: while in the APP/PS1 compound **11** and **13** treated mice, plaques displayed an average size of 5 to 20 μm respectively, in the APP/PS1 Vehicle group, Aβ plaques reached 50 μm in diameter (**Figure 46b**-**d**).

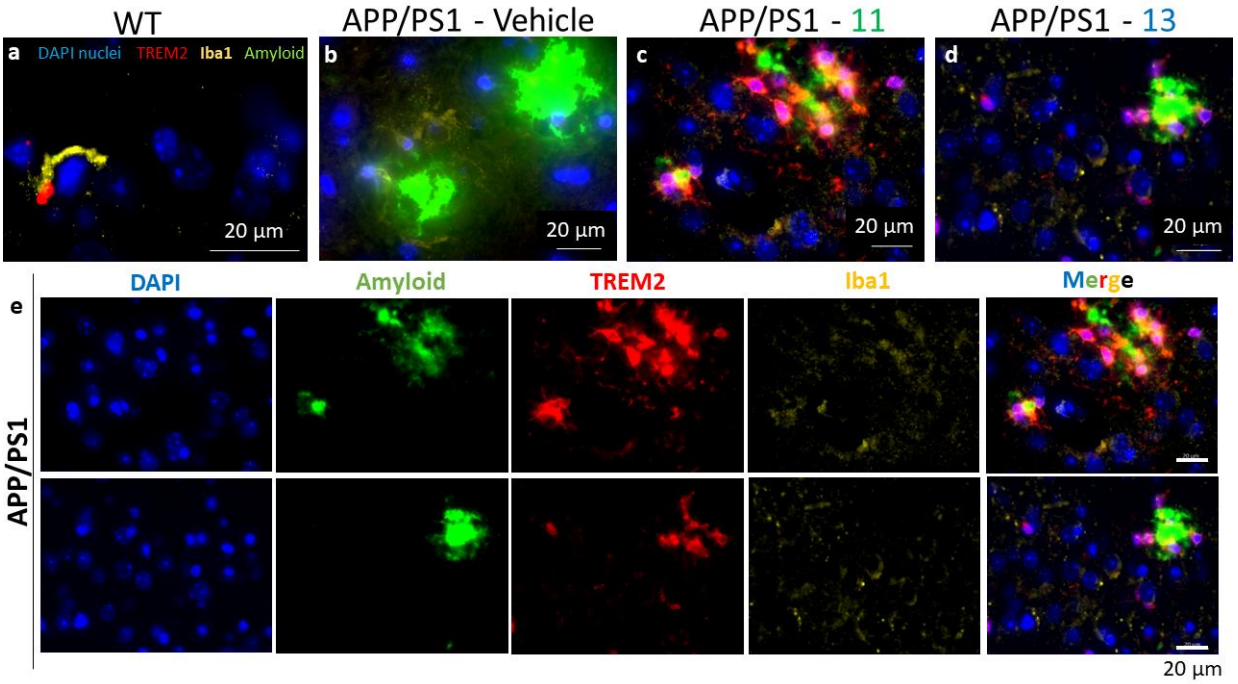

Figure 46. Expression profile of TREM2 positive cells on 12-month-old-APP/PS1 non-treated versus treated mice. **a-d**) Representative images from each group (WT, APP/PS1 vehicle, APP/PS1 compound **11** treated and APP/PS1 compound **13** treated); colocalization of TREM2 (red) with microglia (Iba1, yellow) and amyloid plaques (green) in the cortex area of the brain of 12-month-old APP/PS1 mice. Nuclei were stained with DAPI (blue). Scale bar = 20 µm. **E**) Representative images of the separated channel and the merge of TREM2 (red) with microglia/macrophage (Iba1, yellow) and amyloid plaques (green) from compound **11** and **13** treated mice. Scale bar = 20 µm.

Both compounds showed no Rab5- Aβ colocalization in 12-month-old APP/PS1 mouse brain

One of the earliest manifestations of AD pathology is represented by abnormalities in the endosomal pathway.[152] Therefore, it was examined the morphology and activity of early endosomes in APP/PS1 12-month-old mice after 10.5 months treatment with vehicle, compound **11** or **13**. Immunofluorescent analysis of cortical neurons with an antibody against the early endosomal protein Rab5 revealed that APP/PS1 vehicle mice contained more numerous and atypically large Rab5-positive structures (red channel), while compound **11** and **13** treated mice showed smaller Rab5 vesicle (**Figure 47**). Moreover, to determine whether amyloid and Rab5 were present in the same subcellular compartments, the same brain section was stained with an Aβ antibody (green channel) and investigated whether the two markers resulted in colocalization (yellow signal). As shown in **Figure 47**, APP/PS1 vehicle mice showed colocalization between Rab5 and Aβ (yellow positive signal, merge column) while mice treated with compounds **11** and **13** showed no swelling lysosomes and minimal colocalization.

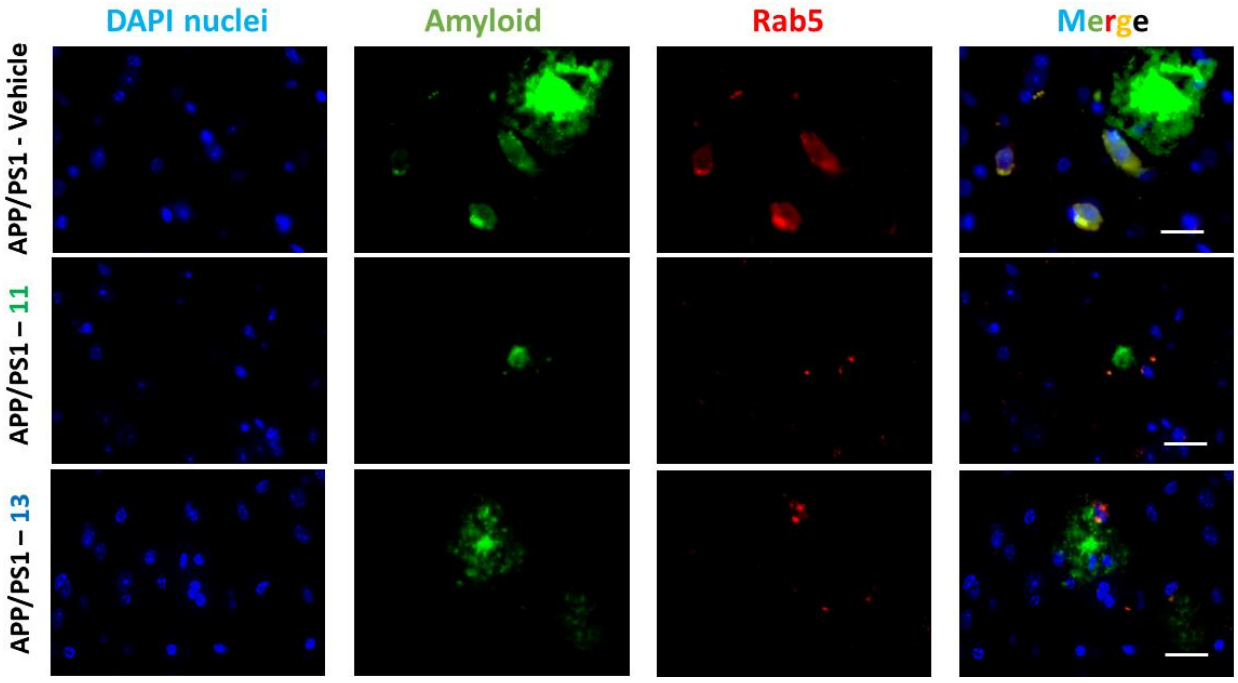

Figure 47. Representative images of Aβ and Rab5 colocalizing in the cortex of APP/PS1 12-month-old mice after 10.5 months treatment with compounds **11** and **13** versus control animals (vehicle). Sagittal brain sections were stained with antibodies against Aβ (green channel) and Rab5 (red channel) while nuclei are stained in blue. The staining reveals enlarged endosomes and an overlap between Aβ and Rab5 in the control brain, while smaller Rab5 vesicle and no colocalization was detected in the mice brains treated with compounds **11** and **13**. Scale bar 30 µm, 100X magnification.

Both compounds showed liver protective activity

Clinical trials with certain p38 MAP Kinase inhibitors were discontinued because of liver toxicity.[86] In both studies, long- and short-term, liver histopathological evaluation was performed in order to investigate compound toxicity. H&E staining on 12-month-old APP/PS1 10.5 months p.o. daily (10 mg/kg daily intake) treated with compounds **11** and **13** showed no macroscopic findings of liver toxicity (**Figure 48**). Vehicle animals showed pale livers compared to the treatment groups, and indication of swollen hepatocytes with rarefied (less compact) cytoplasm which reflects a lower overall cytoplasmic protein content which in turn reduces staining intensity (**Figure 48**). This observation is potentially consistent with afore-observation that this mouse line is also very sensitive to pro-diabetic conditions.

In the short-term study, in order to get diabetic-amyloidosis phenotype mice, 12-month-old APP/PS1 animals were switched to a HFD for 4 weeks. The vehicle group showed

severely steatotic livers, hepatocytes were disorganized, diffuse and enlarged. Fat vacuoles occupied the cytoplasm, compressing cell nuclei to one side (**Figure 49**). The percent of macro-steatosis revealed by the H&E staining is predominant in mostly of hepatic cells in the vehicle group, while compounds **11** and **13** showed a decrease of the severity of the steatosis in the livers (**Figure 49**), where only few of the hepatic cells appeared disarranged. Two weeks daily treatment with the **VX 745** compound showed no amelioration of the severity of the steatosis if compared to the vehicle group (**Figure 49**).

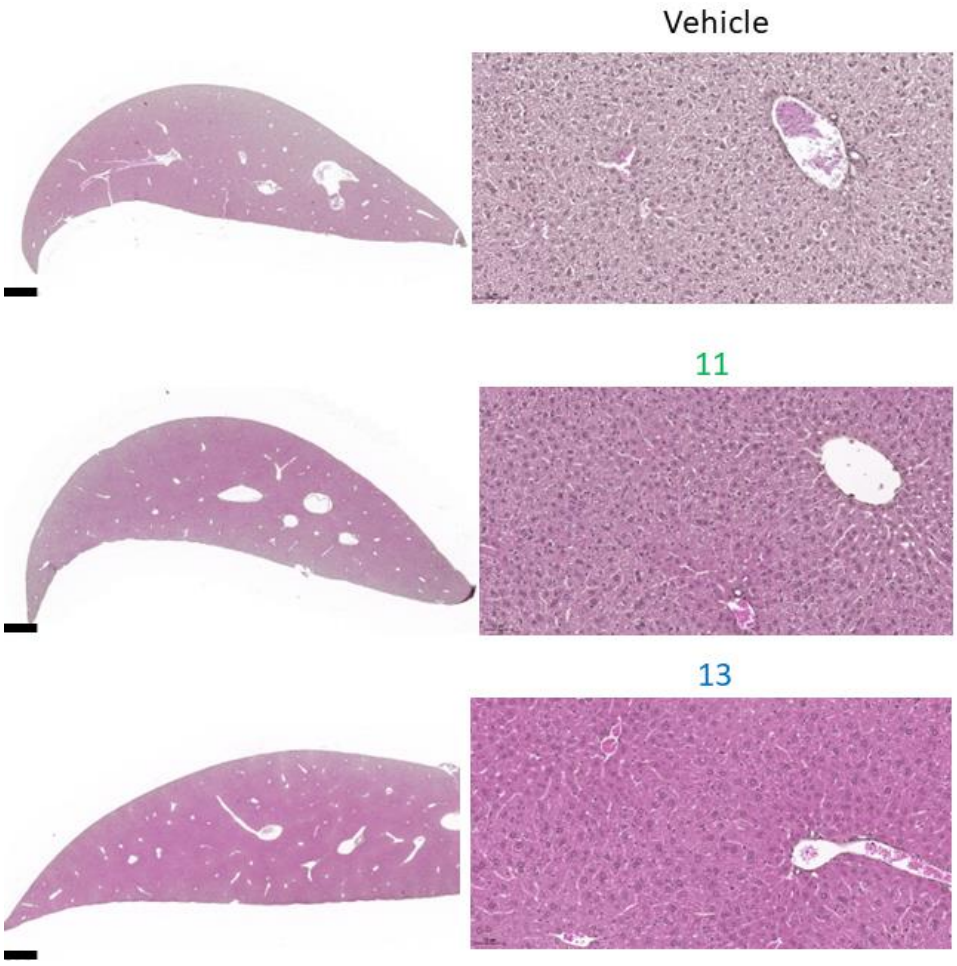

Figure 48. Representative images of histopathological evaluation of mouse liver from the long-term study (10.5 months treatment). H&E stained liver sections from vehicle, compounds **11** and **13** treated APP/PS1 12-month-old mice with 1.7X overview and 20X magnification. No macroscopic tissue damage was observed in any group. Scale bar 500 µm.

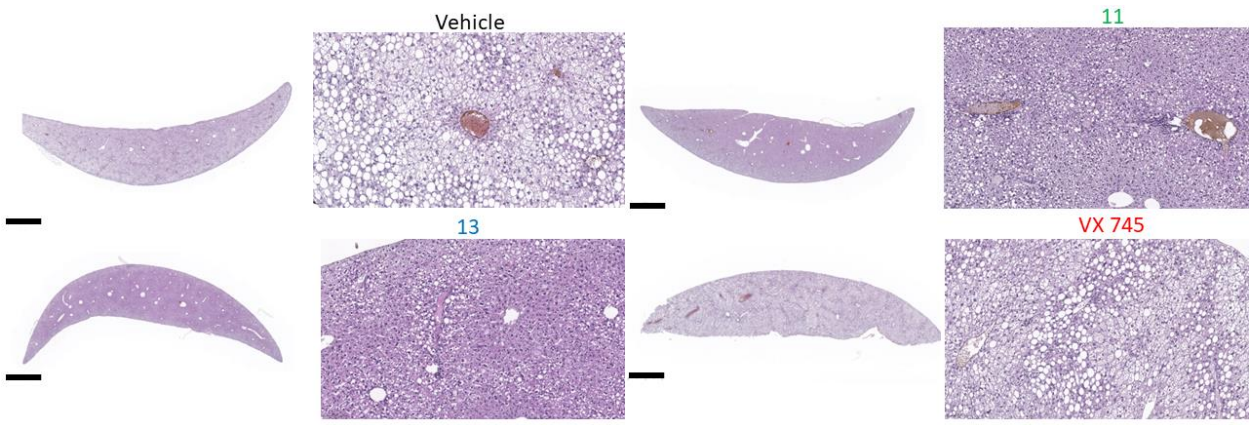

Figure 49. Representative images of histopathological evaluation of mouse liver from the short-term study (2 weeks treatment). H&E stained liver sections from vehicle, compound **11**, **13** and **VX 745** treated APP/PS1 12-month-old mice with 1.7X overview and 20X magnification. Four weeks of HFD induced steatosis in the livers, macroscopically visible in the vehicle and **VX 745** treated mice. Compounds **11** and **13** showed a less severe steatosis. Scale bar 1000 µm.

Both compounds showed amyloid plaque disaggregation activity and size reduction in 12-months-old APP/PS1 mouse brain after two weeks treatment (short-term study)

In order to evaluate the short-term effect of compound **11** and **13** in amyloid plaque reduction in 12-months-old APP/PS1 mice, Aβ IF staining (green channel) was performed in combination with the TREM2 marker (yellow channel). As expected, staining of the vehicle group animals shows the intensive deposition of amyloid plaques in APP/PS1 mice average size of 40-50 µm (**Figure 50a**).

Consistent with the suggestion that p38 MAP Kinase treatment reduces the accumulation of Aβ peptides in the brain, a remarkable reduction in the Aβ-positive staining and average size in both compounds treated groups was detected (**Figure 50b** and **c**). VX 745 treated mice showed no reduction of the Aβ accumulation or of the size of plaques (**Figure 50d**). Also, Trem2-positive cells appeared more activated after exposure to compounds **11** and **13** compared with the vehicle and **VX 745** animals (**Figure 50a-d**).

To better evaluate the amount of the reduction, a quantification was performed on sagittal cuts of each brain by ImageJ software. Compound **11** showed a statistically significant reduction in Aβ deposition of ~ 55 % versus vehicle (*$p < 0.05$), while **VX 745** treated animals showed no significant reduction of the amyloid burden (**Figure 51**). Results were also similar to those in the long-term study with regard to the degree of amyloid removal and the relative potency of the substances. These data also indicate that the degree of reduction of amyloid in 2 weeks was similar to that obtained in long term

treatment. This suggests that the effect is based on a combination of reduce initiation of new plaques formation and a reduction in size of existing plaques.

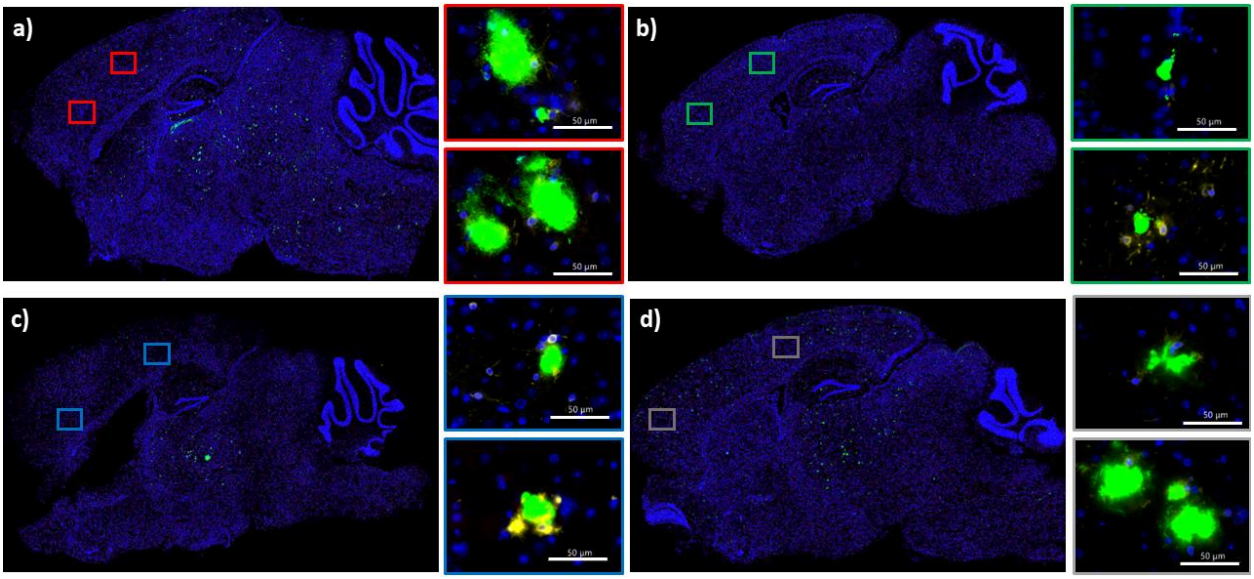

Figure 50. Amyloid-β plaque reduction in 12-month-old APP/PS1 p38α MAP Kinase inhibitor-treated mice (short-term study, 2 weeks treatment). **a**) Vehicle representative IF microscope images of mouse sagittal brain slices stained with Amyloid-β antibody (green channel) and TREM2 (yellow channel) and 100X magnification in the cortex area. **b**) Compound **11** representative IF microscope images of mouse sagittal brain slices stained with Amyloid-β antibody (green channel) and TREM2 (yellow channel) and 100X magnification in the cortex area. **c**) Compound **13** representative IF microscope images of mouse sagittal brain slices stained with Amyloid-β antibody (green channel) and TREM2 (yellow channel) and 100X magnification in the cortex area. **d**) **VX 745** compound representative IF microscope images of mouse sagittal brain slices stained with Amyloid-β antibody (green channel) and TREM2 (yellow channel) and 100X magnification in the cortex area. Scale bar 50 µm.

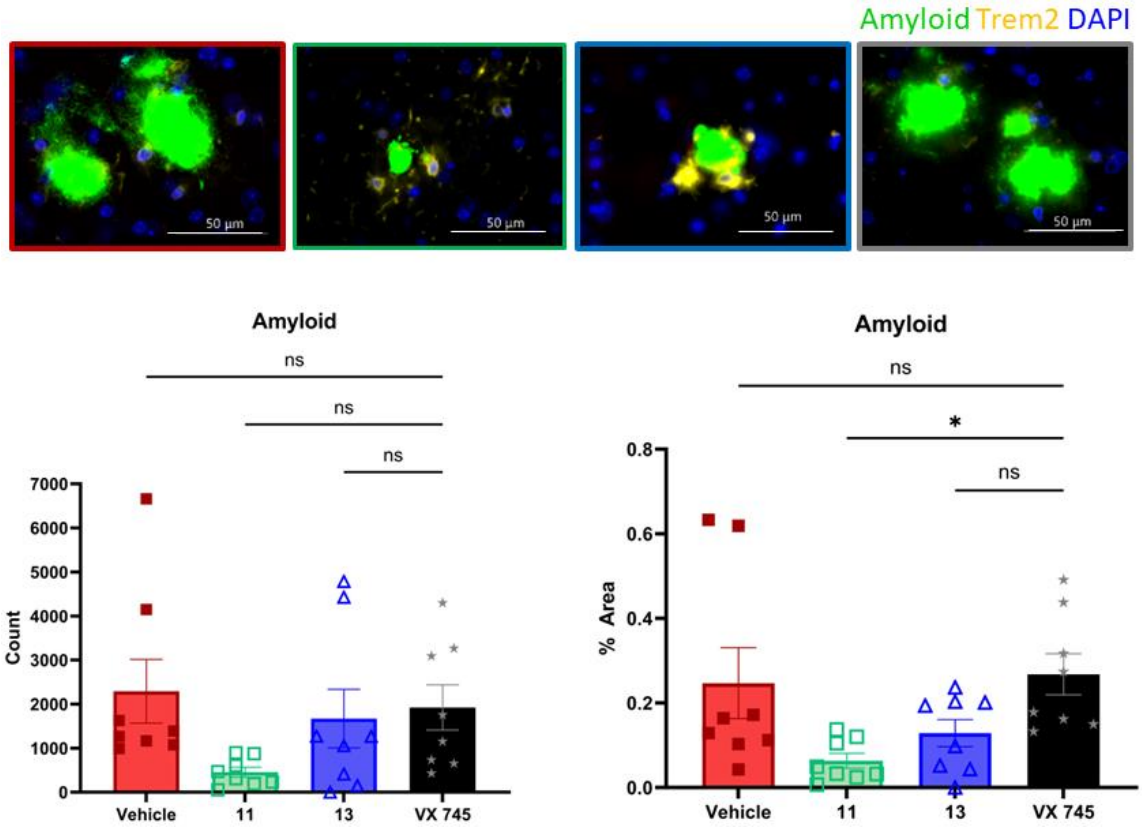

Figure 51. Amyloid-β plaque reduction quantification in 12-month-old APP/PS1 p38α MAP Kinase inhibitor-treated mice. On the top, representative IF microscope images of 100X magnification cortex amyloid plaques stained with Amyloid-β antibody (green channel) and TREM2 (yellow channel) (**Figure 50**). Scale bar 50 µm. **b**) Aβ-positive areas were quantified by ImageJ software. In comparison: APP/PS1 vehicle group (n=8, dark red, full square shape), APP/PS1 compound **11** treated mice (n=8, green, empty square shape), APP/PS1 compound **13** treated mice (n=8, blue, empty triangle shape) and **VX 745** compound treated mice (n=8, black, star full shape). Values are displayed as mean ± SD. * $p < 0.05$; ** $p \leq 0.01$; *** $p \leq 0.001$; **** $p \leq 0.0001$.

4.4 Discussion

The p38α MAP Kinase is expressed in neurons and its expression is considered to be a critical contributor in the toxic effects mediated by amyloid-beta, inflammation and tau.[1,4,6] Given this rationale, I tested two p38α MAP Kinase inhibitors, previously selected in **Chapter 1** of this thesis, in a long-term and short-term study using APP/PS1 as an AD murine model. The decision to study compounds 11 and 13 in the APPPS1 model of amyloidosis was based on a range of earlier studies and observations. Amongst published reports, both VX745 and SB203580 had caused effects on various parameters in mouse AD models.[28,153] Previous studies indicated that Synovo's newer generation of skepinones are highly active in the inflammatory models that was reported in **Chapters 1** and **3** but were not yet tested in amyloidosis models. These results provided the opportunity to investigate the mode of action (MoA) of this class in amyloidosis (AD models) and ask the following questions:

- Is partition to the CNS essential for this MoA?
- What processes are influenced by p38α MAP Kinase inhibitors in brains containing amyloid plaques?
- What is the nature of the anti-inflammatory effect in the context of amyloid?
- Is the effect a rapid or long-term one?

The data generated here answer most of these questions.

In the long-term study, compound **11** (known to not be BBB-penetrant) and compound **13** (BBB-penetrant) were orally administrated by daily food intake for 10.5 months, then behavioral tests and histological evaluation were analyzed in comparison with APP/PS1 and WT vehicle treated animals, matched by age and genetic background. Firstly, I investigated the effect of both compounds on memory impairment-like features occurring in this murine model. The OF results of 12-month-old animals displayed that both compounds showed anxiolytic and anti-depressive effects if compared to APP/PS1 vehicle treated animals (**Figures 41** and **42**). The same animals were tested with the NOR behavioral trial, and while vehicle APP/PS1 12-month-old mice showed memory impairment (time spent with the known object did not differ from the time spent investigating the novel object, ratio Obj1 versus Obj2 is 1:1), both compounds displayed a reversal of the memory impairment to the level of 12-month-old WT animals with the same genetic background (ratio Obj1 versus Obj2 was ~ 1:2) (**Figure 44**). These results are comparable to those reported by Guo *et. al*. where SB203580, a first generation p38 MAP Kinase inhibitor, reversed memory deficits and depression-like behavior in mice microinjected with Aβ1–42 into the hippocampus.[153]

Several studies showed that both depression and cognitive decline in mice are associated with increased amyloid plaques.[154,155,156,157] [157] For this reason, the brains from the 12-months-old mice were subject to histological analysis which showed that compounds **11**

and **13** reduced the amyloid plaque deposition in the total brain by ~ 75 % and 68 %, respectively, if compared to the vehicle treated animals (**Figure 45**). Based on this evidence, on the matter of the importance of partition to the CNS, it appears that this is not essential in this mouse model. Both compounds had similar affinity to the target disease but larger differences in brain exposure in either healthy or APP/PS1 mice. However, the more peripherally active analog, **11**, was the more active in reducing Amyloid or improving memory. These data suggest that peripheral effects can slightly impact the brain response in this model. Thus, one potential aspect of this effect that merits investigation is whether cells that encounter the inhibitor in the periphery undergo a semi-permanent phenotypic shift that dictates their phenotype once in the brain. Alternatively, the explanation may be found in aspects of dose response where the degree of effect could be shifted if the brain experiences over dose that may reverse some beneficial effects obtained at lower doses. These settings will be investigated in future dose response follow up studies.

These results pose questions about possible MoA of the substances. One of my hypotheses involved primarily the microglia subpopulation. While M1 microglia induce inflammation resulting in a diminished ability to phagocytose amyloid leading to neurotoxicity, M2 microglia are considered anti-inflammatory and neuroprotective due to their anti-inflammatory activity and efficacy in phagocytosing amyloid, resulting in good clearance (**Figures 34a** and **b**).[109] The Iba1 marker was then used to investigate microglial activity in the brain of the APP/PS1 mice. Although this general marker does not distinguish between the M1 and M2 subpopulations, the results showed that both compounds promote up-regulation of microglia activated cells (Iba1 positive) by ~ 50 % compared to the vehicle APP/PS1 mice. In order to distinguish between the M1 and M2 phenotypes, immunofluorescent analysis with the marker TREM2 were performed. These data showed that p38α MAP Kinase inhibitor compound **11** promotes the switch from M1 to M2 phenotype: all Iba1 positive cells in treated brains were also TREM2 positive. In contrast, vehicle treated animals showed Iba1 positive cells but only few TREM2 positive cells (**Figure 46**).

Furthermore, due to the latest findings in the dysregulation of endocytic pathways in AD and its link to p38 pathway, abnormalities in the endosomal pathway by Rab5 immunofluorescent analysis were also investigate.[131] These findings showed that while APP/PS1 vehicle mice contained more numerous and atypically large Rab5-positive structures colocalized with Aβ positive staining, compound **11** and **13** treated mice showed smaller Rab5 vesiculas and small Aβ colocalization (**Figure 47**). These results together indicate that p38α MAP Kinase inhibitor treatment promotes clearing of amyloid plaques by up-regulating TREM2 microglia positive cells for phagocytosis and amyloid degradation in late endosomal structures.

With the aim to investigate the short-term beneficial effect of p38α MAP Kinase inhibitor treatment, it was conducted a study over 2 weeks and included **VX 745**, a p38α MAP Kinase inhibitor competitor compound, that in a pilot study in 26-month-old Tg2576 mice showed amyloid reduction and cognitive-impairment improvement.[158] 12-month-old APP/PS1 mice were pre-fed for 4 weeks with HFD, simulating diabetic patient conditions with the aim to exacerbate AD-like symptoms in mice. After two weeks p.o. daily treatment, amyloid beta plaque deposition in the brain was investigated by immunofluorescent analysis. The results showed that compound **11** decreased Aβ size and deposition by 55 % versus vehicle treated mice, while the **VX 745** competitor compound had no effect on amyloid size and clearance (**Figures 50** and **51**). These data indicate that the beneficial effect of compound **11** can also be achieved in short-term treatment.

Clinical trials with certain p38α MAP Kinase inhibitors were discontinued because of liver toxicity.[86] In both of the studies (long and short-term), liver histopathological analysis showed no compound treatment was associated with liver toxicity (**Figures 48** and **49**). These data suggest that both compounds in the dose range of 10 or 5 mg/kg p.o. in long or short-term studies respectively are not associated with obvious effects in liver histopathology. In contrast, even under liver stress conditions (HFD), the compounds are not detrimental and may even be beneficial to liver function and health. HFD would typically magnify any toxic effects of a substance due the oxidative and metabolic stress associated with steatosis. The HFD/steatotic setting may be more relevant to parts of the human population and target patient populations. Thus, these data from a stressed liver setting may be an indication of increased safety in this generation of p38 inhibitors.

4.5 Conclusion

Here, two p38α MAP Kinase inhibitors with different organ affinity profiles (compound **11** is not BBB-penetrant while compound **13** is) were tested in a long-term and in a short-term study (10.5 months versus 2 weeks p.o. daily treatment) on 12-months-old APP/PS1 mice. The selected candidates improved cognitive parameters in the long-term study: memory, activity and anxiety were all reversed to WT levels in age-matched mice with the same genetic background. Further histological analysis in the brain showed that both compounds can cause the removal of amyloid aggregates – within 10.5 months treatment (long-term study, 10 mg/kg/d) and two weeks (short term study, 6 mg/kg/d), while the **VX 745** competitor compound did not. It was also demonstrated that both candidates promote M2/TREM2 activity and maturation in the brain, indicating that p38 inhibitory activity plays a key role in the pathogenesis and progression of the disease. Further investigation on the possible MoA showed that the candidates are promoting amyloid degradation by the early/swelling endosomal intracellular inhibition pathway (minimal

Rab5/Amyloid colocalization), while the vehicle treated animals did not display this (Rab5 and amyloid were colocalized).

5 Thesis summary

In the first chapter of this thesis, 13 novel Skepinone-based p38α MAP Kinase inhibitors with IC_{50} values in the nanomolar range (1 - 5.5 nM range) were characterized *in vitro* and *in vivo*. Due to their *in vitro* potency and their different organ affinity profiles, compound **11** (not BBB-penetrant) and **13** (BBB-penetrant) were further investigated in order to explore the role of p38α MAP Kinase inhibitors in treatment of CNS pathology in murine models of CNS degeneration, here MS and AD.

In the second chapter of this thesis, it was optimized the well-known EAE murine model for MS. The results of this project could show that diet has a major impact on disease severity, incidence and on the gene expression pattern in EAE studies, while the MOG_{35-55}-CFA-emulsion preparation method has implications for the robustness and variability of the model. My investigations led to a more stable and reproducible EAE model that was afterwards used in the following chapter of this thesis.

In the third chapter of this thesis, I investigated the role of p38α MAP Kinase inhibitor compounds on the refined EAE murine model for MS established in **Chapter 2**. The results of this study showed that compound **11**, the peripherally active p38α MAP Kinase inhibitor, increased *in vivo* survival by over 50 % in the EAE CFA/MOG induced optimized mouse model versus vehicle treated animals, resulting also in decrease of the severity of recorded symptoms. Histopathological and gene expression evaluation displayed that the spinal cord and brain benefited from the anti-inflammatory effect of the drugs, showing neuroprotection by myelin fiber preservation and a decrease of the apoptotic factors. Also, in contrast with the failure of other p38 MAP Kinase inhibitors in clinical trials for MS patients attributed to side effects in the liver, both compounds **11** and **13** showed liver toxicity protection by histopathological and qPCR analysis indicating great potential beneficial therapeutic effects as drug against MS.

In the fourth chapter of the thesis, p38α MAP Kinase inhibitors **11** and **13** were tested in a long-term and in a short-term study (10.5 months versus 2 weeks p.o. daily treatment) in APP/PS1 mice. In the long-term study, the selected candidates improved cognitive and affective parameters. In terms of memory, activity and anxiety, the compounds showed recovery of these parameters if compared with WT detected levels of age-matched mice with the same genetic background. Additionally, both compounds caused the removal of amyloid aggregates – within 10.5 months treatment and 2 weeks – while the competitor compound (**VX 745**) did not. It was also demonstrated that p38 inhibitory activity plays a key role in the pathogenesis and progression of the disease: both candidates enhanced M2/TREM2 activity and maturation in brain. Further investigation on the possible MoA showed that the candidates are promoting amyloid degradation by late endosome intra-cellular pathway activation.

6 References

1. Munoz, L. & Ammit, A. J. Targeting p38 MAPK pathway for the treatment of Alzheimer's disease. *Neuropharmacology* **58**, 561–568 (2010).

2. Munoz, L. *et al.* A novel p38α MAPK inhibitor suppresses brain proinflammatory cytokine up-regulation and attenuates synaptic dysfunction and behavioral deficits in an Alzheimer's disease mouse model. *J. Neuroinflammation* **4**, 21 (2007).

3. Yasuda, S., Sugiura, H., Tanaka, H., Takigami, S. & Yamagata, K. p38 MAP Kinase inhibitors as potential therapeutic drugs for neural diseases. *Cent. Nerv. Syst. Agents Med. Chem.* **11**, 45–59 (2011).

4. Lee, J. K. & Kim, N. J. Recent Advances in the Inhibition of p38 MAPK as a Potential Strategy for the Treatment of Alzheimer's Disease. *Molecules* **22**, (2017).

5. Bohush, A., Niewiadomska, G. & Filipek, A. Role of Mitogen Activated Protein Kinase Signaling in Parkinson's Disease. *Int. J. Mol. Sci.* **19**, (2018).

6. Asih, P. R. *et al.* Functions of p38 MAP Kinases in the Central Nervous System. *Front. Mol. Neurosci.* **13**, (2020).

7. Germann, U. A. & Alam, J. J. P38α MAPK Signaling-A Robust Therapeutic Target for Rab5-Mediated Neurodegenerative Disease. *Int. J. Mol. Sci.* **21**, 1–19 (2020).

8. Lee, J. C. *et al.* A protein kinase involved in the regulation of inflammatory cytokine biosynthesis. *Nature* **372**, 739–746 (1994).

9. Hensley, K. *et al.* p38 kinase is activated in the Alzheimer's disease brain. *J. Neurochem.* **72**, 2053–2058 (1999).

10. Sun, A., Liu, M., Nguyen, X. V. & Bing, G. p38 MAP Kinase is activated at early stages in Alzheimer's disease brain. *Exp. Neurol.* **183**, 394–405 (2003).

11. Rutigliano, G., Stazi, M., Arancio, O., Watterson, D. M. & Origlia, N. An isoform-selective p38α mitogen-activated protein kinase inhibitor rescues early entorhinal cortex dysfunctions in a mouse model of Alzheimer's disease. *Neurobiol. Aging* **70**, 86–91 (2018).

12. Bachstetter, A. D. *et al.* Microglial p38α MAPK is a key regulator of proinflammatory cytokine up-regulation induced by toll-like receptor (TLR) ligands or beta-amyloid (Aβ). *J. Neuroinflammation* **8**, 1–12 (2011).

13. Krementsov, D. N., Thornton, T. M., Teuscher, C. & Rincon, M. The Emerging Role of p38 Mitogen-Activated Protein Kinase in Multiple Sclerosis and Its Models. *Mol. Cell. Biol.* **33**, 3728 (2013).

14. Martino, G. *et al.* Cytokines and immunity in multiple sclerosis: the dual signal hypothesis. *J. Neuroimmunol.* **109**, 3–9 (2000).

15. Uccelli, A., Pedemonte, E., Narciso, E. & Mancardi, G. Biological markers of the inflammatory phase of multiple sclerosis. *Neurol. Sci.* **24 Suppl 5**, (2003).

16. Lock, C. *et al.* Gene-microarray analysis of multiple sclerosis lesions yields new targets validated in autoimmune encephalomyelitis. *Nat. Med.* **8**, 500–508 (2002).

17. Duffy, J. P. *et al.* The Discovery of VX-745: A Novel and Selective p38α Kinase Inhibitor. *ACS Med. Chem. Lett.* **2**, 758 (2011).

18. Haddad, J. J. VX-745. Vertex Pharmaceuticals. *Curr. Opin. Investig. drugs* (2001).

19. Roy, S. M. *et al.* Targeting human central nervous system protein kinases: An isoform selective p38αMAPK inhibitor that attenuates disease progression in Alzheimer's disease mouse models. *ACS Chem. Neurosci.* **6**, 666–680 (2015).

20. Robson, M. J. *et al.* p38α MAPK signaling drives pharmacologically reversible brain and gastrointestinal phenotypes in the SERT Ala56 mouse. *Proc. Natl. Acad. Sci. U. S. A.* **115**, E10245–E10254 (2018).

21. Zhou, Z. *et al.* Retention of normal glia function by an isoform-selective protein kinase inhibitor drug candidate that modulates cytokine production and cognitive outcomes. *J. Neuroinflammation* **14**, 1–12 (2017).

22. Roy, S. M. *et al.* A Selective and Brain Penetrant p38αMAPK Inhibitor Candidate for Neurologic and Neuropsychiatric Disorders That Attenuates Neuroinflammation and Cognitive Dysfunction. *J. Med. Chem.* **62**, 5298–5311 (2019).

23. Koeberle, S. C. *et al.* Skepinone-L is a selective p38 mitogen-activated protein kinase inhibitor. *Nat. Chem. Biol.* **8**, 141–143 (2011).

24. Koeberle, S. C. *et al.* Design, synthesis, and biological evaluation of novel disubstituted dibenzosuberones as highly potent and selective inhibitors of p38 mitogen activated protein kinase. *J. Med. Chem.* **55**, 5868–5877 (2012).

25. Walter, N. M. *et al.* Design, Synthesis, and Biological Evaluation of Novel Type I1/2 p38α MAP Kinase Inhibitors with Excellent Selectivity, High Potency, and Prolonged Target Residence Time by Interfering with the R-Spine. *J. Med. Chem.* **60**, 8027–8054 (2017).

26. Wentsch, H. K. *et al.* Optimized Target Residence Time: Type I1/2 Inhibitors for p38α MAP Kinase with Improved Binding Kinetics through Direct Interaction with the R-Spine. *Angew. Chemie - Int. Ed.* **56**, 5363–5367 (2017).

27. Tormählen, N. M. *et al.* Design and Synthesis of Highly Selective Brain Penetrant p38α Mitogen-Activated Protein Kinase Inhibitors. *J. Med. Chem.* **65**, 1225–1242 (2022).

28. Alam, J., Blackburn, K. & Patrick, D. Neflamapimod: Clinical Phase 2b-Ready Oral Small Molecule Inhibitor of p38α to Reverse Synaptic Dysfunction in Early Alzheimer's Disease. *J. Prev. Alzheimer's Dis.* **4**, 273–278 (2017).

29. Compston, A. & Coles, A. Multiple sclerosis. *Lancet* **372**, 1502–1517 (2008).

30. Goldenberg, M. M. Multiple sclerosis review. *P T* **37**, 175–184 (2012).

31. Thompson, A. J., Baranzini, S. E., Geurts, J., Hemmer, B. & Ciccarelli, O. Multiple sclerosis. *Lancet (London, England)* **391**, 1622–1636 (2018).

32. Lublin, F. D. & Reingold, S. C. Defining the clinical course of multiple sclerosis. *Neurology* **46**, 907 LP-911 (1996).

33. Oh, J. & Bar-Or, A. Emerging therapies to target CNS pathophysiology in multiple sclerosis. *Nat. Rev. Neurol. 2022 188* **18**, 466–475 (2022).

34. Constantinescu, C. S. & Gran, B. Autoimmune associations in multiple sclerosis. *Nat. Rev. Neurol.* **6**, 591–592 (2010).

35. Miller, S. D., Karpus, W. J. & Davidson, T. S. Experimental Autoimmune Encephalomyelitis in the Mouse. *Curr. Protoc. Immunol.* **88**, 15.1.1-15.1.20 (2010).

36. Chen, X. *et al.* The Molecular Mechanisms of Ferroptosis and Its Role in Blood-Brain Barrier Dysfunction. *Front. Cell. Neurosci.* **16**, 231 (2022).

37. Beard, J. L. Iron biology in immune function, muscle metabolism and neuronal functioning. *J. Nutr.* **131**, (2001).

38. Stankiewicz, J. M., Neema, M. & Ceccarelli, A. Iron and multiple sclerosis. *Neurobiol. Aging* **35**, S51–S58 (2014).

39. Zielińska, M. & Michońska, I. Macronutrients, vitamins and minerals in the diet of multiple sclerosis patients. *Adv. Psychiatry Neurol. Psychiatr. i Neurol.* **31**, 128–137 (2022).

40. Choi, Y. *et al.* Vitamin E (α-tocopherol) consumption influences gut microbiota composition. *Int. J. Food Sci. Nutr.* **71**, 221–225 (2020).

41. Gilgun-Sherki, Y., Melamed, E. & Offen, D. The role of oxidative stress in the pathogenesis of multiple sclerosis: the need for effective antioxidant therapy. *J. Neurol.* **251**, 261–268 (2004).

42. Stanhope, K. L. & Havel, P. J. Fructose consumption: recent results and their potential implications. *Ann. N. Y. Acad. Sci.* **1190**, 15–24 (2010).

43. Singh, R. K. *et al.* Influence of diet on the gut microbiome and implications for human health. *J. Transl. Med. 2017 151* **15**, 1–17 (2017).

44. Gold, R., Linington, C. & Lassmann, H. Understanding pathogenesis and therapy of multiple sclerosis via animal models: 70 years of merits and culprits in experimental autoimmune encephalomyelitis research. *Brain* **129**, 1953–1971 (2006).

45. Hasselmann, J. P. C., Karim, H., Khalaj, A. J., Ghosh, S. & Tiwari-Woodruff, S. K. Consistent induction of chronic experimental autoimmune encephalomyelitis in C57BL/6 mice for the longitudinal study of pathology and repair. *J. Neurosci. Methods* **284**, 71–84 (2017).

46. Wendeln, A. C. *et al.* Innate immune memory in the brain shapes neurological disease hallmarks. *Nature* **556**, 332–338 (2018).

47. Livak, K. J. & Schmittgen, T. D. Analysis of relative gene expression data using real-time quantitative PCR and the 2(-Delta Delta C(T)) Method. *Methods* **25**, 402–408 (2001).

48. Katz Sand, I. The Role of Diet in Multiple Sclerosis: Mechanistic Connections and Current Evidence. *Curr. Nutr. Rep.* **7**, 150–160 (2018).

49. Guerrero Aznar, M. D. *et al.* Efficacy of diet on fatigue, quality of life and disability status in multiple sclerosis patients: rapid review and meta-analysis of randomized controlled trials. *BMC Neurol.* **22**, 1–16 (2022).

50. Botella Romero, F., Alfaro Martínez, J. J., Luna López, V., Galicia Martín, I. & Grupo de Trabajo sobre Calcio y Vitamina D en Nutrición Enteral. [Enteral nutrition in neurological patients: is there enough vitamin D content in commonly used formulas?]. *Nutr. Hosp.* **27**, 341–8 (2012).

51. Brahmachari, S., Fung, Y. K. & Pahan, K. Induction of glial fibrillary acidic protein expression in astrocytes by nitric oxide. *J. Neurosci.* **26**, 4930–4939 (2006).

52. Wolf, Y. *et al.* Microglial MHC class II is dispensable for experimental autoimmune encephalomyelitis and cuprizone-induced demyelination. *Eur. J. Immunol.* **48**, 1308–1318 (2018).

53. Hamilton, A. M. *et al.* Central nervous system targeted autoimmunity causes regional atrophy: a 9.4T MRI study of the EAE mouse model of Multiple Sclerosis. *Sci. Rep.* **9**, 1–13 (2019).

54. Dias, A. T. *et al.* Different MOG(35-55) concentrations induce distinguishable inflammation through early regulatory response by IL-10 and TGF-β in mice CNS despite unchanged clinical course. *Cell. Immunol.* **293**, 87–94 (2015).

55. Huntemann, N. *et al.* An optimized and validated protocol for inducing chronic experimental autoimmune encephalomyelitis in C57BL/6J mice. *J. Neurosci. Methods* **367**, (2022).

56. Berer, K. *et al.* Dietary non-fermentable fiber prevents autoimmune neurological disease by changing gut metabolic and immune status. *Sci. Rep.* **8**, 10431 (2018).

57. Wendeln, A. C. *et al.* Innate immune memory in the brain shapes neurological disease hallmarks. *Nature* **556**, 332–338 (2018).

58. Fitzgerald, K. C. *et al.* Diet quality is associated with disability and symptom severity in multiple sclerosis. *Neurology* **90**, E1–E11 (2018).

59. Makki, K., Deehan, E. C., Walter, J. & Bäckhed, F. The Impact of Dietary Fiber on Gut Microbiota in Host Health and Disease. *Cell Host Microbe* **23**, 705–715 (2018).

60. Ward, R. J., Zucca, F. A., Duyn, J. H., Crichton, R. R. & Zecca, L. The role of iron in brain

ageing and neurodegenerative disorders. *Lancet. Neurol.* **13**, 1045 (2014).

61. Cheli, V. T., Correale, J., Paez, P. M. & Pasquini, J. M. Iron Metabolism in Oligodendrocytes and Astrocytes, Implications for Myelination and Remyelination. *ASN Neuro* **12**, (2020).

62. Kirby, T. O. & Ochoa-Repáraz, J. The Gut Microbiome in Multiple Sclerosis: A Potential Therapeutic Avenue. *Med. Sci. (Basel, Switzerland)* **6**, 69 (2018).

63. Mills, E., Dong, X. P., Wang, F. & Xu, H. Mechanisms of brain iron transport: insight into neurodegeneration and CNS disorders. *Future Med. Chem.* **2**, 51–64 (2010).

64. Rand, D. *et al.* Endothelial Iron Homeostasis Regulates Blood-Brain Barrier Integrity via the HIF2α-Ve-Cadherin Pathway. *Pharmaceutics* **13**, 1–24 (2021).

65. Fauci, A. S. *Harrison's principles of internal medicine*. (McGraw-Hill Education, 2015).

66. Caetano, A. *et al.* The antioxidant response of the liver of male Swiss mice raised on a AIN 93 or commercial diet. *BMC Physiol.* **13**, 3 (2013).

67. Wang, D. *et al.* Resveratrol defends blood-brain barrier integrity in experimental autoimmune encephalomyelitis mice. *J. Neurophysiol.* **116**, 2173–2179 (2016).

68. Stavroulakis, T. & McDermott, C. J. Enteral feeding in neurological disorders. *Pract. Neurol.* **16**, 352–361 (2016).

69. Burgos, R. *et al.* ESPEN guideline clinical nutrition in neurology. *Clin. Nutr.* **37**, 354–396 (2018).

70. Ma, Q. *et al.* Impact of microbiota on central nervous system and neurological diseases: the gut-brain axis. *J. Neuroinflammation* **16**, 1–14 (2019).

71. Goldenberg, M. M. Multiple Sclerosis Review. *Pharm. Ther.* **37**, 175 (2012).

72. Carli, M. De, D'elios, M. M., Zancuoghi, G., Romagnani, S. & Prete, G. Del. Review human th1 and th2 cells: Functional properties, regulation of development and role in autoimmunity. *Autoimmunity* **18**, 301–308 (1994).

73. Soldan, S. S. & Lieberman, P. M. Epstein–Barr virus and multiple sclerosis. *Nat. Rev. Microbiol. 2022 211* **21**, 51–64 (2022).

74. Liu, R. *et al.* Autoreactive lymphocytes in multiple sclerosis: Pathogenesis and treatment target. *Front. Immunol.* **13**, 996469 (2022).

75. Ghasemi, N., Razavi, S. & Nikzad, E. Multiple Sclerosis: Pathogenesis, Symptoms, Diagnoses andCell-Based Therapy. *Cell J.* **19**, 1 (2017).

76. Roy, S. M. *et al.* A Selective and Brain Penetrant p38αMAPK Inhibitor Candidate for Neurologic and Neuropsychiatric Disorders That Attenuates Neuroinflammation and Cognitive Dysfunction. *J. Med. Chem.* **62**, 5298–5311 (2019).

77. Lee, J. K. & Kim, N. J. Recent Advances in the Inhibition of p38 MAPK as a Potential Strategy for the Treatment of Alzheimer's Disease. *Mol. A J. Synth. Chem. Nat. Prod. Chem.* **22**, (2017).

78. Yang, A. T. *et al.* TGF- β 1 induces the dual regulation of hepatic progenitor cells with both anti- and proliver fibrosis. *Stem Cells Int.* **2016**, (2016).

79. Xu, F., Liu, C., Zhou, D. & Zhang, L. TGF-β/SMAD Pathway and Its Regulation in Hepatic Fibrosis. *J. Histochem. Cytochem.* **64**, 157 (2016).

80. Nga, H. T. *et al.* Interleukin-10 Attenuates Liver Fibrosis Exacerbated by Thermoneutrality. *Front. Med.* **8**, 672658 (2021).

81. Basaranoglu, M., Basaranoglu, G. & Bugianesi, E. Carbohydrate intake and nonalcoholic fatty liver disease: fructose as a weapon of mass destruction. *Hepatobiliary Surg. Nutr.* **4**, 10916–10116 (2015).

82. Singh, A., Upadhayay, S. & Mehan, S. Inhibition of c-JNK/p38MAPK signaling pathway by Apigenin prevents neurobehavioral and neurochemical defects in ethidium bromide-induced experimental model of multiple sclerosis in rats: Evidence from CSF, blood plasma and brain samples. *Phytomedicine Plus* **1**, 100139 (2021).

83. Singh, A., Upadhayay, S. & Mehan, S. Understanding Abnormal c-JNK/p38MAPK Signaling Overactivation Involved in the Progression of Multiple Sclerosis: Possible Therapeutic Targets and Impact on Neurodegenerative Diseases. *Neurotox. Res.* **39**, 1630–1650 (2021).

84. Noubade, R. *et al.* Activation of p38 MAPK in CD4 T cells controls IL-17 production and autoimmune encephalomyelitis. *Blood* **118**, 3290–3300 (2011).

85. Xing, B., Bachstetter, A. D. & Van Eldik, L. J. Inhibition of neuronal p38α, but not p38β MAPK, provides neuroprotection against three different neurotoxic insults. *J. Mol. Neurosci.* **55**, 509–518 (2015).

86. Dambach, D. Potential adverse effects associated with inhibition of p38alpha/beta MAP Kinases. *Curr. Top. Med. Chem.* **5**, 929–939 (2005).

87. d'Errico, P. & Meyer-Luehmann, M. Mechanisms of Pathogenic Tau and Aβ Protein Spreading in Alzheimer's Disease. *Front. Aging Neurosci.* **12**, 581817 (2020).

88. Crosson, F. J., Covinsky, K. & Redberg, R. F. Medicare and the Shocking US Food and Drug Administration Approval of Aducanumab: Crisis or Opportunity? *JAMA Intern. Med.* **181**, 1278–1280 (2021).

89. De La Torre, J. C. & Gonzalez-Lima, F. The FDA Approves Aducanumab for Alzheimer's Disease, Raising Important Scientific Questions1. *J. Alzheimers. Dis.* **82**, 881–882 (2021).

90. Holmes, C. *et al.* Systemic inflammation and disease progression in Alzheimer disease. *Neurology* **73**, 768–774 (2009).

91. Zhao, M. *et al.* The induction of the TNFalpha death domain signaling pathway in Alzheimer's disease brain. *Neurochem. Res.* **28**, 307–318 (2003).

92. Kim, J. W. *et al.* Longitudinal Associations Between Serum Cytokine Levels and Dementia. *Front. psychiatry* **9**, (2018).

93. Louveau, A. *et al.* CNS lymphatic drainage and neuroinflammation are regulated by meningeal lymphatic vasculature. *Nat. Neurosci. 2018 2110* **21**, 1380–1391 (2018).

94. Da Mesquita, S. *et al.* Functional aspects of meningeal lymphatics in ageing and Alzheimer's disease. *Nature* **560**, 185–191 (2018).

95. Jorfi, M., Maaser-Hecker, A. & Tanzi, R. E. The neuroimmune axis of Alzheimer's disease. *Genome Med. 2023 151* **15**, 1–25 (2023).

96. Stanciu, G. D. *et al.* Link between Diabetes and Alzheimer's Disease Due to the Shared Amyloid Aggregation and Deposition Involving Both Neurodegenerative Changes and Neurovascular Damages. *J. Clin. Med.* **9**, 1–25 (2020).

97. Jash, K. *et al.* Cognitive dysfunction: A growing link between diabetes and Alzheimer's disease. *Drug Dev. Res.* **81**, 144–164 (2020).

98. Sun, Y. *et al.* Metabolism: A Novel Shared Link between Diabetes Mellitus and Alzheimer's Disease. *J. Diabetes Res.* **2020**, (2020).

99. de la Monte, S. M. Insulin Resistance and Neurodegeneration: Progress Towards the Development of New Therapeutics for Alzheimer's Disease. *Drugs 2016 771* **77**, 47–65 (2016).

100. Devi, L., Alldred, M. J., Ginsberg, S. D. & Ohno, M. Mechanisms Underlying Insulin Deficiency-Induced Acceleration of β-Amyloidosis in a Mouse Model of Alzheimer's Disease. *PLoS One* **7**, e32792 (2012).

101. Natunen, T. *et al.* Diabetic phenotype in mouse and humans reduces the number of microglia around β-amyloid plaques. *Mol. Neurodegener. 2020 151* **15**, 1–30 (2020).

102. Walker, K. A., Ficek, B. N. & Westbrook, R. Understanding the Role of Systemic Inflammation in Alzheimer's Disease. *ACS Chem. Neurosci.* **10**, 3340–3342 (2019).

103. Bachstetter, A. D. & Van Eldik, L. J. The p38 MAP Kinase Family as Regulators of Proinflammatory Cytokine Production in Degenerative Diseases of the CNS. *Aging Dis.* **1**, 199 (2010).

104. Jiang, Y. *et al.* Characterization of the structure and function of a new mitogen-activated protein kinase (p38beta). *J. Biol. Chem.* **271**, 17920–17926 (1996).

105. Ono, K. & Han, J. The p38 signal transduction pathway: activation and function. *Cell. Signal.* **12**, 1–13 (2000).

106. van den Blink, B. *et al.* p38 mitogen-activated protein kinase inhibition increases cytokine release by macrophages in vitro and during infection in vivo. *J. Immunol.* **166**, 582–587

(2001).

107. Hong, S. *et al.* Complement and microglia mediate early synapse loss in Alzheimer mouse models. *Science* **352**, 712–716 (2016).

108. Guo, S., Wang, H. & Yin, Y. Microglia Polarization From M1 to M2 in Neurodegenerative Diseases. *Front. Aging Neurosci.* **14**, (2022).

109. Miao, J. *et al.* Microglia in Alzheimer's disease: pathogenesis, mechanisms, and therapeutic potentials. *Front. Aging Neurosci.* **15**, 1201982 (2023).

110. Sarlus, H. & Heneka, M. T. Microglia in Alzheimer's disease. *J. Clin. Invest.* **127**, 3240–3249 (2017).

111. Gao, C., Jiang, J., Tan, Y. & Chen, S. Microglia in neurodegenerative diseases: mechanism and potential therapeutic targets. *Signal Transduct. Target. Ther. 2023 81* **8**, 1–37 (2023).

112. Wendimu, M. Y. & Hooks, S. B. Microglia Phenotypes in Aging and Neurodegenerative Diseases. *Cells* **11**, (2022).

113. Deczkowska, A. *et al.* Disease-Associated Microglia: A Universal Immune Sensor of Neurodegeneration. *Cell* **173**, 1073–1081 (2018).

114. Keren-Shaul, H. *et al.* A Unique Microglia Type Associated with Restricting Development of Alzheimer's Disease. *Cell* **169**, 1276–1290.e17 (2017).

115. Guerreiro, R. *et al.* TREM2 variants in Alzheimer's disease. *N. Engl. J. Med.* **368**, 117–127 (2013).

116. Jonsson, T. *et al.* Variant of TREM2 associated with the risk of Alzheimer's disease. *N. Engl. J. Med.* **368**, 107–116 (2013).

117. Lee, C. Y. D. *et al.* Elevated TREM2 Gene Dosage Reprograms Microglia Responsivity and Ameliorates Pathological Phenotypes in Alzheimer's Disease Models. *Neuron* **97**, 1032–1048.e5 (2018).

118. Schlepckow, K. *et al.* Enhancing protective microglial activities with a dual function TREM2 antibody to the stalk region. *EMBO Mol. Med.* **12**, (2020).

119. Ellwanger, D. C. *et al.* Prior activation state shapes the microglia response to antihuman TREM2 in a mouse model of Alzheimer's disease. *Proc. Natl. Acad. Sci. U. S. A.* **118**, (2021).

120. Henjum, K. *et al.* Cerebrospinal fluid soluble TREM2 in aging and Alzheimer's disease. *Alzheimers. Res. Ther.* **8**, (2016).

121. Heslegrave, A. *et al.* Increased cerebrospinal fluid soluble TREM2 concentration in Alzheimer's disease. *Mol. Neurodegener.* **11**, (2016).

122. Suárez-Calvet, M. *et al.* Early increase of CSF sTREM2 in Alzheimer's disease is associated with tau related-neurodegeneration but not with amyloid-β pathology. *Mol.*

Neurodegener. **14**, (2019).

123. Ewers, M. *et al.* Increased soluble TREM2 in cerebrospinal fluid is associated with reduced cognitive and clinical decline in Alzheimer's disease. *Sci. Transl. Med.* **11**, (2019).

124. Pascoal, T. A. *et al.* Microglial activation and tau propagate jointly across Braak stages. *Nat. Med.* **27**, 1592–1599 (2021).

125. Brown, G. C. & St George-Hyslop, P. Does Soluble TREM2 Protect Against Alzheimer's Disease? *Front. Aging Neurosci.* **13**, 834697 (2022).

126. Wu, L. *et al.* Toll-Like Receptor 4: A Promising Therapeutic Target for Alzheimer's Disease. *Mediators Inflamm.* **2022**, (2022).

127. Zhou, J. *et al.* Imbalance of Microglial TLR4/TREM2 in LPS-Treated APP/PS1 Transgenic Mice: A Potential Link Between Alzheimer's Disease and Systemic Inflammation. *Neurochem. Res.* **44**, 1138–1151 (2019).

128. Ruganzu, J. B. *et al.* Downregulation of TREM2 expression exacerbates neuroinflammatory responses through TLR4-mediated MAPK signaling pathway in a transgenic mouse model of Alzheimer's disease. *Mol. Immunol.* **142**, 22–36 (2022).

129. Yang, J. *et al.* TREM2 ectodomain and its soluble form in Alzheimer's disease. *J. Neuroinflammation* **17**, (2020).

130. Hu, Y. *et al.* TREM2, Driving the Microglial Polarization, Has a TLR4 Sensitivity Profile After Subarachnoid Hemorrhage. *Front. Cell Dev. Biol.* **9**, 693342 (2021).

131. Xu, W., Fang, F., Ding, J. & Wu, C. Dysregulation of Rab5-Mediated Endocytic Pathways in Alzheimer's Disease. *Traffic* **19**, 253 (2018).

132. Grbovic, O. M. *et al.* Rab5-stimulated Up-regulation of the Endocytic Pathway Increases Intracellular Î²-Cleaved Amyloid Precursor Protein Carboxyl-terminal Fragment Levels and AÎ² Production*. *J. Biol. Chem.* **278**, 31261–31268 (2003).

133. Jiang, M. & Chen, G. Ca2+ Regulation of Dynamin-Independent Endocytosis in Cortical Astrocytes. *J. Neurosci.* **29**, 8063 (2009).

134. Colacurcio, D. J., Pensalfini, A., Jiang, Y. & Nixon, R. A. Dysfunction of Autophagy and Endosomal-Lysosomal Pathways: Roles in Pathogenesis of Down Syndrome and Alzheimer's Disease. *Free Radic. Biol. Med.* **114**, 40 (2018).

135. Gengler, S., Hamilton, A. & Hölscher, C. Synaptic plasticity in the hippocampus of a APP/PS1 mouse model of Alzheimer's disease is impaired in old but not young mice. *PLoS One* **5**, (2010).

136. Radde, R. *et al.* Abeta42-driven cerebral amyloidosis in transgenic mice reveals early and robust pathology. *EMBO Rep.* **7**, 940–946 (2006).

137. Serneels, L. *et al.* γ-Secretase Heterogeneity in the Aph1 Subunit: Relevance for Alzheimer's Disease. *Science* **324**, 639 (2009).

138. Blanchard, V. *et al.* Time sequence of maturation of dystrophic neurites associated with Aβ deposits in APP/PS1 transgenic mice. *Exp. Neurol.* **184**, 247–263 (2003).

139. Ramos, B. *et al.* Early neuropathology of somatostatin/NPY GABAergic cells in the hippocampus of a PS1 × APP transgenic model of Alzheimer's disease. *Neurobiol. Aging* **27**, 1658–1672 (2006).

140. Caballero, C. *et al.* Inter-individual variability in the expression of the mutated form of hPS1M146L determined the production of Abeta peptides in the PS1xAPP transgenic mice. *J. Neurosci. Res.* **85**, 787–797 (2007).

141. Jimenez, S. *et al.* Inflammatory response in the hippocampus of PS1M146L/APP751SL mouse model of Alzheimer's disease: age-dependent switch in the microglial phenotype from alternative to classic. *J. Neurosci.* **28**, 11650–11661 (2008).

142. Moreno-Gonzalez, I. *et al.* Extracellular amyloid-beta and cytotoxic glial activation induce significant entorhinal neuron loss in young PS1(M146L)/APP(751SL) mice. *J. Alzheimers. Dis.* **18**, 755–776 (2009).

143. Baglietto-Vargas, D. *et al.* Calretinin interneurons are early targets of extracellular amyloid-beta pathology in PS1/AbetaPP Alzheimer mice hippocampus. *J. Alzheimers. Dis.* **21**, 119–132 (2010).

144. Sanchez-Varo, R. *et al.* Abnormal accumulation of autophagic vesicles correlates with axonal and synaptic pathology in young Alzheimer's mice hippocampus. *Acta Neuropathol.* **123**, 53–70 (2012).

145. Trujillo-Estrada, L. *et al.* Early neuronal loss and axonal/presynaptic damage is associated with accelerated amyloid-β accumulation in AβPP/PS1 Alzheimer's disease mice subiculum. *J. Alzheimers. Dis.* **42**, 521–541 (2014).

146. Gomez-Arboledas, A. *et al.* Phagocytic clearance of presynaptic dystrophies by reactive astrocytes in Alzheimer's disease. *Glia* **66**, 637–653 (2018).

147. Webster, S. J., Bachstetter, A. D. & Van Eldik, L. J. Comprehensive behavioral characterization of an APP/PS-1 double knock-in mouse model of Alzheimer's disease. *Alzheimer's Res. Ther.* **5**, 1–15 (2013).

148. Zhang, R. *et al.* Novel object recognition as a facile behavior test for evaluating drug effects in AβPP/PS1 Alzheimer's disease mouse model. *J. Alzheimers. Dis.* **31**, 801–812 (2012).

149. Kelliny, S. *et al.* A New Approach to Model Sporadic Alzheimer's Disease by Intracerebroventricular Streptozotocin Injection in APP/PS1 Mice. *Mol. Neurobiol.* **58**, 3692–3711 (2021).

150. Breitve, M. H. *et al.* A longitudinal study of anxiety and cognitive decline in dementia with Lewy bodies and Alzheimer's disease. *Alzheimers. Res. Ther.* **8**, (2016).

151. Okuzono, Y. *et al.* Reduced TREM2 activation in microglia of patients with Alzheimer's

disease. *FEBS Open Bio* **11**, 3063–3080 (2021).

152. Jang, Y. *et al.* In vitro and in vivo antiviral activity of nylidrin by targeting the hemagglutinin 2-mediated membrane fusion of influenza A virus. *Viruses* **12**, (2020).

153. Guo, J. *et al.* SB203580 reverses memory deficits and depression-like behavior induced by microinjection of Aβ1–42 into hippocampus of mice. *Metab. Brain Dis.* **32**, 57–68 (2017).

154. Chan, C. & Rosenberg, P. B. Depression Synergy With Amyloid and Increased Risk of Cognitive Decline in Preclinical Alzheimer Disease. *JAMA Netw. Open* **2**, e198970–e198970 (2019).

155. Sun, X. *et al.* Amyloid-Associated Depression: A Prodromal Depression of Alzheimer Disease? *Arch. Gen. Psychiatry* **65**, 542 (2008).

156. Espenes, R. *et al.* Amyloid Plaques and Symptoms of Depression Links to Medical Help-Seeking due to Subjective Cognitive Decline. *J. Alzheimers. Dis.* **75**, 879–890 (2020).

157. Romoli, M., Sen, A., Parnetti, L., Calabresi, P. & Costa, C. Amyloid-β: a potential link between epilepsy and cognitive decline. *Nat. Rev. Neurol.* **17**, 469–485 (2021).

158. Alam, J. J. Selective Brain-Targeted Antagonism of p38 MAPKα Reduces Hippocampal IL-1β Levels and Improves Morris Water Maze Performance in Aged Rats. *J. Alzheimer's Dis.* **48**, 219–227 (2015).

7 Figures and Tables Content

8 Acknowledgments

Firstly, I would Like to thank Prof. Laufer and Prof. Koch for their precious guide during my Ph.D. and my scientific career.

Thanks to Dr. Michael Burnet for the great opportunity to pursue my experiments at Synovo GmbH. Thanks for the constant support, the trust and the advice you gave me. I won't forget.

I would like to thank Dr. Florian Maier, my supervisor, my mentor. You push me to my limits and made me love science in a way I couldn't imagine to be possible.

Thanks to Dr. Martin Reisser, Dr. Lara Wohlbold and Dr. Agne Klein, precious colleagues and great scientists without whom this thesis wouldn't be the same.

Thanks to Eleanor, Santiago, Luciano, Katharina, Thilo, Johanna, Tina, Thomas and Christina who helped me not only with my experiments, but they made me laugh when I could not.

I would like to thank my family, my mum Tina, my dad Riziero, my brother Emiliano and my sister Niulka. Thanks for your help and your unconditional love.

Last but not least, I would like to thank Matthias, a colleague, a great researcher and my family. You are the biggest supporter in my scientific life and even more. I want to be yours.

This thesis is dedicated to Lella. I think about you everyday. I miss you and I will always do.